# RAMAN SPECTROSCOPY FOR PLANETARY EXPLORATION AND CHARACTERIZATION OF EXTRATERRESTRIAL MATERIALS

A DISSERTATION SUBMITTED TO THE GRADUATE DIVISION OF THE UNIVERSITY OF HAWAIʻI AT MĀNOA IN PARTIAL FULFILLMENT OF THE REQUIREMENTS FOR THE DEGREE OF

DOCTOR OF PHILOSOPHY

IN

GEOLOGY AND GEOPHYSICS

AUGUST 2016

By:

Tayro E. Acosta-Maeda

Dissertation Committee

Shiv K. Sharma, Chairperson
Patricia Fryer
Edward R. D. Scott
Anupam K. Misra
Stephen M. Masutani

# ACKNOWLEDGEMENTS

I would like to express my deepest gratitude to Professor Shiv Sharma. Not only for helping me grow as a scientist as my advisor, but also for being the very reason I came to the University of Hawai‘i and for allowing me to become part of his Raman spectroscopy laboratory. Without his continued support, this dissertation would not have been possible. I am also very thankful to everyone I had the pleasure to work with at the laboratory. I am especially thankful to Anupam Misra for helping me as a coworker, as a student, as a scientist and as a person. Thanks also to David Bates and Mark Wood for their invaluable help with software and data processing, to Frederick Matsunaga for helping with technical work in the lab, to Miles Egan for readily helping with my chemistry questions, to Roy Tom for machining and fabricating essential custom parts and to Ava Dykes, Lloyd Muzangawa, Dalton Muchow, Barry Lienert, Charles Helsley and Lydie Bonal for one way or another helping me obtain the data presented in this work. John Porter also was instrumental in developing and writing the theory used to obtain the cross sections of different chemicals.

During graduate school I had the privilege of also working and collaborating with the people in the high pressure laboratory. Although not directly involving the results in this dissertation, the experience has enormously expanded my area of expertise. I am thankful for the advice and teachings of Pavel Zinin, and the patience and support of Lu-Chang Ming. The assistance provided by John Balogh fixing lasers and other technical work is also greatly appreciated. Thanks also to Shoko Odake, Ru Jia, Katherine Burgess, Xiuru Liu, Przemyslaw Dera and Yi Hu.

I would like to express my very great appreciation to the faculty and staff of GG and HIGP for all their help, teachings and helpful discussions. I am very thankful to Patricia Fryer for serving in all my committees and helping me as a student; to Edward R. D. Scott for introducing me to shocked meteorites, coauthoring with me and for serving in my committee; and to Neil Frazer for helping me stay on track. Thanks to Eric Hellebrand for his invaluable help with the EPMA measurements. The faculty taught me almost all I know about geology; I am grateful to Clint Conrad, John Mahoney, Jeffrey Taylor, Paul Lucey, Paul Wessel, Peter Englert, Janet Becker, Garret Ito, Stephen Martel, Steven Stanley, Ali El-Kady, Cecily Wolfe, Henrieta Dulai,

Kathleen Ruthenberg, and anyone I might be forgetting. I also want to say thanks to Stephen Masutani and Pui Lam for serving as outside members of my committee. Thanks also to Grace Furuya, Vi Nakahara, Rena Lefevre, Susan Vangorder, Lily Shao, and Leona Anthony for helping me with all the forms and administrative procedures. I would also like to thank Nancy Hulbirt and Brooks Bays for their help with figures and design, and to Mai Izumi for her help with editing.

I am also thankful to all my fellow graduate students for helpful discussions and moral support along the way, especially to Patrick Gasda, Mathews Paret, Regan Austin, Myriam Telus, and David Frank. I thank Genesis Berlanga for the last minute confidence push. Thanks to everyone for giving me useful comments and engaging in helpful discussions, those mentioned above, other coauthors and collaborators (Lori Kamemoto, Nirmal Lamsal, Anne M. Alvarez, Lisa Tatsumi-Petrochilos, Julia Hammer, Mike Fuller, Samuel Clegg, Roger Wiens, and Vitalyi Gusev), Zhidong Xie and another three anonymous reviewers.

This dissertation has been partially funded by grants from NASA (PIDDP, MIDP, SuperCam Mars 2020, EPSCoR) and ONR.

My sincere thanks also go to Fernando Rull for initially introducing me to Raman spectroscopy, and then to Raman spectroscopy applied to planetary exploration. I'd like to extend this thank you to everyone who encouraged me to get to this point back at University of Valladolid in Spain and its astronomy club, especially to Pablo Sobrón and José Antonio Manrique.

Finally, I am especially thankful for my parents Carlos and Alicia for all their encouragement and support, my sister Tatiana, and all my friends, new and old. And more importantly to my wife Noriko; I thank her for all her love, support, encouragement, hard work and pure fun at the same time. I couldn't imagine a better partner. The last thank you goes to our little son, Kai, for filling with bundles of joy this hard last one year and a half.

# ABSTRACT

The sharp spectral features of Raman spectra are widely recognized to provide unequivocal and accurate chemical characterization of organic and inorganic compounds. Therefore Raman spectroscopy can be used to detect minerals, water bearing minerals, organic and biological materials and biomarkers in the context of planetary science. This dissertation extends the applicability of the Raman technique both laboratory based micro-Raman and remote Raman sensing ahead of planetary exploration missions to Mars employing Raman spectrometers. The interpretation of Raman imaging from a meteorite taken with a micro-Raman system revealed a close correlation between the blue color in natural ringwoodite and a new observed Raman peak that shows strong resonance Raman enhancement. The data suggest that ringwoodite exists both in the spinel structure and in the partially inverse spinel structure. In the field of remote Raman, this dissertation provides carefully derived Raman cross-section values for various organic liquids and inorganic polyatomic ions in aqueous solutions that will be useful for estimating detection capabilities of 532 nm excitation remote Raman systems for planetary exploration. Suitability of remote 532 nm Raman systems for future applications is explored. A portable, compact time-resolved instrument using a 3-inch diameter telescope is used it to demonstrate daytime detection of amino acids and nucleobases from a distance of 8 m. The measurements with a larger 8-inch Raman system demonstrate that it is possible to acquire good quality Raman spectra of various materials from a 430 meter remote distance during daylight with detection times of 10 seconds, and in some cases as short as 1 second, during daylight and in a realistic outdoor context. To my knowledge, these are the only remote Raman spectra at this distance that provide unambiguous detection of compounds important for planetary science, such as water and water ice, dry ice, sulfur, sulfates, various minerals and organics, and atmospheric gases. This dissertation demonstrates the large potential of micro-Raman investigations and the significant improvement of the remote Raman technique as well as its suitability for Solar System exploration.

# MOTIVATION

These are active and exciting times for Raman spectroscopy in planetary science as micro-Raman laboratory systems are more powerful and versatile than ever and several Raman systems are planned to fly to Mars. The European Space Agency has included a micro-Raman spectrometer in the payload of the Exomars 2018 mission (Rull Perez and Maurice, 2016) and the National Aeronautics and Space Administration is planning to add Raman capabilities in both the Supercam and SHERLOC instruments in the payload of the Mars 2020 rover mission (Beegle and Bhartia, 2016; Wiens and Maurice, 2016).

In recent years, Remote Raman spectroscopy has been developing in parallel with the more traditional micro-Raman technique (Hirschfeld, 1974; Sharma et al., 2002) and our group at the University of Hawai‘i, lead by Shiv K. Sharma, has been pioneering the technique since the early 2000s. Thanks to the equipment and experience of the Raman Spectroscopy Laboratory at the University of Hawai‘i, I feel that remote Raman systems can be developed, new techniques established, and improvement in our understanding on Raman sensing, to provide the community with tools and data to better interpret future measurements to be coming from outside the Earth.

# TABLE OF CONTENTS

# LIST OF TABLES

# LIST OF FIGURES

# CHAPTER 1: INTRODUCTION

## 1.1 Raman Spectroscopy

### 1.1.1 Historical background

The interaction of light with matter results in the phenomena of reflection, absorption, transmission, and scattering. In some cases this interaction also results in fluorescence emissions (photoluminescence) at longer wavelengths than that of the incident light. In 1852 Sir George Gabriel Stokes famously described detailed experimental studies on several samples, both organic (including quinine) and inorganic (including fluor spar or fluorite mineral, an impure $CaF_2$) and identified a common phenomenon he called dispersive reflectance - where the wavelength of the dispersed light was longer than that of incident light (Stokes, 1852). The shift in the wavelength is referred to as the Stokes shift (Figure 1) and the phenomenon is known today as fluorescence.

There is also a long history of research on the phenomena of scattering of light. Lord Rayleigh (John Strutt), a British physicist, published his theory of elastic scattering (known as Rayleigh scattering) in several papers between 1870 and 1900. In Rayleigh scattering of light by atoms or molecules, which are much smaller than the wavelength of light, there is no change in the wavelength of incident light. The scattered light has a strong wavelength dependence ($\sim\lambda^{-4}$), which means that shorter (blue) wavelengths are scattered more strongly than longer (red) wavelengths. Rayleigh scattering of sunlight in the atmosphere causes diffuse sky radiation, which is responsible for the blue color of the sky (Rayleigh, 1899).

Raman spectroscopy is based on the Raman Effect. The Raman Effect was predicted in 1923 as an inelastic scattering of light (Smekal, 1923), with further contributions of some of the physicists that developed quantum mechanics (Dirac, 1927; Kramers and Heisenberg, 1925; Schrödinger, 1926). The effect was first observed experimentally in 1928 by Sir C.V. Raman, an Indian physicist, during the course of extended research on the molecular scattering of light in liquids (Raman and Krishnan, 1928). The effect was observed independently in quartz crystals by Landsberg and Mandelstam (1928) and the years 1928 and 1929 saw the light of extensive research on the topic (Menzies, 1930). For this discovery and the first publication of a spectrum of scattered light with frequency shifted lines, Raman was awarded the Nobel Prize in 1930 and the effect is named after him as the Raman Effect.

### 1.1.2 Basic Theory

The Raman Effect is observed when a monochromatic light of frequency $\nu_0$ is incident on a transparent sample and the spectrum of the scattered light shows, in addition to the Rayleigh line, a pattern of lines of shifted frequency - the Raman spectrum. The pattern on the low frequency side of the exciting light ($-\Delta\nu$), which is negative or longer in wavelength, resembles the Stokes shift found in luminescence. For this reason they are referred to as Stokes-Raman lines. The pattern is mirrored by an identical pattern on the high frequency side ($\Delta\nu$) positive or shorter in wavelength, which is referred to as anti-Stokes Raman lines. The intensities of the Stokes Raman lines are greater than those of the anti-Stokes Raman lines. The lifetime of Raman scattering ~$10^{-13}$ second, and is much shorter than the lifetime of most fluorescence.

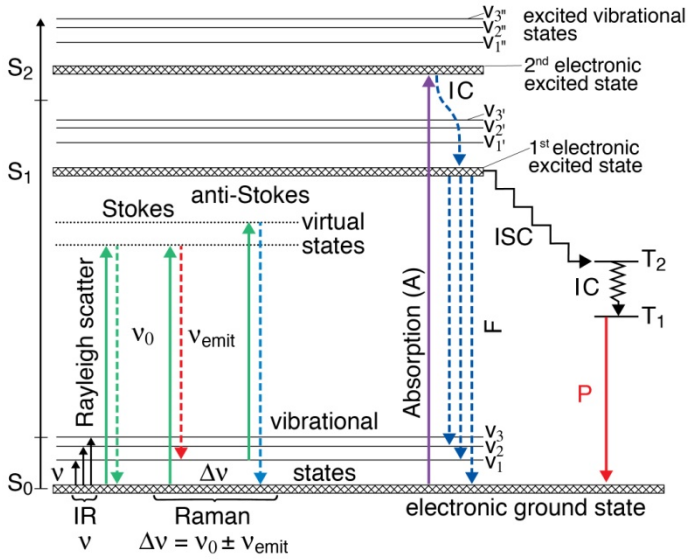


Figure 1.1: Jabłoński energy-level diagram showing the real electronic excited states involved in fluorescence and phosphorescence, and virtual states involved in elastic (Rayleigh) and inelastic (Raman) scattering. IC is internal conversion, ISC is intersystem crossing, F is fluorescence (lifetime $10\text{x}10^{-12}$ - $10^{-9}$ s), and P is phosphorescence (lifetime $10^{-3}$ - $10^{2}$ s).

For any molecular bond, the individual atoms are confined to specific vibrational modes whose energies are quantized. For example, the energy of a particular vibrational mode in a diatomic molecule can be given by the solution of the Schrödinger equation

$$\frac{d^2\Psi}{dq^2} + \frac{8\pi^2\mu}{h^2}\left(E - \frac{1}{2}KQ^2\right)\Psi = 0 \qquad (1.1)$$

where 'Ψ' is the wave function of the quantum system, 'Q' is the atomic displacement from the equilibrium position, 'μ' is the reduced mass of the system (i.e., for a diatomic molecule with molecular masses $m_1$ and $m_2$, $\mu = (m_1m_2)/(m_1+m_2)$), 'h' is the Planck's constant, and 'K' is the force constant of the molecular bond. Solving for the condition that the wave function must be single valued, the eigenvalues are

$$E_v = (v+1/2)\, h\nu_{vib} \qquad (1.2)$$

where 'v' is the vibrational quantum number, and '$\nu_{vib}$' is the vibrational frequency; and the frequency of vibration is given by

$$\nu_{vib} = \frac{1}{2\pi}\sqrt{\frac{K}{\mu}} \qquad (1.3).$$

Raman scattering can be described in terms of the discrete energy states of each molecular vibrational mode. For this we can consider a vibrational energy diagram (Fig. 1.1). There, each discrete vibrational state corresponds to the vibrational quantum number 'v' in equation 1.2. Contiguous energy levels increase or decrease in energy by one quantum number; hence $\Delta E = h\nu_{vib}$.

At low to moderate temperatures, most of the molecules will exist in the ground vibrational quantum state (v = 0), while the rest of the molecules will exist in higher vibrational states according to the Boltzmann's distribution function (Equation 1.4). Molecules in upper vibrational quantum states (e.g., v = 1) vibrate at the fundamental frequency $\nu_{vib}$; however, the probability of finding the atoms displaced from their equilibrium position increases with

increasing quantum number. Raman scattering can also be interpreted as a change in vibrational energy state caused by the interaction with an incident photon. An oscillating dipole moment is induced in the molecular system along with the incident light wave putting the molecular system in a virtual energy state whose energy is higher than the vibrational energies (Fig. 1.1, Jabłoński diagram modified to show vibrational energies (Jabłoński, 1933)). Depending on the photon energy, the energy level of the virtual state is usually much greater than the energy of the vibrational states, but is not necessarily coinciding with any particular electronic excited state. The most likely outcome of this process is the molecule staying in its ground electronic state (Hahn, 2007). However, during the interaction with the incident photon and depending on the energy of the photon, some quantum of energy equal to that of the vibrational mode may be given or taken to the molecule vibrations (Fig. 1.1). This phenomenon of inelastic scattering is referred to as spontaneous or normal Raman scattering to distinguish it from stimulated Raman scattering, which is a non-linear optical effect.

After this scattering event, the remaining photon energy, which is now less (or more) than that of the incident photon, is emitted from the molecule as electromagnetic radiation. This inelastically scattered radiation is the Raman emission.

The intensity ratio of the Stokes Raman to anti-Stokes Raman lines of the sample depends on the temperature of the sample, i.e., the population of molecules in the ground and excited states, according to following equation:

$$\frac{I_{Stokes}}{I_{anti-Stokes}} = \frac{(\nu_0 - \Delta\nu)^4}{(\nu_0 + \Delta\nu)^4} e^{(-hc\Delta\nu/kT)} \qquad (1.4)$$

where ‘h’ is the Planck’s constant, ‘k’ is the Boltzmann’s constant, ‘T’ is the temperature and ‘Δν’is the vibrational energy of the molecule ($\nu_{vib}$). Based on this equation, the Stokes to anti-Stokes ratio of Raman lines can be used to determine the temperature of the sample.
The phenomena of Rayleigh and Raman scattering can be explained, in part, by classic electromagnetic theory (Herzberg, 1945). Light scattering may be considered as an interaction between an electromagnetic wave with matter (solid, liquid or gas) that perturbs the electron clouds within the constituent molecules with the same frequency ($\nu_0$) as the electric field of the

incident wave. The perturbation of the electron cloud results in the periodic separation of the center of positive and negative charges within the molecules, which produces an induced dipole. The oscillating induced dipole moment manifests as a source of electromagnetic radiation, thereby resulting in scattered light. For example, a hypothetical atom, with a spherical symmetric electron cloud, has no permanent dipole moment. When the atom is placed in an oscillating field of electromagnetic light waves of frequency $\nu_0$, i.e., $E = E_0 \cos(2\pi\nu_0 t)$, it will induce a dipole moment P given by the following equation

$$P = \alpha E_0 \cos 2\pi\nu_0 t \qquad (1.5)$$

where '$\alpha$' is a constant of proportionality (known as polarizability), '$E_0$' is the magnitude of the electric field, and '$\nu_0$' is the frequency in Hz ($\nu = c/\lambda$, where c is the speed of light, and $\lambda$ is the wavelength) of the incident light, and 't' is the time.

The polarizability is not constant because certain vibrations and rotations of the molecule can cause it to vary. For example, during the vibration of a diatomic molecule, the molecular shape is alternately compressed and extended. The electron cloud is not identical at the extremes of the vibration, so a change in polarizability will result. For small displacements the polarizability of a diatomic molecule can be given as

$$\alpha = \alpha_0 + \left(\frac{\delta\alpha}{\delta Q}\right) dQ + \ldots \qquad (1.6)$$

where 'dQ' is the difference between the inter-nuclear distance and the equilibrium inter-nuclear distance at a given time, and '$\delta\alpha/\delta Q$' is the rate of change of $\alpha$ with respect to dQ. If the vibration is considered harmonic, dQ is given by

$$dq = Q_0 \cos 2\pi\nu_{vib} t \qquad (1.7)$$

where '$Q_0$' is the maximum displacement about the equilibrium position and $\nu_{vib}$ is the vibrational frequency.

Substituting the values of α and dQ from Equations 1.6 and 1.7 yields,

$$P = \alpha_0 E_0 \cos 2\pi\nu_0 t + \left(\frac{\delta\alpha}{\delta Q}\right) E_0 Q q_0 \cos 2\pi\nu_0 t \cos 2\pi\nu_{vib} t \qquad (1.8).$$

Using trigonometry relations, the above equation can be written as

$$P = \alpha_0 E_0 \cos 2\pi\nu_0 t + \frac{E_0 Q_0}{2}\left(\frac{\delta\alpha}{\delta Q}\right) [\{\cos 2\pi(\nu_0 + \nu_{vib})t\} + \cos\{2\pi(\nu_0 - \nu_{vib})t\}] \quad (1.9).$$

It follows from Equation (1.9) that the electrical field of the incident light interacts with the molecules in the medium and induces oscillating polarizability components with frequencies $\nu_0$, $\nu_0$-$\nu_{vib}$ and $\nu_0$+$\nu_{vib}$, which result in scattering at the same frequencies. The spectrum of the scattered light will not only contain the line corresponding to incident light $\nu_0$ (Rayleigh scattering), but also two modified lines corresponding to the frequencies $\nu_0 \pm \nu_{vib}$ (Raman scattering). The intensity of the Rayleigh line depends on the square of the amplitude, i.e., $(E_0\alpha_0)^2$, and the intensities of the Raman lines depend on $(E_0 q_0/2)^2 (\delta\alpha/\delta Q)^2$, where $\delta\alpha/\delta Q$ is the rate of change at for changes in α a given normal mode of vibration. A necessary condition for Raman scattering is that $\delta\alpha/\delta Q$ must be non-zero. This constitutes the selection rule of Raman spectroscopy: "For a molecular vibration to be Raman active, the polarizability must be changed during the vibration." Thus we have a classical explanation of Stokes Raman and anti-Stokes Raman lines. The observed intensity of Raman scattering is proportional to the cross section β which is closely related to the change in polarizability $\delta\alpha/\delta Q$. According to the classical theory, however, the intensities of a Stokes Raman line and corresponding anti-Stokes Raman line should be the same. The limitation of classical theory results in incorrect relative intensity of the Stokes Raman line, as compared with the corresponding anti-Stokes Raman line, and instead needs to be explained on the quantized nature of the vibrational energy levels.

The observed intensity of Raman scattering is proportional to the cross section, $\beta_j$, with units of square centimeters per molecule. It follows from the Raman theory that the magnitude of $\beta_j$ is related to the change in polarizability $\delta\alpha/\delta Q$ (Tang and Albrecht, 1970). One consequence of this theory is that the Raman intensity for modern Raman spectrometers, which measure

photons/second in the absence of resonance Raman Effect, increases as the excitation wavelength decreases following the 4th power excitation frequency dependence of the Raman cross section given by

$$\beta_j = \beta_j^0 \upsilon^0 \left(\upsilon^0 - \upsilon_j\right)^3 \qquad (1.10)$$

where $\beta_j^0$ is the frequency independent cross section of the $j^{th}$ vibrational mode, $\upsilon^0$ is the wavenumber of the excitation laser wavelength, and $\upsilon_j$ is the wavenumber of the Raman peak j (McCreery, 2002).

### 1.1.3 Applications for planetary science

As described above, in the Raman Effect, an incident photon scatters inelastically upon interaction with molecules, and the scattered radiation carries information on vibrational and rotational energy levels of molecules and lattice vibrations energy levels. Thus, Raman spectra can potentially identify a wide range of chemical compounds, ranging from minerals to biological products.

Initially Raman spectroscopy was considered a physics curiosity until the invention of lasers, even though several Raman studies of pure components (solids, liquids, gases) were carried out at the macroscopic scale using mercury emission lamps (Herzberg, 1945). This was mainly because of the low efficiency of normal Raman scattering. A typical total Raman scattering cross section is on the order of $10^{-29}$ $cm^2$ per molecule, whereas typical cross-sections for absorption in ultraviolet and infrared are around $10^{-18}$ and $10^{-21}$ $cm^2$ per molecule, respectively. Lasers that became available during the 1960s were able to provide high irradiance of monochromatic light onto the sample for recording the Raman spectra. Moreover, Raman spectrometers constructed before the 80s were large, expensive, and not suitable for onsite analysis. With the development of lasers and detectors starting in the 60s and into the 80s, it was a natural consequence that Raman spectroscopy was applied to meteorite minerals phases once the technique was established as a practical method of chemical analysis (Bild and Tallant, 1984; Heymann, 1987). Not surprisingly, Raman spectroscopy helped prove the impact origin of multiple cratering events (Gucsik et al., 2003; Halvorson and McHone, 1992), and permitted recognition of shocked minerals as a proof of impacts in meteorites (Boyer et al., 1985;

Miyahara et al., 2014). Currently Raman spectroscopy is used as a powerful characterization tool in shocked meteorites to distinguish among shock-created mineral polymorphs (Chen et al., 2007a; Wang et al., 2004; Zhang et al., 2006). One of the polymorph families found in meteorites is also of particular interest to Earth sciences. Wadsleyite and ringwoodite are polymorphs of the common mineral olivine. All three phases constitute a large fraction of the upper mantle of the Earth (Binns et al., 1969; Ringwood, 1975) and their physico-chemical properties are key to understanding the behavior of the Earth's interior. Backed by the experience and resources of the Raman systems and laboratories, I undertook a thorough Raman study of a shocked ordinary chondrite with wide melt veins and large ringwoodite crystals. I went beyond simple Raman identification into providing chemical and structural insight on both ringwoodite, and other shock-induced mineral phases.

Raman spectrometers have significantly profited from technical development and it is now possible to construct low-cost, battery-powered, portable Raman spectrometers, which have many of the spectral capabilities of laboratory-based systems (e.g., Dubessy et al., 2012). The recent spectacular advances in the construction of Raman spectrometers are well illustrated by the low mass (~ 1.5 Kg) of the Raman spectrometer for the next European and American rover missions to Mars (Beegle and Bhartia, 2016; Rull Perez and Maurice, 2016; Wiens and Maurice, 2016).

### 1.1.4 Resonance Raman Spectroscopy

Resonance Raman spectroscopy, which is used in Chapter 2, is a variant of 'normal' Raman spectroscopy. Raman spectroscopy is typically performed using laser sources that have energy above the vibrational or rotational energies of the molecule but far below the first electronic excited state. Resonance Raman scattering takes place when the laser's energy nears that of an electronic excited state (e.g., $1^{st}$ or $2^{nd}$ electronic excited state in Fig. 1.1). In such a case, the Raman bands originating in the excited electronic transition may show very strong enhancements, with intensities $10^3$ to $10^5$ higher than that the predicted by the $\nu_0^4$ rule. The term pre-resonance Raman scattering is commonly used when the excitation energy is in the vicinity of the electronic excited state. Resonance Raman adds sensitivity to Raman spectroscopy and allows the identification of samples with concentrations as low as low as $10^{-8}$ M (molar). In resonance Raman the excitation wavelength is chosen to overlap with (or be very close to) an

electronic transition, which usually occurs in an area of UV-visible absorption. The resonance Raman lines, thus, are selectively enhanced and produce simpler spectra and allow for assignments of the vibrations of the excited chromophores and facilitate interpretation of features produced by the electronic transitions in the absorption spectra. The usefulness of resonance Raman spectroscopy for studying aqueous samples, especially biological samples, was appreciated early on. Raman enhancement has been observed in several organic molecules, such as hemoglobin, with transitions in the 400-600 nm range. Strekas and Spiro (1972) demonstrated the usefulness of the resonance Raman effect in selective studies of the chromophoric hemes of hemoglobin and myoglobin. Resonance Raman with tunable visible lasers is used to study heme protein structure and function (Spiro et al., 1990) and elucidate the photochemical mechanisms of visual pigments, such as rhodopsin (Mathies et al., 1987). In minerals, Raman enhancement has been observed for the iron containing oxides hematite ($\alpha$-$Fe_2O_3$), maghemite ($\gamma$-$Fe_2O_3$) and magnetite ($Fe_3O_4$) (de Faria et al., 1997). For this group of minerals, pre-resonance Raman occurs with 636 nm excitation caused by a spectral absorption band located near 640 nm. This band has been identified as the result of the $^6A_1(^6S) \rightarrow {}^4T_2(^4G)$ ligand field transitions of octahedrally coordinated $Fe^{3+}$ (Cornell and Schwertmann, 2003). Raman resonance has also been observed in ringwoodite, along with Fe-originated absorption bands in the optical spectra (Acosta-Maeda et al., 2013). These have been assigned to the transition $^5T_{2g} \rightarrow {}^5E_g$ of $^{VI}Fe^{2+}$ split by the trigonal distortion or Jahn-Teller effect (Taran et al., 2009).

The change in polarizabilty produced by an electronic transition gives rise to the enhanced Raman effect and can be expressed as a function of two "terms" of resonance, A and B. According to the Albrecht theory, the A-term resonance can only be seen for totally symmetric modes and the B-term can contribute to the cross section in non-totally symmetric modes.

The intensity of a Raman band with a contribution from the electronic transition m→n is, in theory (Albrecht, 1961; Ferraro et al., 2003; Tang and Albrecht, 1970),

$$I_{mn} = C \cdot I_o \cdot (\upsilon_0 - \upsilon_{mn})^4 \sum_{p\sigma} \left[ (\alpha_{\rho\sigma})_{mn} \right]^2 \quad (1.11)$$

where m and n are the initial and final electronic states. This equation also expresses the $\nu_0^4$ rule. $(\alpha_{\rho\sigma})_{mn}$ represents the polabizability change caused by the m→e→n transition (where e is an electronic excited state) and ρ and σ are the three components x-y-z of the polarizability tensor. This depends on the frequency difference between the states $\upsilon_{em}$ and $\upsilon_{en}$ as

$$(\alpha_{\rho\sigma})_{mn} = \frac{1}{h}\sum_e \left( \frac{M_{me}M_{en}}{\upsilon_{em} - \upsilon_0 + i\Gamma_e} + \frac{M_{me}M_{en}}{\upsilon_{en} + \upsilon_0 + i\Gamma_e} \right) \qquad (1.12)$$

where h is the Planck's constant and the $M_s$ are the electronic transition moments. $\Gamma_e$ is the band width of the state e, and $i\Gamma_e$ is named the dumping constant. In Raman scattering, $\upsilon_0$ is usually $\upsilon_0 << \upsilon_{em}$, and the Raman intensity follows the $\nu_0^4$ rule. The first term in parenthesis in the equation becomes very large as $\upsilon_0$ approaches $\upsilon_{em}$ and the intensity of the band at $\upsilon_0$-$\upsilon_{em}$ greatly increases. This resonance term gives rise to the Resonance Raman scattering. The polarizability can be expressed in two terms, A and B, by stating the total wavefunction as the product of the electronic and vibrational wavefunctions.

$$(\alpha_{\rho\sigma})_{mn} \cong A + B \qquad (1.13)$$

where the A term is

$$A \cong M_{me}{}^2 \frac{1}{h}\sum_{\upsilon} \frac{\langle j|\upsilon\rangle\langle\upsilon|i\rangle}{\upsilon_{\upsilon i} - \upsilon_0 + i\Gamma_\upsilon} \qquad (1.14)$$

where $M_e$ is the pure electronic transition moments for the excited state e of which υ is a vibrational level. The A term becomes larger given the resonance condition $\upsilon_0 \rightarrow \upsilon_{\upsilon i}$ and as the electronic absorption becomes stronger, yielding a larger $M_e$. Because the vibrational wavefunctions are orthogonal, one of the integrals becomes 0 unless the equilibrium position is shifted with the electronic excitation. This happens only in totally symmetric vibrations, hence the A term is only observed for totally symmetric Raman modes. The B term involves two electronic excited states e and s, and can be expressed as

$$B \cong M_e' M_e \frac{1}{h} \sum_v \frac{\langle j|Q|v\rangle\langle v|i\rangle + \langle j|v\rangle\langle v|Q|j\rangle}{\upsilon_{vi} - \upsilon_0 + i\Gamma_v} \qquad (1.15)$$

where

$$M_e' = \mu_s \frac{\langle s|\partial H / \partial Q|e\rangle}{\langle \upsilon_s - \upsilon_e \rangle} \qquad (1.16)$$

and where $\upsilon_s$ and $\mu_s$ are the frequency and transition dipole moment of the second excited state. The numerator of the B term contains vibrational overlaps integrals dependent of Q (normal coordinate of the vibration) and Franck-Condon overlap integrals. Therefore it does not become 0 when the vibrations are not totally symmetric. The electronic hamiltonian H is contained in the vibronic coupling operator <s|∂H/∂Q|e>; the B term is not 0 when proper symmetry coordinates are chosen and resonance Raman Effect can be observed with only a B term contribution.

## 1.2. Advanced Raman Spectroscopy Methods

### 1.2.1 Micro-Raman spectroscopy

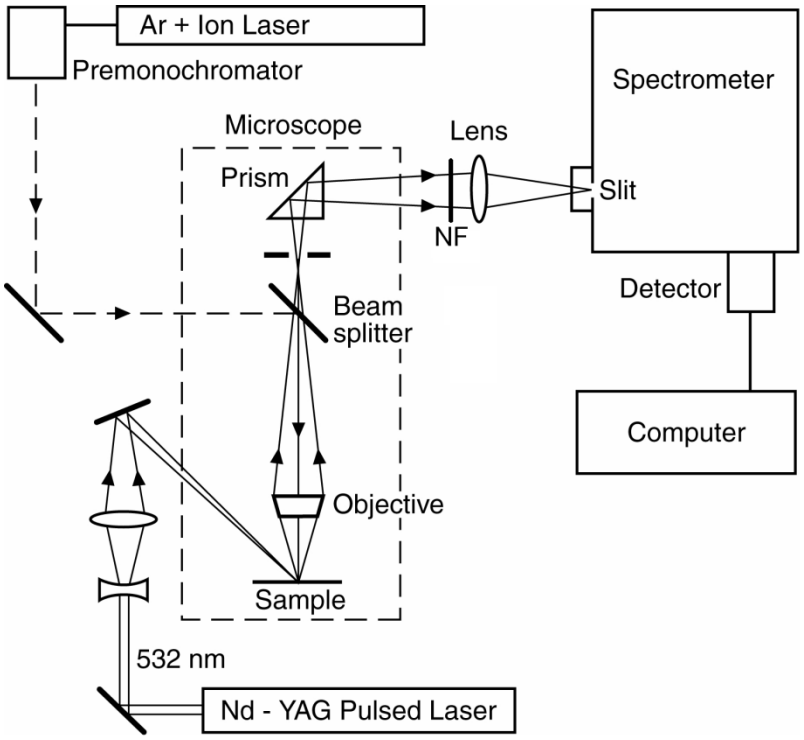


Figure 1.2: Schematics of micro-Raman system with 180° and 135° scattering geometry with a CW Ar-ion laser and a pulse 532 nm laser, respectively, NF: notch filter.

The schematics of a micro-Raman system (Fig. 1.2) show a continuous wave (CW) Ar-ion laser, 488 and 514.5 nm radiation, used in 180-degree geometry, and a pulsed frequency-doubled 532 nm laser radiation from an Nd:YAG laser are used in an oblique (typically 45-degree) angle excitation geometry. The principal advantage of micro-Raman spectroscopy is the ability to make measurements of a region of the sample as small as the focused laser spot. The laser can be focused to a diffraction limited spot and the system will accept light from other areas such as above and below the nominal focus area in the optical axis direction.

Typical laser spots are on the order of 2-3 μm for a 50X VIS microscope objective and 514.5 nm Ar CW laser excitation. The necessary components to obtain a Raman spectrum are a

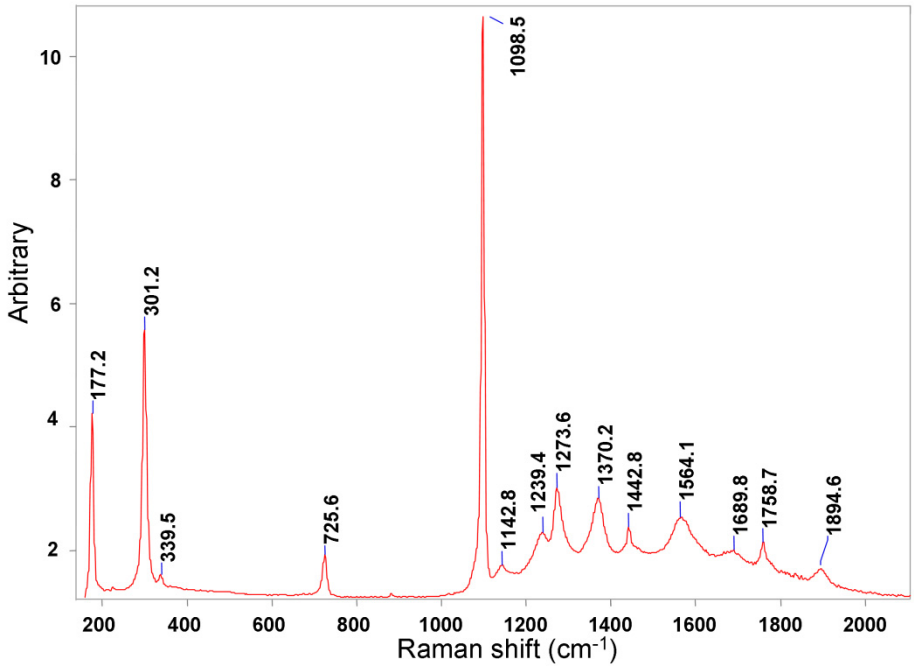


Figure 1.3: Black spot on clean brown surface of colonized "red" carbonate from Little Red Hill, CA, crystal: dolomite and unidentified peaks after 1100cm$^{-1}$. Exposure: 10 seconds, 10 accumulations, 13mW, 785 nm excitation.

monochromatic excitation source, a spectrometer fitted with a detector, and a way to reject the intense Rayleigh scattering. In modern micro-Raman spectrometry, a microscope is used both to excite the sample and collect the scattered light with 180° geometry. A holographic notch-beam splitter is used to direct the laser towards the sample and to allow the inelastically scattered radiation to travel towards the spectrometer. Advances in notch and sharp edge filters have significantly reduced the size and increased the efficiency of the dispersive Raman systems. SuperNotch filters allow the rejection of the Rayleigh scattered light by a factor of ~$10^8$. These advances have been used in a number of modern commercial research-grade Raman spectrometers, and to develop miniature Raman spectrometers for space applications (Gasda et al., 2015). The work presented in this dissertation, is from use of a number of Raman systems at the Hawai'i Institute of Geophysics and Planetology. These include a Kaiser Raman RXN1™ Microprobe with 785 nm laser excitation; a Renishaw InVia micro-Raman system with 224 nm (UV), 514.5 nm (Green) and 830 nm (NIR) laser excitation wavelengths; a WITec alphaR 300

Raman microscope with 532 nm (green) and a 632 nm (red) laser excitations; and older SPEX spectrometer fitted with Ar and Kr ion lasers.

Motorized and piezo-electric drive stages (e.g., Prior Scientific) can be added to the microscope setting. This allows moving the sample and taking spectra from specific locations along a pattern to generate Raman images, which display the spatial distribution of a Raman signature signal.

A variety of wavelengths can be used with micro-Raman systems. Typically Ar lasers emission lines have been successfully used (e.g., 488 and 514.5 nm, or 244 nm with wavelength doubling). Newer semiconductor lasers provide reliable excitation at NIR wavelengths such as 785 and 830 nm. Tunable lasers are available (e.g., Ti:sapphire laser), especially suitable to look for resonances in resonance Raman spectroscopy. The availability of several excitation wavelengths allows selecting an ideal wavelength for each application. This can be invaluable in obtaining Raman spectra in resonance or pre-resonance areas, in detecting and avoiding fluorescence, or taking advantage of the theoretical higher Raman intensity at lower wavelengths.

Microscope glass slides are commonly used to prepare meteorite fragments for analysis. These are easily measured in micro-Raman systems with magnifications up to 100X and spatial resolution up to 1.5 μm. However, care must be taken not to mistake glass or glue Raman and luminescence signals for mineral Raman signals. As an example for how to identify luminescence peaks and distinguish them from the Raman peaks using different excitation wavelengths, we can look at the spectrum (Fig. 1.3) of an astrobiology analog sample (colonized "red" carbonate from Little Red Hill, CA). The spectrum shows the characteristic signature peaks of dolomite (177, 301 and 1098 $cm^{-1}$) and some unidentified peaks in the range 1100 to 2000 $cm^{-1}$. Some of these peaks appear to come from induced phosphorescence from trace rare earth elements or from biologic fluorescence. If we take the spectrum at the same point with two different excitation wavelengths, 785 and 830 nm, the luminescence signals will be expected to shift in wavenumber, but when represented in the wavelength scale they will remain at the same positions while Raman peaks will be shifted

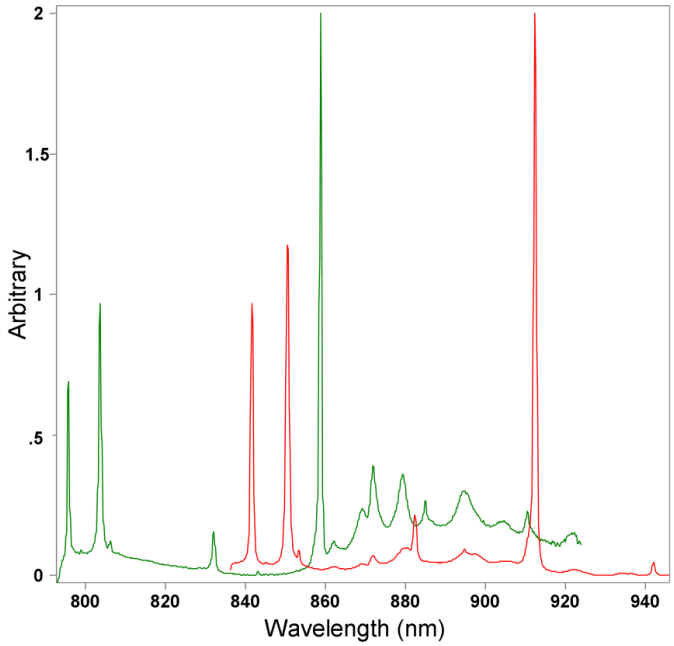


Figure 1.4: Black spot on clean brown surface of colonized "red" carbonate from Little Red Hill, CA, crystal: dolomite and unidentified peaks after 1100 $cm^{-1}$. Green: exposure 10 seconds; 10 accumulations; 13 mW; and 785 nm excitation. Red: exposure 5 seconds; 10 accumulations; 10 mW; 830 nm excitation wavelengths.

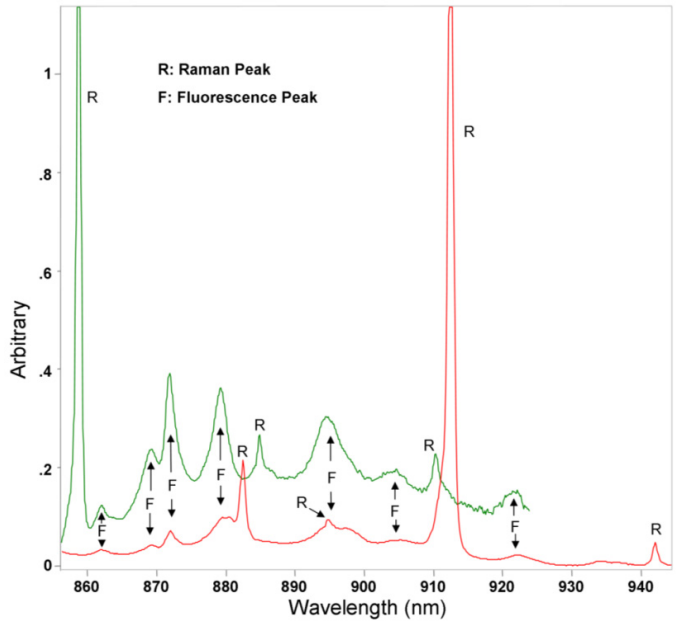


Figure 1.5: Raman and luminescence assignment of peaks recorded in the spectra of the colonized "red" carbonate from Little Red Hill, CA, shown in Fig. 1.4.

according to the wavenumber increment respect to the excitation wavelength. We can see in (Fig. 1.4) how the Raman peaks are displaced in wavelength because they originate from a vibrational energy induced shift from the excitation wavelength, in this case 785 and 830 nm. Luminescence, however, originates from electronic excited states and its signals are fixed in the wavelength domain. An enlarged section (Fig. 1.5) of the Raman-luminescence mixed range between 850 and 950 nm, from which luminescence and Raman peaks can be easily distinguished, shows that most of the peaks in the area are indeed due to luminescence.

### 1.2.2 Remote Raman instrumentation for daytime Raman detection

Remote Raman systems add new traits to the Raman technique. The potential for performing Raman analysis remotely was envisioned in the 60s (Cooney, 1965) and remote Raman was first applied experimentally by Hirschfeld for long-range atmospheric measurements (Hirschfeld, 1974). Remote Raman measurements were first taken with a small system constructed in the 90s (Angel et al., 1992) with CW lasers. In recent years, several research teams have been developing remote Raman systems in a wide range of applications (Carter et al., 2005a; Gasda et al., 2015; Moros et al., 2011) and measurements distances have increased into the km range (Aggarwal et al., 2010). Earlier systems were based on CW lasers that require measuring in dark conditions. However, modern systems are fitted with pulsed lasers and gated detectors that allow for measurements during daytime (Sharma et al., 2006). For planetary science applications, larger measurement distances increase the effective exploration area of a planetary rover, saving mission time and increasing the number of accessible targets (Abedin et al., 2015; Angel et al., 2012; Sharma et al., 2006). A remote Raman system with daytime measurement capability and a distance capability on the order of hundreds of meters could also be developed (Klein et al., 2004) and can help best determine optimal sampling sites in future asteroid sample return missions such as NASA's OSIRIX-Rex (Nakamura-Messenger et al., 2014), or discriminate between ices and different sulfates in Europa from a low orbit (Carlson et al., 2009). A remote Raman system with Raman imaging capability would also have potential for determining mineral distribution and composition on a rock surface by comparing a set of Raman images collected for various minerals.

The components of a remote Raman system are similar to those of a micro-Raman system: a laser, collection optics, optical filter and a spectrometer fitted with a detector. The

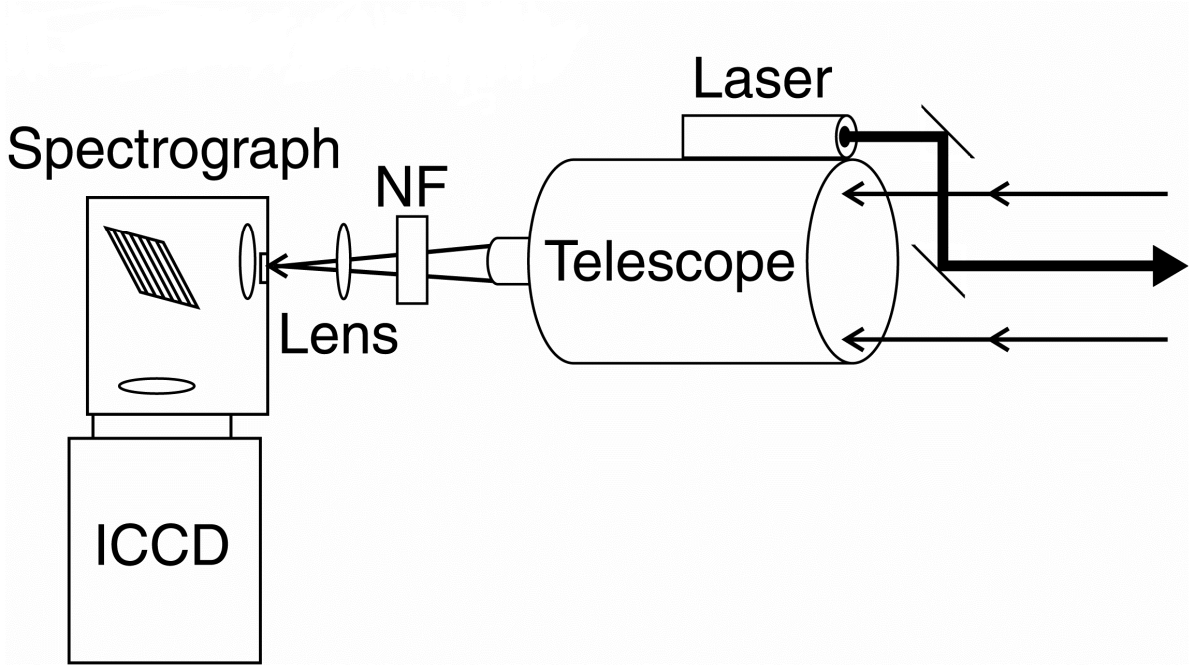


Figure 1.6: Schematics of a typical coaxial directly coupled Remote Raman system. NF: Laser blocking filter (notch filter).

major difference between remote and micro-Raman systems is the incorporation of a telescope for the collection of the scattered radiation. The generated Raman signal spreads almost spherically from the excitation spot (Damen et al., 1965), which in turn makes the irradiance of the measured Raman signal inversely proportional to the square of the measurement distance (Measures, 1992). The use of a telescope or other optics with large aperture is intended to increase the solid angle at which the system 'observes' the excitation spot, allowing analysis of a target meters away from the system. In other words, larger collection optics increase the collection of scattered light over larger solid angle to compensate the decreased photon flux at large measurement distance. Modern daytime capable remote Raman systems are fitted with gated lasers and detectors which can perform fast measurements of planetary analogs under daylight at increasing distances (Misra et al., 2012; Misra et al., 2011; Rull et al., 2011; Sharma et al., 2006; Sharma et al., 2009). The technique employs lasers and detectors that can send and receive signals in nanoseconds, allowing for full Raman spectrum measurements while minimizing daylight background and some of the long-lived luminescence that can undermine some Raman measurements (Blacksberg et al., 2016; Misra et al., 2005). Typical pulsed laser

sources are Nd-YAG lasers (1064 nm; 532, 355, and 266 nm frequency doubling and wave mixing wavelengths) and tunable Nd:YLF pumped Ti-Sapphire lasers (e.g., 785 nm wavelength) for infrared excitation. Intensified charge-coupled devices (ICCD) are extensively used with pulsed lasers. The schematics of a typical remote Raman system (Fig. 1.6) usually has the laser head placed close to the telescope and the system is set up in coaxial geometry such that the optical axis of the laser beam is brought to the optical axis of the telescope by two laser specific dielectric mirrors. This geometry allows keeping the same optics alignment at different measurement distances.

Previous studies (Gasda et al., 2015; Misra et al., 2005) show that direct optical coupling between the telescope and the spectrometer is more efficient than fiber coupling or other methods. In the direct coupling configuration, the light collected by the telescope is focused into the spectrometer slit by means of a positive aspheric achromatic lens. The best results are obtained when the telescope focus, the coupling lens and the coupling distance between both are chosen to obtain an image of the laser spot on the slit that is smaller than the slit. Moreover, the converging angle of the final beam forming the slit image should not exceed the numerical aperture of the spectrometer. The addition of a laser beam expander in the laser path allows modifying the laser spot size at a distance and thus the irradiance of the laser on the samples. The beam expander can then be used to adjust for sample sensitivities and avoid damage, control the beam at large distances or focus the spot to add LIBS capabilities to the system (Sharma et al., 2006; Wiens and Maurice, 2016). It is useful to mount remote Raman systems on pan & tilt stages to provide pointing capabilities and make portable systems to use in the field. Finally, the camera and the laser are synchronized through a trigger signal. The camera is timed to the Rayleigh-Raman signal arrival and the measurement gate adjusted for the laser pulse length. For short laser pulses (<20 ns and 10-20 mJ per pulse) the Raman intensity is greater than ambient daylight, thus allows for daytime measurements. Modern remote Raman systems have been successfully used in daylight to measure geological samples in chambers simulating Mars and Venus conditions (Sharma et al., 2007; Sharma et al., 2011) and minerals or organics in open air and broad daylight at distances up to 430 m (Misra et al., 2012; see Chapter 5).

## 1.3 Purpose of the dissertation

The research I present in this dissertation is aimed to illustrate the potential of Raman spectroscopy in different areas of planetary geology. It is also intended to provide new science advancements, essential data for Raman spectra interpretations and new reporting of Raman instrumentation developments.

Raman spectra carry a wealth of information but are not simple to measure, and often low signal or fluorescence interference hinders the measurement. Therefore it is fundamental to develop techniques and apply technological advances to make Raman spectroscopy more versatile. Once a measurement is taken, its interpretation requires the use of the accumulated Raman database available in the literature since the late 1920s. This dissertation aims, in part, to add knowledge to the database in the field of planetary science and to develop and apply measurement techniques that could be used with great advantage by Raman users and scientists.

As stated in the motivation section, two upcoming planetary missions are going to be sent to Mars carrying Raman spectrometers in their payloads (Rull Perez and Maurice, 2016; Wiens and Maurice, 2016). NASA's mission will be equipped with remote Raman capabilities. Using remote and micro-Raman instrumentation this dissertation also aims to provide a baseline for what can be expected from measured samples of interest related to planetary science, such as geologic materials, organic compounds or water. Finally, with this dissertation I contribute in the development of better more suitable remote systems: sensitive and with longer measurement range; and more compact and with lower power consumption; with the intention of making space worthy instrumentation.

## 1.4 Organization of the dissertation

This chapter is the introduction. It presents Raman spectroscopy theory and applications to familiarize the reader with the Raman spectroscopy potential and possibilities for development. Important references on Raman spectroscopy are listed for the readers for further reading on the topic. It also describes the micro-Raman technique and the current state of remote time-resolved Raman instrumentation.

The contribution in the micro-Raman field is contained in Chapter 2, dedicated to micro-Raman mapping of mineral phases in a highly shocked ordinary chondrite. It is published as

Acosta-Maeda et al. (2013) in a peer-review journal. It shows the reader how a comprehensive Raman study of the phases, relationships, chemical composition and some crystal structures in a planetary geology sample could help identifying new chemical phases, always correlating with other technique for data validation. Preliminary data for this chapter were published in conference abstracts (Acosta et al., 2012a; Acosta et al., 2012b).

Chapters 3, 4 and 5 are contributions to the field of remote Raman and its application to planetary science. Chapter 3 presents measured values of the differential Raman cross sections of a large number of chemicals, including different nitrates, sulfates, carbonates, phosphates and organic liquids, for a remote Raman configuration. These cross sections could help in estimating detection limits of the chemicals at various target ranges for remote Raman systems. I initially took measurements to determine the differential cross section for the 801 $cm^{-1}$ vibrational mode of cyclohexane. Then I used the obtained result as a standard to determine the Raman cross sections of a set of selected samples by the relative intensities of their measured Raman peaks. The selected samples are of interest to planetary geology and astrobiology. The contents of this chapter have been accepted for publication in a peer-reviewed journal (Acosta-Maeda et al., 2016b).

Chapter 4 presents measured spectra of amino acids taken with a miniaturized remote Raman instrument (Gasda et al., 2015). This study demonstrates the detection of amino acids and nucleobases from a distance of 8 m using a portable, compact remote-Raman instrument. The remote Raman system is well suited for planetary exploration applications, with no requirement for sample preparation or collection, and rapid measurement times of astrobiology relevant samples. The chapter provides useful information in validating the concept that a remote Raman system would be helpful in detecting life in other planets. The results of this study were published as a conference abstract (Acosta-Maeda et al., 2014) and will take part of a future peer-reviewed publication, currently in preparation.

Chapter 5 shows good quality Raman spectra of various materials from a 430 meter distance. The data were collected using a pulsed remote Raman system with an 8” telescope during daytime, which shows the detection capabilities of a current state of the art remote Raman system developed at the University of Hawai‘i. The remote Raman spectra taken at that distance provide significant advancement for the unambiguous detection of compounds important for

planetary science, such as water and water ice, sulfur and various minerals. A summary of the results of this chapter has been published as a conference abstract (Acosta-Maeda et al., 2016c) and a more extended version has been submitted for publication in a peer review journal (Acosta-Maeda et al., 2016a).

Chapter 6, the conclusions, will put the findings of this dissertation into context and signal some future work.

# CHAPTER 2: MICRO-RAMAN MAPPING OF MINERAL PHASES IN THE STRONGLY SHOCKED TAIBAN ORDINARY CHONDRITE

Published in its present form as Acosta-Maeda, T.E., Scott, E.R.D., Sharma, S.K., and Misra, A.K. (2013) The pressures and temperatures of meteorite impact: Evidence from micro-Raman mapping of mineral phases in the strongly shocked Taiban ordinary chondrite. American Mineralogist, 98, 859-869.

## 2.1 Abstract

Taiban is a heavily shocked L6 chondrite showing opaque melt veins. Raman spectroscopy was used to characterize the high-pressure silicate assemblages in a thin section crossed by a shock-created 4 mm wide melt vein. Raman spectra using different excitation wavelengths allowed identification of mineral phases such as olivine, wadsleyite, ringwoodite, high-Ca clinopyroxene, majorite-pyrope, jadeite, maskelynite, and lingunite. Fe-depleted olivine in contact with the ringwoodite suggests chemical fractionation during a solid-state olivine-ringwoodite transformation. Raman imaging revealed a close correlation between the blue ringwoodite color and the peak observed at 877 $cm^{-1}$. This signal shows strong near-resonance Raman enhancement when measured with near-IR excitation lines (785 and 830 nm) close to the optical absorption bands of the ringwoodite. The blue color of the ringwoodite is likely caused by a small amount of iron in four-fold coordination inside the spinel structure, and that yields the observed spectral features in differently colored ringwoodite. Under the formation conditions of the studied silicate pocket, all enstatite transformed to a majorite-pyrope solid solution, whereas the high-Ca clinopyroxene likely remained unchanged. Maskelynite grains in the margins of the pocket often contain lingunite or are totally transformed to jadeite. Based on static high-pressure results, the mineral assemblages in the pocket suggest peak pressure in the 17–20 GPa range with maximum temperature (*T*max) in the range 1850–1900 K as the formation conditions for this Taiban chondrite during shock.

## 2.2 Introduction

High-pressure polymorphs of major minerals are commonly found in shocked meteorites. During the formation and later evolution of the Solar System (Raymond, 2010; Wetherill, 1980), asteroids repeatedly collided with each other and with larger bodies triggering shock waves. Meteorites that underwent such shock waves show different shock effects depending on the peak pressures and temperatures, and duration of the collision events (Stöffler et al., 1991).

Minerals commonly found in or near melt veins in highly shocked chondrites include ringwoodite, majorite, wadsleyite, magnesiowüstite, akimotoite, lingunite, silicate–perovskite, and maskelynite (Chen and El Goresy, 2000; Chen et al., 1996; Ferroir et al., 2008; Mori, 1994; Price et al., 1983 ; Sharp et al., 1997; Tomioka and Fujino, 1997; Xie et al., 2006). As the shock

front triggered by a collision spreads through the irregularities of the rock, melt veins and shocked pockets form depending on pressure and temperature conditions and the properties of the rock at each point. High-pressure phases form by solid-state transformations of the original minerals or fractional crystallization from the melt. Based on results from static high-pressure and shock recovery experiments, the observed crystallization assemblages can aid in constraining the conditions of melt vein crystallization (Sharp and De Carli, 2006). However, these methods present some difficulties. Shock recovery experiments probably produce lower temperatures and shorter shock durations than natural impacts. Similarly, equilibrium phase diagrams obtained from static high-pressure experiments fail to reproduce the large departures from equilibrium that mineral phases experience during shock. Furthermore, static experiments do not produce direct transformation from low-pressure phases without forming intermediate structures (e.g., olivine to ringwoodite without forming wadsleyite) (Sharp and De Carli, 2006; Stöffler et al., 1991; Xie and Sharp, 2007; Xie et al., 2006)

Ringwoodite $\gamma$-$(Fe,Mg)_2SiO_4$ is the high-pressure polymorph of olivine with spinel structure. It is found as a rare mineral in shocked meteorites and arguably in impact craters by transformation from olivine, and is considered to be the major constituent of the lower part of the mantle transition zone (Binns et al., 1969; Ringwood, 1975; Rull et al., 2007). Thus, the physical properties of the ringwoodite are key to understanding the behavior of that zone in the Earth's interior. The mineral has also been the subject of abundant research since its discovery by Binns et al. (1969) in the Tenham meteorite (e.g. Gupta and Goyal, 2011; Madon and Poirier, 1983; Mosenfelder et al., 2001; Price et al., 1982; Sinogeikin et al., 2003). Raman spectroscopy has been used extensively to assess the nature of the olivine polymorphs and other shock-induced phases (e.g. Chen et al., 2007a; Miyahara et al., 2008; Zhang et al., 2006). However, only a few studies have taken advantage of the potential for Raman spectroscopy to provide compositional and structural information on the shock-induced ringwoodite phases (e.g., Feng et al. 2011) .

Micro-Raman spectroscopy has been used successfully to provide unequivocal identification of minerals and glassy phases in meteorites and to obtain additional information on structural and compositional variations inside mineral grains (Cooney et al., 1999; Fries et al., 2011; Wang et al., 2001; Wang et al., 2004). In combination with a microscope and an automated X-Y-Z stage, Micro-Raman spectroscopy can resolve sample sizes as small as 1 μm

and place the data in its spatial context. Raman mapping, or Raman imaging, is a powerful technique that combines the mineralogical information included in the Raman spectra with spatial distribution, thus provides additional information on the petrography of the studied rocks and allows for constraints on the crystallization histories (Fries et al., 2011; Frosch et al., 2007; Miyahara et al., 2008; Steele et al., 2007).

### 2.3 Sample

Taiban is a very strongly shocked, shock stage S6 ordinary L6 chondrite found in De Baca County, New Mexico, in 1975 (Lange et al., 1980). It shows multiple veins of opaque shock melt produced by shearing during the shock event that extracted the meteorite from its parent body. The melt veins form a network of complex branches surrounding pockets of highly shock-altered, mosaicized (i.e., made into a mosaic), relict, or recrystallized silicates, and their high-pressure polymorphs, along with droplets of immiscible troilite and metallic inclusions. Outside the melt vein, olivine forms a mosaic only with diapletic plagioclase glass (maskelynite) interstitial to olivine and the different pyroxenes (Scott et al., 2004; Stöffler et al., 1991). The studied polished thin section UNM297 (Fig. 2.1) is intersected by a 4 mm wide melt vein in which the shock silicate pockets are dominated by blue and white ringwoodite crystals that range in size from 10 to 100 μm. As ringwoodite is assembled in clasts within the vein and the surrounding white matrix, the high-pressure phase did not crystallize from the impact melt (Scott et al., 2004). Minor amounts of host olivine and the intermediate phase β-$(Mg,Fe)_2SiO_4$ wadsleyite also appear associated with the ringwoodite. The white matrix is composed mainly of pyroxenes (high-Ca clinopyroxene and jadeite) and the high-pressure garnet polymorph of pyroxene, majorite. Plagioclase quenched to glass is conspicuous in the vicinity of the melt vein but was not found inside the lithic pockets or the melt areas; maskelynite grains have flow textures filling gaps between olivine and pyroxene. No lamellar intergrowth structures of ringwoodite and olivine were found so far in Taiban meteorite under optical microscope and SEM observations.

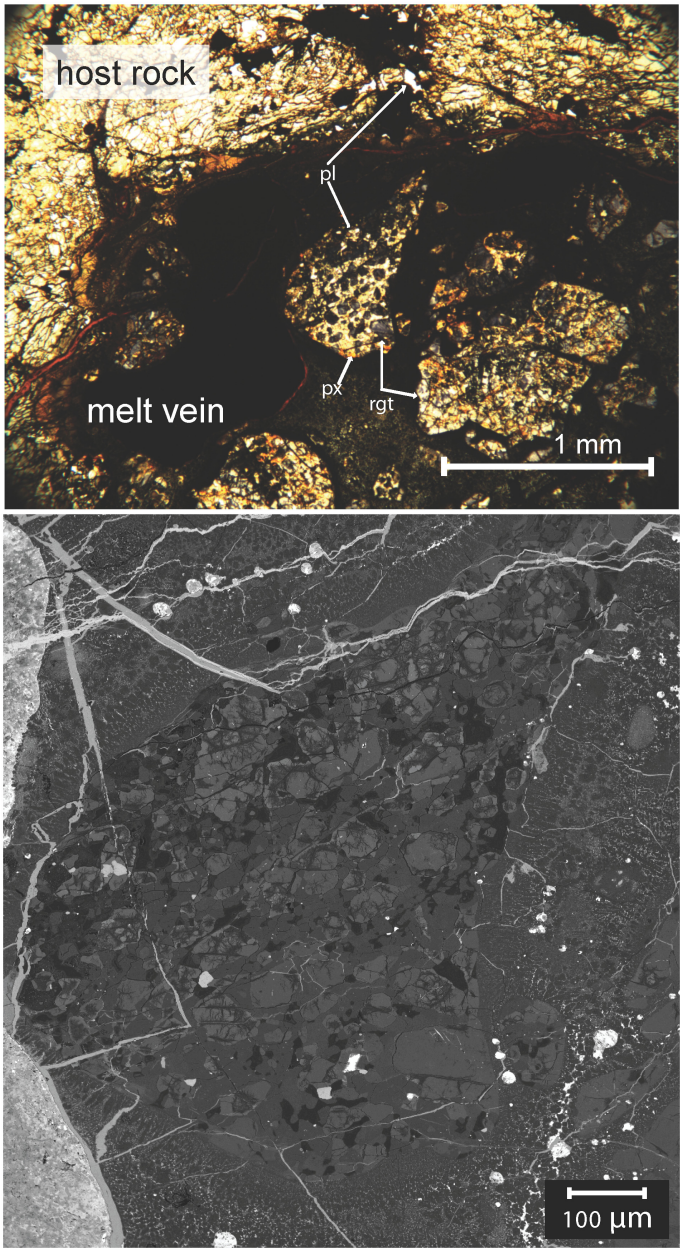


Figure 2.1: (a) Transmitted light photomicrograph of the black melt vein of the Taiban meteorite. Pockets inside the vein contain pyroxene (px) assemblages, blue and white ringwoodite grains (rgt), and relict plagioclase glass (pl). Ringwoodite tends to be clearer in color toward the mid-section of the vein, approximately in the bottom right corner of this image. Black areas contain metal-sulfides, iron oxides, and metal inclusions, among other submicrometer phases. The host rock is mainly composed of assemblages of olivine, enstatite, high-Ca pyroxene, and plagioclase totally transformed to maskelynite. (b) Backscattered electron image of the silicate pocket located in the center of the above image.

## 2.4 Methods

Raman spectroscopy with different excitation wavelengths was used in combination with optical images. Raman spectra were taken with three different instruments at the University of Hawai'i. Spectra with 785 nm excitation wavelength were taken with a Kaiser Optical Systems' micro-Raman system. The system is composed of a 785 nm Invictus diode laser, a Leica microscope with imaging capabilities, a Kaiser Holospec spectrometer, and an Andor CCD camera. A 100 μm optical fiber transmits the laser light to the microscope and the Raman signal to the spectrometer. The laser is focused and the signal is observed through a 100× objective mounted on the microscope in backscattering geometry; the laser spot size on the sample was 2 μm. The system has a spectral range of 150–3300 $cm^{-1}$. Typical acquisition time was 150 s and laser output power was limited to 10 mW, after making sure no sample damage was induced at that power. To look for resonance Raman effects and allow assessment of Raman peaks vs. fluorescence peaks, additional spectra were taken with a Renishaw inVia micro-Raman system coupled with a 830 nm Invictus diode laser, a 244 nm frequency doubled Ar ion Lexus laser, and a 514.5 nm Ar ion laser. The microscope and spectrometer are coupled through optical mirrors and all the optics can be set to accommodate different wavelengths. The 514.5 and 830 nm lasers were focused on the sample through a 100× objective that also acted as a signal collector; laser spot sizes were approximately 2 μm for both wavelengths. Because of high absorption in the UV range, a 40× UV objective was used for the 244 nm line, which focuses the beam down to 5 μm spot size. Laser powers were kept under 5 mW for 830 nm, 1 mW for 514.5 nm, and 0.2 mW for 244 nm to avoid laser-induced heating or sample photo-damage. Raman spectral ranges were 120–1600 $cm^{-1}$ for 830 nm, and from 300–4000 and 500–4000 $cm^{-1}$ for 514.5 and 244 nm, respectively.

Spectra with 532 nm excitation were collected using a WiTec Alpha300R confocal Raman microscope with a frequency doubled Nd-YAG laser (Coherent Compass) beam at 532 nm. The power of the 532 nm laser beam at the sample was 3 mW. All the spectra were acquired through a 100× objective with 300 s exposure time and a laser spot of around 2 μm. The Raman systems used for this study have a peak resolution of 6 $cm^{-1}$ for the 514, 785, and 830 nm Raman systems, and 10 and 12 $cm^{-1}$ for the UV 244 and 532 nm Raman systems, respectively (using the FWHM of the 1085 $cm^{-1}$ calcite line measured with the various Raman systems). The mineral

assemblages in the thin section of the Taiban meteorite were observed in transmitted, reflected, and cross-polarized light. Different areas were examined inside and outside the ~4 mm melt vein. The main focus of the study was a silicate pocket inside the melt vein, surrounded by quenched glass. Outside the melt vein silicates have milder shock effects with the conspicuous presence of maskelynite.

For detection of minor phases, line and area scans were performed with the aid of an X-Y-Z stage with submicrometer accuracy in addition to point Raman measurements for 244, 785, and 830 nm. The sample was scanned under the laser beam in 2D for a Raman chemical image. Typically, step distances were chosen to match the 2 μm laser spot size and exposure times were set to 150 s. Data obtained during mapping runs were examined to locate the minor phases and obtain typical spectra for each phase to generate the Raman images. Typical images cover an area of approximately 600 μm2 over 12 × 12 pixels and each phase was identified by its Raman signature peaks. Map intensity scales were generated by integrating the area or the peak height of each of the phases: the 856 $cm^{-1}$ peak for olivine; 1013 $cm^{-1}$ peak for high-Ca pyroxenes; 929 $cm^{-1}$ peak for majorite; 799 $cm^{-1}$ peak for ringwoodite; and 877 $cm^{-1}$ peak for blue ringwoodite. Background subtraction and cosmic ray removal software processing was applied for each acquisition. Additional processing was needed to remove the small contribution of the microscope slide substrate and epoxy resin to the Raman signal. This was necessary for mineral phases transparent to the laser light at each wavelength. Representative spectra from the substrate were obtained at the edges of the slide and then subtracted from each of the spectra. Spectra operations and curve fittings were performed with the Grams/AI 8.0 software package (Thermo-Fisher Scientific, Inc.).

After the Raman measurements, the thin section was coated with carbon and studied with an electron microprobe (JEOL JXA-8500F) equipped with 5 tunable wavelength-dispersive spectrometers at the University of Hawai'i. Mineral chemical analyses were performed with a beam energy of 15 keV, a beam current of 15 nA, and an electron beam diameter of typically 5 μm. A combination of natural and synthetic standards was used for the calibration. Oxygen was calculated by cation stoichiometry and included in the matrix correction. Typical detection limits were 0.010 wt% for Al*K*α, 0.012 wt% for P*K*α, 0.014 wt% for Na*K*α, 0.019 wt% for Ti*K*α, and

0.035 wt% for Mn*K*α. The matrix correction method was ZAF or Phi-Rho-Z calculations and the mass absorption coefficients data set was LINEMU.

## 2.5 Results and discussion

Raman spectra imaging and single point measurements were taken in and around the biggest ringwoodite crystal (Figure 2.2). Some additional spectra were recorded in other areas of the white matrix, other silicate pockets, and in several points in the mineral assemblages outside the melt vein.

### 2.5.1 Olivine, wadsleyite, and ringwoodite

Raman signature peaks of olivine are found at several points in and around the ringwoodite. The spectra of the grains within the ringwoodite and between grains show the characteristic peaks of olivine at 824 and 856 $cm^{-1}$, referred to as DB1 and DB2 bands, respectively (after Kuebler et al. 2006), in good agreement with the shifts found in forsterite (Chopelas, 1991a). This pair originates from the Si-$O_{nb}$ bond stretching in the $[SiO_4]^{4-}$ tetrahedral and have a mixed character of $\upsilon_1$ and $\upsilon_3$ modes (Lam et al., 1990). An additional olivine peak appears at 962 $cm^{-1}$ within the ringwoodite and in the olivine filling the 1 μm crack between the ringwoodite grains. Olivine and pyroxene-majorite assemblages or the melt vein are in direct contact with the ringwoodite around the rest of the perimeter. According to a Raman composition calibration of olivine developed by Kuebler et al. (2006), olivine intermingled with the ringwoodite inside the lithic pocket in the melt vein is Fo88, while olivine filling the 1 μm crack is Fo94. In the host rock, olivine is Fo78 (Fig. 2.3, Tables 2.1 and 2.2). The olivine inside the pocket is intermingled with the ringwoodite formed after shock and found in small grains showing dendritic textures or filling the 1 μm crack between ringwoodite grains (Figs. 2.2 and 2.4). The discrepancy in the calculated Fo content of the olivine located within the ringwoodite most likely results from the difference in sampling depth between the two techniques and the Raman spectra of that area showing a contribution of both olivine with dendritic shapes and ringwoodite, thus inducing a bigger error in the estimation of the Raman peak positions. Alternatively, the DB1 and DB2 have been shown to shift during high-velocity shock experiments with impact speeds over 5 km/s (Harriss and Burchell, 2016). The olivine in the host rock is predominantly fine-grained (however, crystals up to 100 μm are found in some areas) and

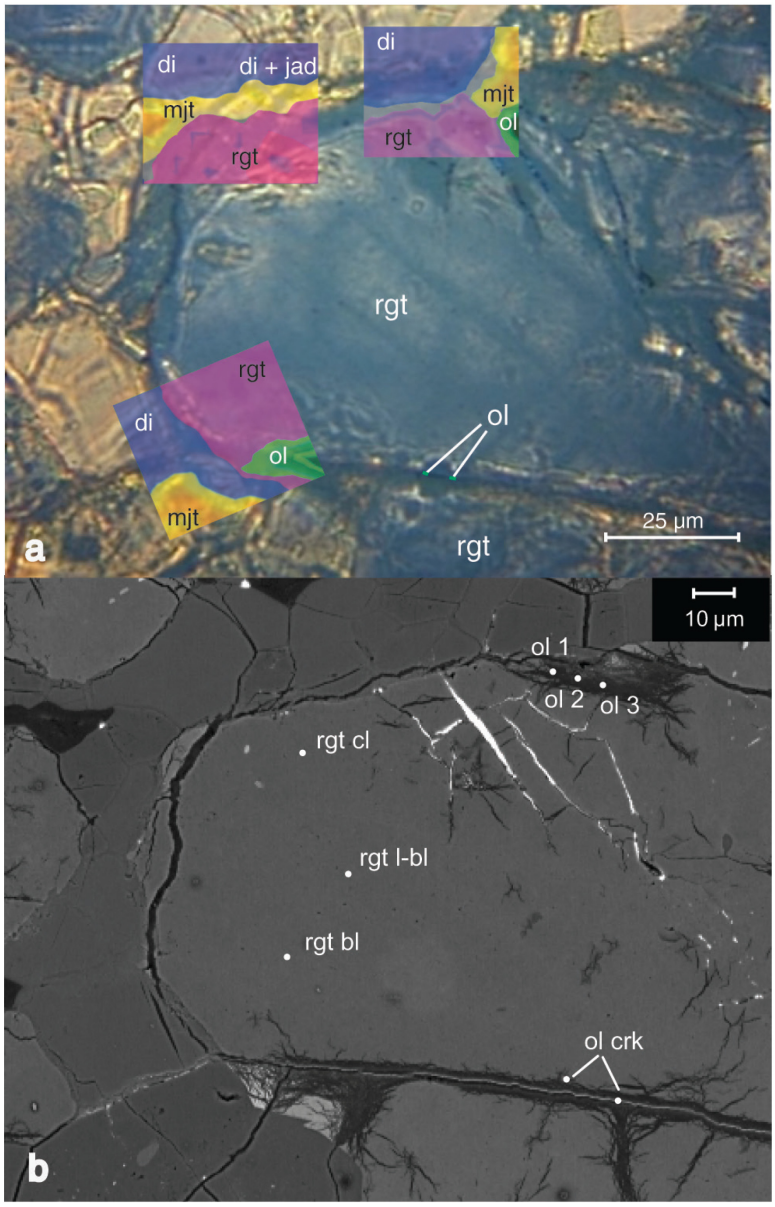


Figure 2.2: (a) Raman maps and phase distributions inferred from additional 2-D maps, 1-D lines, and single point measurements around the studied ringwoodite crystal. The ringwoodite is surrounded by pyroxenes and majorite assemblages. High-Ca pyroxene appears both alone and with jadeite in the Raman spectra of this area. Fe-depleted olivine is present in minor grains at the boundaries of the ringwoodite grain ($Fo_{88}$) and along the 1 µm crack separating the ringwoodite grains in the center and in the bottom of this image ($Fo_{94}$). (b) Backscattered electron image of the same area. Olivine appears darker than the ringwoodite and pyroxene crystals. White dots show EMPA measurement points. The clear circle in the ringwoodite is due to damage of the carbon coating by the electron beam.

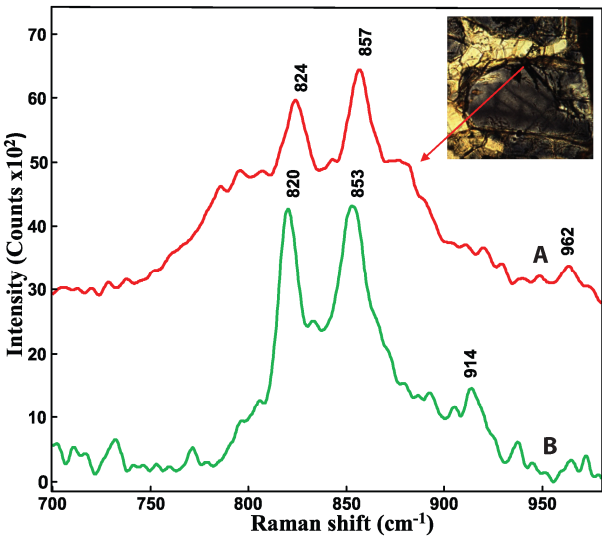


Figure 2.3: Olivine inside the pocket in the melt vein (A) and in the host rock (B) a few millimeters away from the melt vein in the same microscope slide. The olivine inside the pocket is intermingled with the ringwoodite formed after shock. The olivine in the host rock is fine grained and found among pyroxenes. Raman lines are shifted up inside the melt vein indicating a higher Fo content than the host olivine.

is also found in inclusions and among high-Ca and low-Ca pyroxenes, and maskelynite.

Spectra taken at the inner points of the crystal show Raman fingerprints of pure ringwoodite. The vibrations located at 301, 589, 799 (referred to as RA1), and 844 $cm^{-1}$ (referred to as RA2) correspond to ringwoodite, γ-$(Fe,Mg)_2SiO_4$. These vibrations have also been observed in natural ringwoodite lamellae in the Sixiangkou meteorite (Chen et al., 2007a), NWA 1662 (Taran et al., 2009), and in synthetic ringwoodite (Akaogi et al., 1984; Chopelas et al., 1994; Kleppe et al., 2002b; McMillan and Akaogi, 1987). The Raman mode at 844 $cm^{-1}$ corresponds to pure Si-O bond stretching, $A_{1g}$ symmetry. The signals found at 301, 589, and 799 $cm^{-1}$ are $T_{2g}$ modes, opposite oscillations of the two tetrahedral centers (Yu and Wentzcovitch, 2006). RA1 and RA2 probably

Table 2.1: Peak positions of DB1 and DB2 Raman spectra of olivine recorded in different lithologies of the Taiban meteorite.

| Olivine location | DB1 | DB2 | Fo(%) | Fo(%) |
|---|---|---|---|---|
| Ol in crack | 823.8 | 856.4 | 93.8 | 93.6 |
| Ol within | 823.4 | 856.8 | 87.6 | 92.1 |
| Ol host rock | 820.9 | 852.4 | 77.8 | 75.5 |

Note: Mg/(Mg+Fe) ratios are calculated both using the Raman calibration developed by Kuebler et al. (2006) and by EPMA. The Raman calculated values are within Fo±10%, the EPMA values are within Fo±5%.

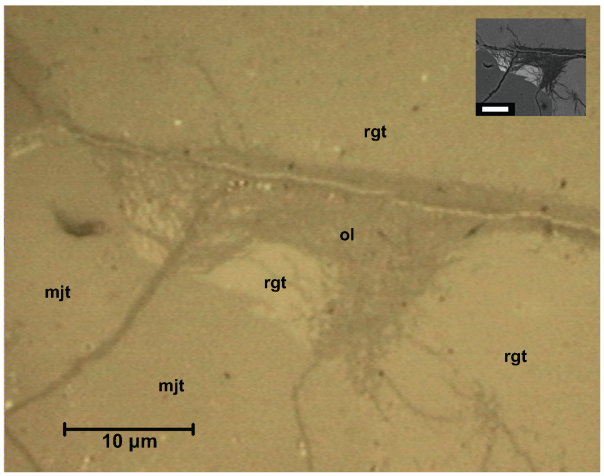


Figure 2.4: Olivine showing dendritic textures intermingled with the ringwoodite grain. Inset shows the same area in backscattered electrons image; scale bar is 10 µm.

have a mixed character of $\upsilon_1$ and $\upsilon_3$ modes, similar to that observed for the olivine doublet DB1 and DB2. Additional measurements taken with excitation wavelengths, 244, 514.5, and 830 nm confirm that the peak observed at 877 $cm^{-1}$ corresponds to the ringwoodite structure. The same peak was observed in other meteoritic and synthetic ringwoodite and researchers have proposed that it is caused by the presence of a defect-induced vibrational mode, by a inverse spinel structure in which the Mg and Fe ions are both in fourfold and sixfold coordination, or by the presence of glassy material (Kleppe et al., 2002a; Nagy et al., 2010a; Nagy et al., 2010b). The intensity of the 877 $cm^{-1}$ signal (Figs 2.5 and 2.6) presents a remarkably accurate spatial correlation with the color observed by optical microscopy and polarized light. The intensity is higher when the ringwoodite is deep blue, intermediate in clear blue areas, and absent when the ringwoodite is colorless. This applies to at least five different ringwoodite grains of different and variable colors observed with different instruments, ruling out crystal orientation being the cause of the 877 $cm^{-1}$ peak. The ringwoodite spectra also show twofold broadening of line widths in blue ringwoodite with a comparable 877 $cm^{-1}$ peak contribution with respect to the lines RA1 and RA2. White ringwoodite, with a negligible 877 $cm^{-1}$ contribution, shows a half width of 22 $cm^{-1}$ for the RA1 peak, whereas blue ringwoodite shows an increased half width to 54 $cm^{-1}$.

The ringwoodite spectrum shows additional bands at 495 $cm^{-1}$ and a strong band at 225 $cm^{-1}$ with a shoulder at 175 $cm^{-1}$. These bands (also observed by Sharp et al. (2009) and Taran et al. (2009) for blue ringwoodite) are not the result of fluorescence because they are observed at the same Raman shift with 532, 785, and 830 nm laser excitation wavelengths. As in the observations of Sharp et al. (2009) and Taran et al. (2009), these bands appear only for blue ringwoodite when excited with a 532 laser. They are observed, however, for both clear and blue ringwoodite when each is excited with near-IR wavelengths (785 and 830 nm), although the

Table 1.2: EPMA of minerals in the Taiban chondrite.

| | Maj | Cpx | Rgt l-bl | Rgt cl | Rgt bl | Rgt cl2 | Ol crk | Ol 1 | Ol 2 | Ol 3 | Ol host |
|---|---|---|---|---|---|---|---|---|---|---|---|
| | | | | | | **wt%** | | | | | |
| $SiO_2$ | 52.99 | 53.87 | 37.73 | 37.95 | 37.38 | 36.80 | 40.47 | 40.63 | 40.38 | 40.80 | 37.35 |
| $TiO_2$ | 0.17 | 0.46 | - | 0.02 | - | - | - | - | - | - | - |
| $Al_2O_3$ | 0.18 | 0.53 | - | 0.01 | - | 0.01 | 0.06 | 0.32 | 0.32 | 0.13 | 0.01 |
| $Cr_2O_3$ | 0.10 | 0.77 | - | 0.18 | - | 0.07 | 0.01 | 0.02 | 0.02 | 0.01 | 0.02 |
| FeO | 14.53 | 4.89 | 24.82 | 24.69 | 25.96 | 25.28 | 6.42 | 8.46 | 7.47 | 6.26 | 22.55 |
| MnO | 0.48 | 0.23 | 0.11 | 0.10 | 0.03 | 0.06 | 1.67 | 2.01 | 2.04 | 2.02 | 0.53 |
| MgO | 28.33 | 16.87 | 37.17 | 37.28 | 36.28 | 37.12 | 49.19 | 48.11 | 48.37 | 50.02 | 38.89 |
| CaO | 0.70 | 21.85 | 0.05 | 0.07 | 0.04 | 0.02 | 0.04 | 0.06 | 0.07 | 0.07 | 0.03 |
| NiO | - | 0.04 | - | - | 0.04 | - | 0.07 | 0.25 | 0.28 | 0.09 | 0.02 |
| $P_2O_5$ | 0.03 | 0.02 | 0.06 | 0.01 | 0.08 | 0.02 | 0.07 | 0.01 | 0.01 | 0.02 | 0.03 |
| $Na_2O$ | 0.01 | 0.48 | 0.01 | - | 0.01 | 0.01 | - | - | - | - | 0.01 |
| Total | 97.53 | 100.02 | 99.96 | 100.32 | 99.85 | 99.42 | 97.98 | 99.88 | 98.97 | 99.42 | 99.44 |
| $Fo_{\%}$ | | | 72.75 | 72.91 | 71.36 | 72.35 | 93.17 | 91.02 | 92.02 | 93.44 | 75.46 |
| | | | | | | Calculated cations per formula unit | | | | | |
| Si | 3.9180 | 1.9749 | 0.9934 | 0.9949 | 0.9911 | 0.9793 | 1.0030 | 0.9992 | 0.9985 | 0.9979 | 0.9820 |
| Ti | 0.0097 | 0.0126 | - | 0.0004 | - | - | - | - | - | - | - |
| Al | 0.0154 | 0.0229 | - | 0.0003 | - | 0.0003 | 0.0016 | 0.0092 | 0.0093 | 0.0039 | 0.0002 |
| Cr | 0.0059 | 0.0223 | - | 0.0037 | - | 0.0015 | 0.0002 | 0.0003 | 0.0003 | 0.0001 | 0.0005 |
| Fe | 0.8986 | 0.1500 | 0.5466 | 0.5414 | 0.5756 | 0.5627 | 0.1331 | 0.1741 | 0.1546 | 0.1280 | 0.4958 |
| Mn | 0.0303 | 0.0072 | 0.0025 | 0.0022 | 0.0007 | 0.0014 | 0.0350 | 0.0419 | 0.0428 | 0.0419 | 0.0117 |
| Mg | 3.1231 | 0.9218 | 1.4591 | 1.4572 | 1.4340 | 1.4725 | 1.8172 | 1.7639 | 1.7830 | 1.8239 | 1.5244 |
| Ca | 0.0552 | 0.8584 | 0.0013 | 0.0020 | 0.0013 | 0.0007 | 0.0010 | 0.0016 | 0.0019 | 0.0018 | 0.0008 |
| Ni | - | 0.0012 | - | - | 0.0008 | - | 0.0015 | 0.0050 | 0.0056 | 0.0018 | 0.0004 |
| P | 0.0016 | 0.0006 | 0.0014 | 0.0002 | 0.0019 | 0.0004 | 0.0014 | 0.0001 | 0.0003 | 0.0004 | 0.0006 |
| Na | 0.0019 | 0.0344 | 0.0003 | - | 0.0008 | 0.0006 | - | - | - | - | 0.0008 |
| O | 12 | 6 | 4 | 4 | 4 | 4 | 4 | 4 | 4 | 4 | 4 |

Notes: Mjt = majorite; Cpx = high-Ca pyroxene; Rgt-bl = blue ringwoodite, Rgt cl = colorless ringwoodite, Rgt bl = blue ringwoodite, Rgt cl2 = clear ringwoodite in different crystal. Ol crk = olivine in the crack of the studied ringwoodite; Ol 1, Ol 2, Ol 3 = three measurements of olivine within the studied ringwoodite crystal; Ol host: olivine in the host rock. $Fo_{\%}$ = $[Mg/(Fe+Mg)] \times 100$.

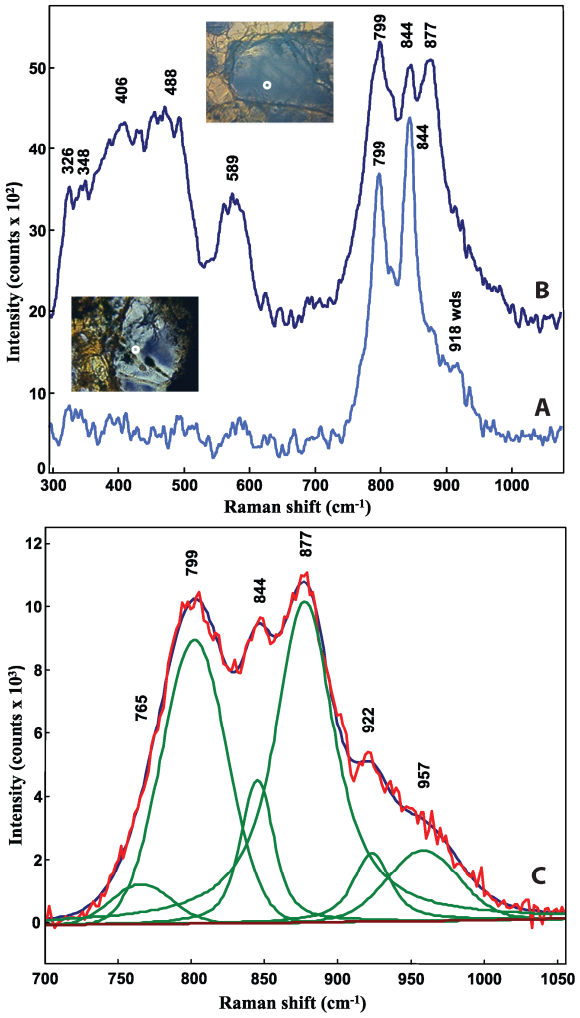


Figure 2.5: Raman spectra of (A) colorless and (B) deep-blue ringwoodite. The intensity of the 877 cm⁻¹ peak is enhanced in the blue ringwoodite due to the resonance Raman Effect with excitation at 785 nm. Several new bands also appear in the low-frequency region for deep-blue ringwoodite. 785 nm laser excitation, 10 mW power output, 150 s acquisition time. (C) Curve-fitting result for the spectrum of deep-blue ringwoodite with Lorentz-Gauss curve shapes. 830 nm laser excitation, 5 mW power output, 300 s acquisition time.

bands are less intense in the clear samples. These bands probably correspond to translational lattice modes in the ringwoodite structure because the positions are close to those measured for lattice modes of forsterite (Iishi, 1978). Raman and IR measurements also show that it is anhydrous ringwoodite, because no O-H modes have been detected under 244 or 514.5 nm excitation wavelengths or in infrared absorption spectra of both blue and clear samples. Minor amounts of wadsleyite are inferred from weak Raman peaks at 723 and 919 $cm^{-1}$, observable under 514.5 nm excitation (Chopelas, 1991b; McMillan and Akaogi, 1987). Observations from other meteorites show two different mechanisms for the transformation from olivine to its high-pressure polymorphs. These are incoherent nucleation on olivine grain boundaries or coherent intracrystalline nucleation of ringwoodite (Chen et al., 2006; Kerschhofer et al., 1998; 2000; 1996; Kubo et al., 2004; Ohtani et al., 2004; Putnis and Price, 1979). More recent meteorite observations (Feng et al., 2011; Miyahara et al., 2008) suggest fractional crystallization of wadsleyite and ringwoodite from a melt of olivine composition. Ringwoodite in the Taiban

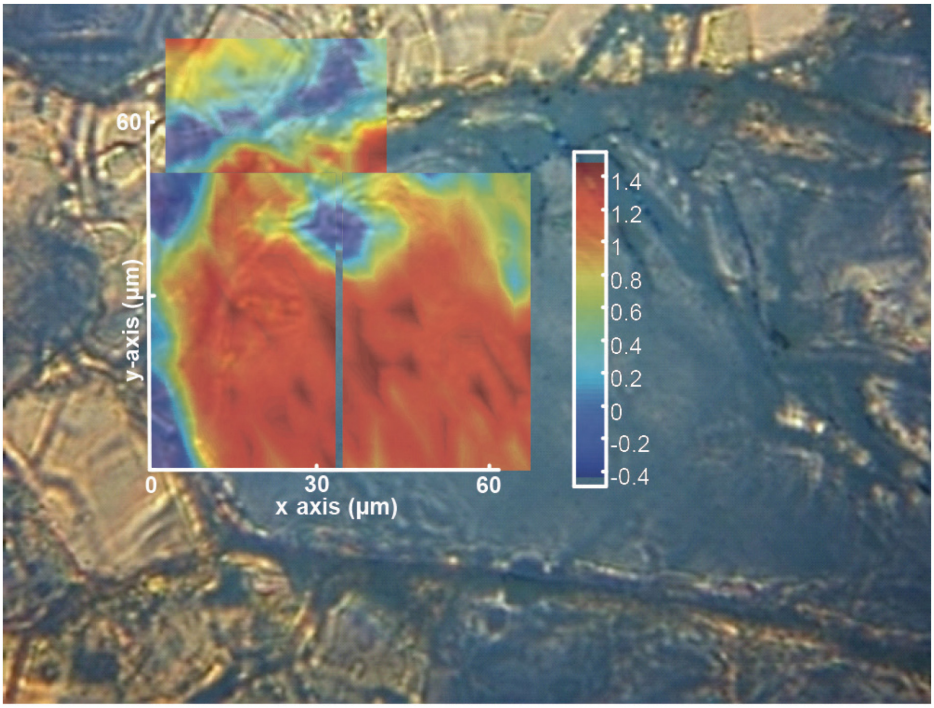


Figure 2.6: Composition of Raman images showing the intensity of the 877 $cm^{-1}$ peak in the ringwoodite grain. The peak is more intense in the red areas, showing the close correlation between the intensity of the peak and the blue ringwoodite color. The arbitrary color scale shows the integrated area of the peak between 860 and 900 $cm^{-1}$.

meteorite contains minor amounts of wadsleyite and olivine that is depleted in Fe (to different extents) with respect to the host olivine (Fo78–Fo94, Tables 2.1 and 2.2) in the vicinity of the ringwoodite grains. Thus, our results suggest that some chemical fractionation took place. The size, shape, and assemblages of the ringwoodite clasts in the pyroxene white matrix entrained in the melt vein, and the absence of wadsleyite crystals, suggest a solid-state transformation. Reflected light microphotography of the relict Fe-depleted olivine entrained in the bigger ringwoodite crystal shows darker olivine surrounded by ringwoodite resulting from the difference in light reflection coefficients between the two fractionated polymorphs (Fig. 2.4). The dendritic textures of the olivine core are similar to those reported by Xie et al. (2012) in olivine cores inside ringwoodite rims in GRV022321 and support the idea of a solid-state transformation with diffusion controlled growth between olivine and ringwoodite.

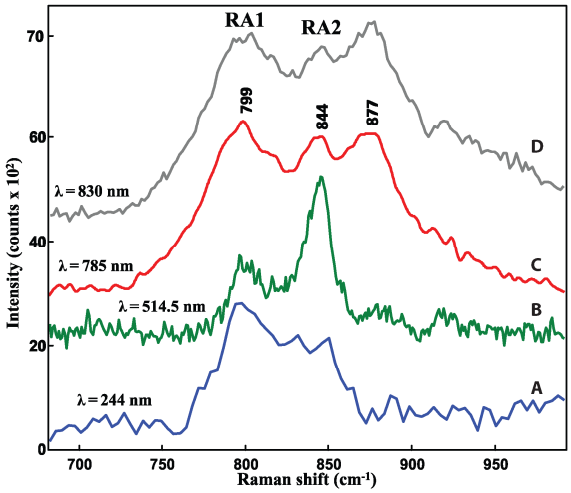


Figure 2.7: Variation in the relative intensity of the peaks RA1, RA2, and 877 $cm^{-1}$ in blue ringwoodite far from grain boundaries with various laser excitation wavelengths due to resonance Raman Effect. Excitation wavelengths, laser power, and acquisition times are (A) 244 nm, 0.5 mW and 1800 s; (B) 514.5 nm, 1 mW, and 600 s; (C) 785 nm, 10 mW, and 150 s; and (D) 830 nm, 5 mW, and 300 s, respectively.

Ideally, the approximate composition of ringwoodite can be inferred from the Raman peaks (Feng et al., 2011). The main peaks measured in the bulk of the ringwoodite grain are two major vibrations located at 798.8 and 843.2 $cm^{-1}$. Near the boundaries of the grain, the peaks are shifted to 797.5 and 843.5 $cm^{-1}$ near the majorite, and to 798.7 and 844.3 $cm^{-1}$ near the crack filed with olivine. This suggests slight differences in Fe and Mg ion content. Pure anhydrous γ-$MgSiO_4$ forms clear colorless crystals with vibrations at 796 (RA1) and 835 $cm^{-1}$ (RA2) (Chopelas et al., 1994) whereas hydrous γ-$(Mg_{0.89}Fe_{0.11})SiO_4$ ~1.6 wt% $H_2O$ is blue and the RA2 peak is shifted toward higher frequencies, 841 $cm^{-1}$. However, the position of the RA2 peak is not dependent on ringwoodite Fe-Mg contents, despite ranging from 835 to 849 $cm^{-1}$ (Feng et al., 2011). The ringwoodite studied in the Taiban meteorite would be equivalent to 72–78% Fo according to the Raman calibration developed by Feng et al. (2011), however that calibration is not reliable near pure Fo values and is not consistent with earlier measurements (Chopelas et al., 1994; McMillan and Akaogi, 1987). Nevertheless, the Raman calculated values in our study fall within ±6% Fo when compared to the EPMA results (Table 2.2). The Raman pattern observed in Taiban is close to those of the ringwoodite γ-$(Mg_{0.8},Fe_{0.2})_2SiO_4$ in the Tenham meteorite, 799 and 845 $cm^{-1}$ (Sato and Nakamura, 2010), and some of the ringwoodite in the lamellae of the Sixiangkou meteorite (22–24 wt% FeO), 799 and 844 $cm^{-1}$ (Chen et al., 2006). A possible explanation for this small shift found in the natural ringwoodite in these meteorites could be the presence of residual stress from the shock that triggered the transformation or the following relaxation. Sazonova et al. (2006) measured shifts of the RA1 peak up to 814 $cm^{-1}$ (814, 843; and 812, 846, in two different spectra) in ringwoodite containing Al up to 9 wt%, Ti up to 0.2 wt%, and K up to 1 wt% synthesized in a shock experiment from biotite. Thus, the presence of

some ions dissolved in the ringwoodite, namely Al, Ti or K, could also affect the position of the RA1 Raman line of ringwoodite. EPMA results show that the position changes can also be caused by slight variations in Ti, Cr, Mn, and P content in different points in the ringwoodite.

The cause of the blue ringwoodite color has been discussed in the past but it still remains mostly unknown. Lingemann and Stöffler (1998) and Price et al. (1979) observed glassy material around ringwoodite crystals in blue colored aggregates. However, this glassy material was not present in the colorless ringwoodite in the Sixiangkou meteorite (Chen et al., 1996). Iron has been ruled out as the cause of the blue color because of the absence of correlation between the ringwoodite color and the iron content (Coleman, 1977; Lingemann and Stöffler, 1998; Taran et al., 2009). Lingemann and Stöffler (1998) proposed that the blue color is caused by the light-scattering effect produced by the glassy material, and Nagy et al. (2011) suggested that the color results from scattering in grain boundaries in submicrometer grains. However, Taran et al. (2009) performed transmission electron microscopy on two foils from a colorless to dark blue ringwoodite grain but found no glassy phase in the colored areas. The color of the ringwoodite in the Taiban meteorite varies gradually within the mineral grains. Colorless areas coexist with blue to dark blue zones forming bubbly or filament patterns inside otherwise completely homogeneous mineral grains. In this study I found a relation between the Raman spectra and the color of the ringwoodite (Fig. 2.6). I assume the 877 $cm^{-1}$ peak has remained mostly unnoticed in previous Raman measurements (with the exception of Kleppe et al. 2002a and Nagy et al. 2010a, 2010b) because of the strong dependence of the Raman signal on the excitation wavelength. The 877 $cm^{-1}$ peak is not observable with 244 nm laser excitation (Figure 2.7). The peak is weak with respect to RA1 and RA2 with the widely used Ar 514.5 nm laser line and is comparable in intensity when excited with 785 or 830 nm laser wavelengths. I attribute this intensity dependence to near-resonance Raman enhancement in the blue ringwoodite. Absorption spectra from blue and dark blue natural ringwoodite from NWA 1662 and NWA 463 meteorites show a strong absorption line centered at 793 nm (Taran et al., 2009). Synthetic blue ringwoodite has similar absorption bands because of its iron content (Keppler and Smyth, 2005). In natural samples, the absorption is stronger in darker colored grains and weaker in colorless ringwoodite. This absorption band remarkably follows the same color correlation as observed in the 877 $cm^{-1}$ Raman peak and explains why the enhancement is only observed in colored ringwoodite. The color correlation of the absorption spectra and the Raman spectra suggest

that the cause of the color lies in the crystal structure of the ringwoodite. The absorption line was assigned by Keppler and Smith (2005) and Taran et al. (2009) to the electronic spin allowed $^5T_{2g} \rightarrow {}^5E_g$ transition of $^{VI}Fe^{2+}$ split by the trigonal distortion or Jahn-Teller effect. Similar Raman enhancements have been observed for iron containing oxides and oxyhydroxides, for which near resonance Raman occurs with 636 nm excitation due to an absorption band located near 640 nm; this band is a result of the $^6A_1(^6S) \rightarrow {}^4T^2(^4G)$ ligand field transitions of octahedrally coordinated $Fe^{3+}$ (Nieuwoudt et al., 2011; Sherman and Waite, 1985). Resonance Raman has also been confirmed in several spinel-structure oxides (Kashyap et al., 2009; Koshizuka et al., 1975; Lutz et al., 1991). Furthermore, the presence of unassigned peaks in Raman spectra from spinels attributed to disorder is not uncommon. The appearance of a new band in the non-silicate spinel $MgAl_2O_4$, after heating induced disorder, has been described as a contribution to the Raman spectrum from cation disorder in the form of Al-ion redistribution from octahedral to tetrahedral sites inside the spinel structure (Cynn et al., 1993; 1992). Thus, the peak observed at 877 $cm^{-1}$ is probably due to cation redistribution inside the spinel structure.

Taran et al. (2009) suggested an inverse spinel structure for the clear varieties of ringwoodite, based on the apparent different natures of the absorption spectra of blue and colorless varieties. In the inverse spinel, all $Fe^{2+}$ ions and probably part of the $Mg^{2+}$ are found in tetrahedral sites of the cubic close-packed structure, and $Si^{4+}$ cations would be displaced to the octahedral sites. However, the observed Raman shifts of RA1 and RA2 do not significantly differ between colorless and blue ringwoodite, suggesting that most of the $Si^{4+}$ is in fourfold coordination. This is consistent with nuclear magnetic resonance (Stebbins et al., 2009) and X-ray diffraction observations (Hazen et al., 1993). On the other hand, the observed increase in the linewidths of RA1 and RA2 indicate some degree of structural disorder in blue ringwoodite. Therefore, our data are consistent with the explanation that the gradation in color of the ringwoodite results from a spinel structure ranging from normal to marginally inverse. Assuming such cation disorder and that the band at 844 $cm^{-1}$ comes from Si-O bonds stretching in tetrahedral sites (Yu and Wentzcovitch, 2006), I tentatively assign the 877 $cm^{-1}$ Raman band to symmetric Fe-O stretching of a small amount of iron in fourfold coordination. Because of the resonance Raman enhancement effect, I believe that it is possible to detect low trace amounts of $Fe^{2+}$ in tetrahedral sites. In the same structure, no Raman signal would be expected from $Mg^{2+}$ ions in four- or sixfold coordination because of the highly ionic nature of the Mg-O bonding. This position is relatively close to the Raman

shifts of 830–832 $cm^{-1}$ reported for $FeO_4$ tetrahedra in $K_2[FeO_4]$ by Gonzalez-Vilchez and Griffith (1972). The difference of approximately 45 $cm^{-1}$ with respect to the $\upsilon_1(A_1)$ band at 830 $cm^{-1}$ could result from contributions of the following: the coupling between $SiO_4$ and $^{IV}FeO_4$ tetrahedra; induced distortion by the $SiO_6$ octahedra; or a shorter Fe-O bonding length, consistent with the high-pressure nature of the phase. Small bond distance differences can yield large Raman shifts, e.g., in the transition between olivine and ringwoodite the increase of the Si-O distances of 0.02 ± 0.0005 Å (Hazen et al., 1993) induces a Raman shift of 10–25 $cm^{-1}$ between the main peaks in olivine and ringwoodite. If the 877 $cm^{-1}$ Raman band is produced indeed by Fe-O stretching, one would expect also to observe Fe-O bending modes and $SiO_6$ octahedral symmetrical stretching. The $\upsilon_2$ and $\upsilon_4$ modes of the $FeO_4$ tetrahedral are reported to be in the region of 300–400 $cm^{-1}$ (Gonzalez-Vilchez and Griffith, 1972) and possibly could be the unassigned, enhanced bands observed in that region (Fig. 2.5). The spectra of the $SiO_6$ octahedra should resemble that of stishovite with two intense modes, $A_{1g}$ at 753 $cm^{-1}$ and $B_{1g}$ at 231 $cm^{-1}$ (Hemley et al., 1986). The band corresponding to the $A_{1g}$ mode may be a shoulder of the RA1 ringwoodite band at 799 $cm^{-1}$ (e.g., 765 $cm^{-1}$, Fig. 2.5). Similarly, the band assigned to the B mode could possibly contribute to the broad set of bands centered at 225 $cm^{-1}$. The near-IR Raman enhancements of these bands (~231, 300–400, ~753, and 877 $cm^{-1}$) support these tentative assignments.

### 2.5.2 Pyroxenes and majorite

White grains show pyroxene Raman fingerprints (Fig. 2.8). The high-Ca clinopyroxene (augite/diopside, *C*2/*c* monoclinic pyroxene) shows two intense peaks, the first one at 1013 $cm^{-1}$ corresponding to the Si-Onb bond stretching in the $[SiO_3]^{2-}$ unit of the pyroxene chain, and the second peak at 667 $cm^{-1}$ corresponding to the bridging oxygen stretch in the Si-Obr-Si bond of the $[Si_2O_6]^{4-}$ unit. Three smaller peaks are present in the range 300–400 $cm^{-1}$, 327, 369, and 395 $cm^{-1}$ created by the displacements of cations from their equilibrium lattice positions or by O-Si-O bending modes (Huang et al., 2000; Wang et al., 2001; Yang et al., 2009). A small amount of jadeite is also present in the white matrix. Jadeite has the ideal formula $NaAlSi_2O_6$ and shows three characteristic signals at 698, 377, and 204 $cm^{-1}$. Similar to the high-Ca pyroxene, jadeite is a *C*2/*c* monoclinic pyroxene and the 698 $cm^{-1}$ band originates from Si-Obr-Si vibrations within the silicate chains, and 377 and 304 $cm^{-1}$ are likely lattice modes involving cation-O interactions or O-Si-O bending modes. Jadeite bands also appear at 988, 1035 (Si-O stretching vibrations), 756 $cm^{-1}$ and smaller bands appear in the range 200–600 $cm^{-1}$ showing, respectively, cation vibrations and O-Si-O

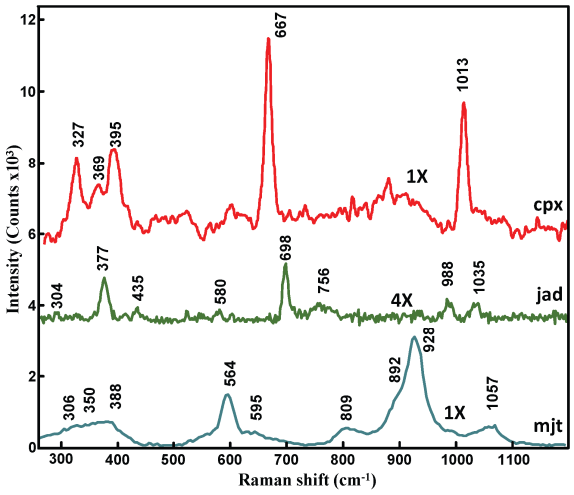


Figure 2.8: Raman spectra of pyroxenes and majorite (mjt) in the white matrix of the lithic pocket. Pyroxenes are high-Ca pyroxene (cpx) and jadeite (jad). High-Ca pyroxene: 785 nm laser; 10 mW power output; 150 s acquisition time. Jadeite: 830 nm laser; 5 mW power output; 150 s acquisition time. Majorite: 532 laser; 3 mW power output; 300 s acquisition time.

bending modes of $SiO_4$ tetrahedra (Huang et al., 2000; Wang et al., 2001; Yang et al., 2009). Along with the pyroxene crystals, majorite assemblages are present in the white matrix. The most intense modes of majorite are found at 597 and 929 $cm^{-1}$ (Rauch et al., 1996). Majorite is the cubic garnet polymorph of pyroxene. It has previously been found in the Coorara, Catherwood, Pampa del Infierno, Tenham, Sixiangkou, and Peace River chondritic meteorites (Coleman, 1977; Smith and Mason, 1970). Majorite forms in these meteorites from low-Ca pyroxenes (Chen and Xie, 2008; Coleman, 1977; Mao et al., 1982; Smith and Mason, 1970). Ca-rich majorite has been observed in the Shergotty and Yamato 75100 meteorites transformed from the host high-Ca pyroxene (Malavergne et al., 2001; Tomioka and Kimura, 2003). The peak positions of majorite in the Taiban meteorite are in good agreement with the values provided by Rauch et al. (1996) for pure $MgSiO_3$. The peak at 929 $cm^{-1}$ is probably the $A_{1g}$ mode from the symmetrical stretch of the $SiO_4$ group; and the 597 $cm^{-1}$ has been assigned to the $A_{1g}$ mode of the O-Si-O bending in the $SiO_4$ tetrahedral. However, there is a significant line width increase in several of the measured crystals, possibly the result of some deformational stress in the crystals or a small contribution of pyrope in solid solution with the majorite (Hofmeister et al., 2004; Manghnani et al., 1998; McMillan et al., 1989). Jadeite Raman signals often appear in combination with diopside or majorite peaks, suggesting that jadeite mineral grains are smaller than the laser spot size in the mapped areas.

The pyroxene-majorite assemblages completely surround the ringwoodite crystals in the silicate pocket. These assemblages are mainly composed of high-Ca pyroxene, majorite, and jadeite. The presence of high-Ca pyroxene and majorite suggests that under the pressure and temperature conditions that the silicate pocket experienced, all the low-Ca pyroxene

metamorphosed into the its high-pressure phase majorite. The calcium pyroxene, however, reversed a high-pressure transformation after the shock or remained unchanged. Similar assemblages were found in the Sixiangkou meteorite by Zhang et al., (2006) and they suggested that the preserved high-Ca pyroxene could be attributed to the higher temperature needed for the high-Ca pyroxene to transform to Ca-rich majorite, but at a very sluggish phase transformation rate. They suggested that the sluggish rate might have been caused by the large radius of the cation $Ca^{2+}$ (0.99 Å) in the crystal structure, its coordination is more difficult to modify under high pressures than that of $Mg^{2+}$ (0.66 Å) and $Fe^{2+}$ (0.74 Å) in the low-Ca pyroxenes (Zhang et al., 2006). Jadeite probably formed from felsic plagioclase feldspar under the pressures and temperatures experienced during shock. Under pressure above the maskelynite stability field, plagioclase dissociates into jadeite and $SiO_2$ (Liu, 1978). Jadeite has been found in other chondrites with similar compositions as the plagioclase glass in the vicinity of melt veins (Ohtani et al., 2004). In the Taiban meteorite pocket, the micrometer-sized jadeite crystals suggest that plagioclase melted and dissociated into jadeite and $SiO_2$. The maskelynite in the host rock shows increasing deformation and flow textures toward the melt vein, consistent with total melting inside, where jadeite formed. The absence of the Raman signature peaks of $SiO_2$ polymorphs can be explained if jadeite crystallized from amorphous plagioclase while the crystallization of stishovite was significantly delayed (Kubo et al., 2010), leaving the $SiO_2$ in form of glass.

### 2.5.3 Maskelynite and lingunite

Larger amounts of plagioclase glass are found in the host rock areas compared with the relict plagioclase glass located in the margins of the silicate pocket, near the host rock. Plagioclase glass forms clear isotropic grains (Stöffler et al. 1991, their Fig. 12). The spectra of both silicate glasses (Fig. 2.9) are dominated by a broad set of bands characteristic of plagioclase feldspar glass, centered around 480 $cm^{-1}$. This is in good agreement with the spectra reported by Sharma et al. (1983) for synthetic glass of anorthite composition and with earlier measurements of maskelynite from natural samples (Chen and El Goresy, 2000; Fritz et al., 2005). This band has been attributed to the motion of the oxygen atom along a line bisecting the T-O-T angle (where T = Si or Al) and is characteristic of the feldspar structure, which contains four-membered rings of $TO_4$ tetrahedra (Sharma et al., 1983). The weak shoulder located around 570 $cm^{-1}$ has been assigned to the three member rings of $TO_4$ tetrahedra in the framework silicate glasses (Galeener and Geissberger, 1983; Sharma et al., 1997). Its low intensity is consistent with the observations for highly shocked plagioclase

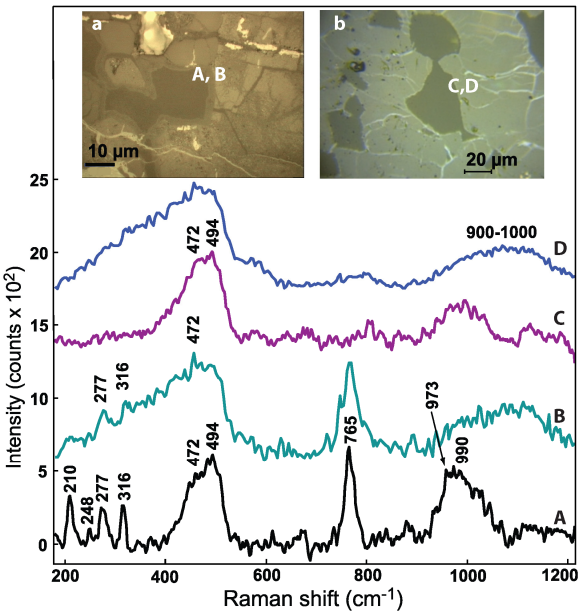


Figure 2.9: Raman of plagioclase glass in the studied lithic pocket (a) and in the host rock (b) of the Taiban meteorite. Inside the melt vein (a), lingunite peaks appear along with the plagioclase glass Raman spectrum. Plots (A) and (B) show the spectrum of maskelynite inside the pocket (a); and (C) and (D) show the spectrum of maskelynite in the host rock (b). (A) 830 nm laser, 3 mW power output, 400 s acquisition time. (B) 532 nm laser, 3 mW power output, 300 s acquisition time. (C) 830 nm laser, 5 mW power output, 150 s acquisition time. (D) 532 nm laser, 3 mW power output, 300 s acquisition time. With 785 nm laser excitation spectrum was obscured by strong luminescence backgroundare (A) 244 nm, 0.5 mW and 1800 s; (B) 514.5 nm, 1 mW, and 600 s; (C) 785 nm, 10 mW, and 150 s; and (D) 830 nm, 5 mW, and 300 s, respectively.

(Fritz et al., 2005). The spectra of plagioclase glass in the high-frequency range shows slightly different patterns when measured with different wavelengths. The Si-O stretch bands at 900–1100 $cm^{-1}$ appear in the spectra recorded with 532 nm laser excitation. The spectra of plagioclase glass in the high-frequency range shows slightly different patterns when measured with different wavelengths. The Si-O stretch bands at 900–1100 $cm^{-1}$ appear in the spectra recorded with 532 nm laser excitation. With 830 nm laser excitation a strong broad band appears at 990 $cm^{-1}$ (904 nm). This band is probably the result of fluorescence caused by rare earth elements, likely Nd, whose strongest fluorescence band is also found around 907 nm. The spectra of plagioclase glass in the high-frequency range shows slightly different patterns when measured with different wavelengths. The Si-O stretch bands at 900-1100 $cm^{-1}$ appear in the spectra recorded with 532 nm laser excitation. With 830 nm laser excitation a strong broad band appears at 990 $cm^{-1}$ (904 nm). This band is probably the result of fluorescence caused by rare earth elements, likely Nd, whose strongest fluorescence band is also found around 907 nm. Lingunite, $(Na,Ca)AlSi_3O_8$, is one of the high-pressure polymorphs of plagioclase. It possesses hollandite structure and was first observed by Gillet et al. (2000) in the Sixiangkou chondrite. Lingunite Raman peaks appear along with the glass

spectrum in the maskelynite grains inside the melt vein (Fig 2.9), at 210, 277, and 765 $cm^{-1}$. These peaks are characteristic of the hollandite structure: the signal at 765 $cm^{-1}$ corresponds to $SiO_6$ octahedral symmetrical stretching; and the peaks at 210 and 277 $cm^{-1}$ correspond to the splitting of the $B_{1g}$ mode. A band resulting from the splitting of the $B_{2g}$ mode appears at 973 $cm^{-1}$ (Gillet et al., 2000; Liu et al., 2009). The 973 $cm^{-1}$ band in the measured plagioclase glass inside the silicate pocket (Fig. 2.9) superimposes on the fluorescence feature around 990 $cm^{-1}$. It has been suggested that lingunite is formed by a solid-state transformation from plagioclase (Tomioka et al., 2000) or by crystallization from a melt (Gillet et al., 2000). Similarly, it has been suggested that plagioclase glass is a quenched melt as opposed to diaplectic glass, maskelynite (Chen and El Goresy, 2000). The plagioclase glass grains in the studied thin slide of the Taiban meteorite present signs of ductile deformation but no evidence of extensive melting, either inside the melt vein or in the host rock. Furthermore, Raman bands of recrystallized plagioclase were not observed in any of the measured grains. If the plagioclase had melted we would expect some degree of recrystallization unless the quenching rate was unrealistically fast (Fritz et al., 2005). Thus, plagioclase in the Taiban meteorite seems to be diaplectic glass and the lingunite appears to be formed by a solid-state transformation, as observed by Kubo et al. (2010) in their high-pressure high-temperature X-ray measurements of plagioclase.

### 2.5.4 Static pressure equivalent

According to the results of static high-pressure melting experiments of the Allende meteorite (Agee et al., 1995), the presence of crystals of ringwoodite, majorite, high-Ca pyroxene, and traces of wadsleyite can constrain the *P-T* formation conditions for the studied silicate pocket to 17–20 GPa with a *T*max in the range 1850–1900 K. The presence of Fe-Ni droplets and various sulfides in droplets and filling cracks is also consistent with that *P-T* range. Our Raman and SEM observations in the studied sample did not yield signals corresponding to higher pressure phases such as magnesiowüstite or silicate perovskite, thus the static pressure equivalent is probably below 20 GPa.

## 2.6 Conclusions

The present study in the Taiban heavily shocked L6 chondrite effectively uses micro Raman mapping and multi wavelength measurements to detect and characterize olivine, wadsleyite, ringwoodite, high-Ca clinopyroxene, majorite-pyrope, jadeite, maskelynite, and lingunite inside lithic pockets contained in the opaque melt vein crossing the sample. The

analysis of the Raman spectra and electron probe microanalysis show that the ringwoodite formed directly from olivine through a solid-state transformation involving chemical fractionation between Fe andMg. Furthermore, a Raman resonance that follows a close correlation with the color of the ringwoodite was found and carefully confirmed. Based in this result, I suggest that the blue color of the ringwoodite is likely caused by a small amount of iron in four-fold coordination inside the spinel structure of the ringwoodite. This data on ringwoodite can help understand the behavior of the mantle transition zone since ringwoodite is thought to be one of the major phases in that layer of the Earth. The remaining Raman data on the other mineral phases will help better understand Raman measurements of shocked meteorite samples. I also describe the mineral assemblages and provide possible formation conditions, which, in combination with other studies on the topic, can help improve our understanding of shock metamorphism This study also demonstrates the great potential of Raman spectroscopy, both with multiple excitation wavelengths and Raman mapping, to analyze meteorite material beyond simple mineral identification.

# CHAPTER 3: REMOTE RAMAN EFFICIECIES AND CROSS SECTIONS OF ORGANIC AND INORGANIC CHEMICALS

Accepted for publication in its present from as Acosta-Maeda, T.E., Misra, A.K., Porter, J.N., Bates, D.E., and Sharma, S.K. (2016) Remote Raman efficiencies and cross-sections of organics and inorganic chemicals. Applied spectroscopy (Accepted).

## 3.1 Abstract

Raman cross sections of various organic liquids and inorganic polyatomic ions in aqueous solutions were determined using a 532 nm pulsed laser using remote Raman systems developed at the University of Hawai‘i. The intensity counts in the spectrum of the light from the integrating sphere measured with UH remote Raman instrument were converted to spectral radiance using a calibrated integrating sphere as a light source. From these data a response function of the remote Raman instrument was obtained. Remote Raman data from a standard 1 mm path length fused silica spectrophotometer cell filled with cyclohexane were collected with the intensity calibrated instrument. The measured value of the differential Raman cross section for the 801 $cm^{-1}$ vibrational mode of cyclohexane is $4.55 \cdot 10^{-30}$ $cm^2$ $molecule^{-1}$ $sr^{-1}$ when excited by a 532 nm laser, in good agreement with the values reported in the literature. Using the measured cyclohexane Raman cross section as a reference and relative Raman mode intensities of the various ions and organic liquids, the Raman cross sections of the strongest Raman lines of nitrate, sulfate, carbonate, phosphate ions and organic liquids were calculated by maintaining the same experimental conditions for remote Raman detection. These relative Raman cross-section values will be useful for estimating detection capabilities of remote Raman systems for planetary exploration.

## 3.2 Introduction

Raman spectroscopy has been recognized as a powerful tool for material characterization. Raman spectra stem from the energy exchange between a light source and molecular vibrational modes. Because vibrational modes depend on the atoms, chemical bonds, and structure of each molecule, Raman spectra are unique to each compound. Crystal lattice modes also appear in Raman spectra, providing a means of distinction between polymorphs of the same chemical composition. Raman spectroscopy can be performed without sample preparation from gases, liquids, and solids phases. Based on recent advancements, it can also be performed during daytime conditions (Misra et al., 2005; Misra et al., 2006; Misra et al., 2007; Sharma et al., 2002). Not surprisingly, Raman spectroscopy has been extensively used in diverse fields such as chemical engineering (Moreno et al., 2011), graphene studies (Graf et al., 2007), explosive detection (Gaft and Nagli, 2008), and geology (Hanesch, 2009). Furthermore, Raman spectroscopy can be used to analyze organics and biogenic materials (Kamemoto et al., 2010; Steele et al., 2012). Its versatility makes

Raman spectroscopy excellent for planetary science (e.g., Acosta-Maeda et al., 2013) and it has been proposed as a tool for-onsite planetary exploration (Wiens et al., 2005).

Since its inception, Raman spectroscopy has traditionally been used in combination with microscopes to optimize the signal and increase spatial resolution. The first use of Raman as a remote sensing tool was during the 1970s (Hirschfeld, 1974), however, it was not until the early 2000s (Sharma et al., 2002) with the development of pulsed lasers and gated receivers that progress was made. In recent years, extensive research on remote Raman for the characterization of materials of interest for planetary science has been taken place (Misra et al., 2005; Misra et al., 2006; Rull et al., 2011; Sharma et al., 2010; Sharma et al., 2011; Sharma et al., 2006; Sharma et al., 2009; Sharma et al., 2007). A remote Raman system mounted on an exploration rover can interrogate larger areas around the rover, saving operational time and keeping the vehicle away from dangerous surfaces. NASA acknowledged this and included remote Raman capabilities with the Supercam instrument of the Mars 2020 rover mission (Wiens et al., 2016). The modern remote Raman systems use pulsed lasers and gated detection, allowing measurements in daylight conditions and avoiding long-lived fluorescence (a frequent problem while measuring mineral samples). In these systems an intensified charged coupled device (ICCD) is timed with the arrival of a Q-switch pulsed laser and the target is measured at remote distances, in the backscatter geometry. Similarly, remote Raman has been studied as a possible tool to detect explosive or dangerous chemicals from a safe distance (Carter et al., 2005a; Hokr et al., 2014; Misra et al., 2012; Moros et al., 2011; Scaffidi et al., 2010; Zachhuber et al., 2011a; Zachhuber et al., 2011b)

The cross section is a quantum mechanical physics term. It corresponds to an effective area which size is proportional to the probability of occurrence of a scattering event involving discrete particles. In Raman spectroscopy the cross section quantifies the likelihood of an inelastic Raman scattering event taking place. The Raman cross section of a particular Raman shift, $\sigma_s$, is proportional to the probability of an incident excitation photon being scattered as a Raman shifted photon. In a Raman experiment, the Raman intensity depends on multiple experimental variables such as the excitation laser power, sample density and absorbance, or optical collection efficiency. Therefore, the Raman cross section is the only constant across experiments. Raman cross sections are empirically determined and relate to the intrinsic Raman emission intensity of a chemical phase (McCreery, 2000).

Chemicals with a large Raman cross section are easier to measure, require less laser excitation power, and yield higher peak intensities and signal to noise ratios when compared

to chemicals with lower Raman cross sections in the same proportions. Conversely, low Raman cross section materials will produce weaker spectra.

Knowing the Raman cross sections of potential samples is critical to understanding spectra involving several components, that would likely include both strong and weak Raman scatters, and to attempt to approach any quantification analysis. Providing cross sections for various wavelengths is also necessary to calculating frequency independent cross sections and identify Raman resonance frequencies (Nagli et al., 2008). Raman cross sections are also important for comparing the efficiency of emerging Raman techniques such as Surface Enhanced Raman Spectroscopy (SERS) (Silva et al., 2014), resonance Raman spectroscopy (Le Ru et al., 2012), tip enhanced Raman spectroscopy (van Schrojenstein Lantman et al., 2012), or Stimulated Raman Spectroscopy (SRS) (Hokr et al., 2014; McClung and Weiner, 1964). The frequency-doubled emission of a Nd-YAG laser has a wavelength of 532 nm and is widely used in remote Raman applications. In addition, some micro Raman applications use the same wavelength. As a notable example, the Raman Laser Spectrometer set in the payload of the ESA's ExoMars mission is fitted with a 532 nm laser (Edwards et al., 2012; Lopez-Reyes et al., 2013). Very few Raman cross sections have been reported for 532 nm laser excitation (Aggarwal et al., 2012; Cançado et al., 2007; Faris and Copeland, 1997; Shim et al., 2008) in materials such as nanographites, diamond, or water. This study aims fill the lack of cross section values of Raman vibrations that could be encountered in geosciences, planetary exploration, and astrobiology. The selected sample suite includes: nitrates, which are found in semi-arid environments; carbonates and borates, which are frequently formed as evaporates; and sulfates, which are present in the Meridiani region of Mars. The detection of bonds such as C-H, C-H or C-Cl is fundamental in the search of organic or biogenic matter. The data and calculated cross sections presented in this chapter are acquired in the backscattered geometry common to most remote Raman experiments. Because the collection solid angle is small for all the remote experiments, the angular dependence of the Raman scattering can be neglected. The results are also applicable to shorter distances, such as micro-Raman systems, although caution should be used because of the larger collection solid angle, which includes scattering at large angles around the 180º backscatter angle.

### 3.3 Theory

Two versions of the Raman cross section are usually provided, the absolute cross section and differential cross section. The absolute, or integrated, cross section is measured

over the full sphere around the sample and over the wavelength range of a Raman band. The differential cross section is defined as the cross section per unit angle and it depends on the observation geometry because of the anisotropy of the Raman Effect (Damen et al., 1965). The differential Raman cross section is given in units of [$cm^2$ $sr^{-1}$ $molecule^{-1}$] ($cm^2$ $sr^{-1}$ $molec^{-1}$, sr = steradian) and expressed as

$$\beta = \frac{d\sigma}{\mathrm{d}\Omega} \quad (3.1)$$

where σ is the integrated Raman cross-section and Ω the solid angle of collection. To obtain the differential Raman cross section of the cyclohexane 801 $cm^{-1}$ peak one must start by obtaining the efficiency of the system. The efficiency of a Raman system is defined as (Stopar et al., 2005):

$$Raman\ efficiency = \frac{power\ of\ Raman\ peak}{Input\ laser\ power} \quad (3.2)$$

for a pulsed laser in a remote Raman system, the input laser power is

$$Input\ laser\ power = pulse\ energy \cdot laser\ frequency \quad (3.3)$$

and the power of a Raman peak is

$$Power\ of\ Raman\ Peak = L_\lambda \cdot \Delta\lambda \cdot \Omega \cdot A \quad (3.4)$$

where $L_\lambda$ and Δλ are the spectral radiance and the full width at half maximum (FWHM) of the Raman peak, Ω is the solid angle subtended by the telescope at the measurement distance, and A is the area of the Raman source (the area of the laser spot).

The Raman cross section of a Raman peak can then be calculated following the equation (McCreery, 2002)

$$L_\lambda \Delta\lambda = (P/A)\beta N(r)\, x \quad (3.5)$$

where $L_\lambda$ is the spectral radiance of the Raman peak in watts $sr^{-1}$ $cm^{-2}$ and $\Delta\lambda$ its FWHM in nm. P/A is the laser power per unit area in watts $cm^{-2}$, $\beta$ is the differential cross section, N (r) is the number density of molecules in the measured sample in molecules per unit volume and x is the sample path length. Rearranging the terms to obtain the cross section one obtains

$$\beta = \frac{L_\lambda \Delta\lambda \, A}{P \, N(r) \, x} \qquad (3.6).$$

One must use this approach to determine the differential Raman cross section of the 801 $cm^{-1}$ peak of cyclohexane.

The integrated intensity of a single Raman peak $I_{R,s}$ can be calculated as

$$I_{R,s} = I_0 \Omega \int_0^x \beta_s \; N_s \; T(l)^2 dl \approx I_0 \Omega \sum_{i=1}^{n} \beta_i \; N_{s,i} \; T_i^2 \Delta l \qquad (3.7),$$

where the subscript R,s refers to the number of Raman photons for a particular Raman line of a liquid sample present (i.e., cyclohexane) in the spectrum, $I_o$ refers to the number of incident photons, $\beta_s$ is the Raman differential cross section for a particular peak of the sample [$cm^2 molec^{-1} sr^{-1}$], $N_s$ is the molecular concentration of the sample [molecules $vol^{-1}$], $T(l)^2$ is the two-way transmission from the front of the sample to the depth l, and $\Omega$ is the solid angle of the collection optics for a particular distance from the sample in steradians [sr]. For remote Raman measurements the distance between the sample and telescope is large compared with the size of the sample, therefore $\Omega$ is taken as a constant. In the summation form, $T_i^2$ refers to the two way transmission from the front of the sample to position i, and $\Delta l$ is a constant such that $n \cdot \Delta l = x$, where n is a positive integer large enough to describe the sample and x is the distance the laser travels inside the sample. Assuming the transmission through air between the sample and the collection optics is 1, the two-way transmission through the sample is given by

$$T(l)^2 = T_{\lambda_{0,lq}} \cdot T_{\lambda_{R,lq}} = e^{-\alpha_{\lambda_{0,lq}} l} \cdot e^{-\alpha_{\lambda_{R,lq}} l} = e^{-(\alpha_{\lambda_{0,lq}} + \alpha_{\lambda_{R,lq}}) l} \qquad (3.8)$$

where $T_{\lambda_{0,lq}}$ is the transmission of the liquid at the excitation wavelength, $T_{\lambda_{R,lq}}$ is the transmission of the liquid at the wavelength of the selected Raman peak of the sample, $\alpha_{\lambda_{0,lq}}$

is the extinction coefficient of the liquid at the excitation wavelength, and $\alpha_{\lambda_{R,lq}}$ is the extinction coefficient of the liquid at the wavelength of the selected Raman peak of the sample. Completing the integral shown in eq. (7) one obtains:

$$I_{R,s} = \frac{I_0 \beta_s N_s \Omega}{(\alpha_{\lambda_{0,lq}} + \alpha_{\lambda_{R,lq}})} (1 - e^{-(\alpha_{\lambda_{0,lq}} + \alpha_{\lambda_{R,lq}})x}). \qquad (3.9).$$

Taking the ratio of the integrated Raman signal for a particular peak of the sample ($I_{R,s}$) versus a particular peak of some different reference sample ($I_{R,ref}$) (for which the Raman cross section is known $\sigma_{ref}$ ) results in the following equation:

$$\frac{I_{R,s}}{I_{R,ref}} = \frac{\beta_s \ N_s \ (\alpha_{\lambda_{0,lq,ref}} + \alpha_{\lambda_{R,lq,ref}}) \ (1 - e^{-(\alpha_{\lambda_{0,lq}} + \alpha_{\lambda_{R,lq}})x})}{\beta_{ref} \ N_{ref} \ (\alpha_{\lambda_{0,lq}} + \alpha_{\lambda_{R,lq}})(1 - e^{-(\alpha_{\lambda_{0,lq,ref}} + \alpha_{\lambda_{R,lq,ref}})x})} \qquad (3.10).$$

Solving for the differential cross section for a particular peak of the sample

$$\beta_s = \beta_{ref} \ \frac{I_{R,s} \ N_{ref}}{I_{R,ref} \ N_s} \ \frac{(\alpha_{\lambda_{0,lq}} + \alpha_{\lambda_{R,lq}})(1 - e^{-(\alpha_{\lambda_{0,lq,ref}} + \alpha_{\lambda_{R,lq,ref}})x})}{(\alpha_{\lambda_{0,lq,ref}} + \alpha_{\lambda_{R,lq,ref}}) \ (1 - e^{-(\alpha_{\lambda_{0,lq}} + \alpha_{\lambda_{R,lq}})x})} \qquad (3.11).$$

Equation (11) can be used to calculate the differential Raman cross section ($\beta_s$) at a particular wavelength for any peak in the Raman spectra of a sample, provided a reference cross section is known. For the calculations in this chapter, the cyclohexane cross section was first obtained and then used as a reference cross section.

In the absence of resonance Raman Effect the cross section increases as the excitation wavelength decreases following the $4^{th}$ power excitation frequency dependence of the Raman cross section given by:

$$\beta_j = \beta_j^0 \upsilon^0 (\upsilon^0 - \upsilon_j)^3 \qquad (3.12),$$

where $\beta_j^0$ is the frequency independent cross section of the $j^{th}$ vibrational mode, $\upsilon^0$ is the wavenumber of the excitation laser wavelength, and $\upsilon_j$ is the wavenumber of the Raman peak j (McCreery, 2002).

### 3.4 Experimental procedure

#### 3.4.1 Samples

The sample set analyzed for this study includes: cyclohexane ($C_6H_{12}$, ACS, purchased from Fisher Scientific); potassium carbonate ($K_2CO_3$); potassium nitrate ($KNO_3$); ammonium nitrate ($NH_4NO_3$); potassium sulfate ($K_2SO_4$); sodium phosphate ($Na_3PO_4$); potassium chlorate ($KClO_3$); sodium tetraborate octahydrate ($Na_2[B_4O_5(OH)_5]\cdot 8H_2O$) purchased from Fisher Scientific; and potassium perchlorate ($KClO_4$, 99% purchased from Alfa Aesar). The organic liquids analyzed (purchased from Fisher Scientific) include: acetone ($(CH_3)_2CO$); acetonitrile ($CH_3CN$); methanol ($CH_3OH$); ethanol ($CH_3CH_2OH$); carbon tetrachloride ($CCl_4$); benzene ($C_6H_6$); nitrobenzene ($C_6H_5NO_2$); dichloromethane ($CH_2Cl_2$); and 2-propanol ($CH_3CHOHCH_3$). The distilled water ($H_2O$) was purchased from Menehune Water Company. The liquid samples were used as purchased. Water solutions of the powdered samples were made and concentrations below the solubility limits of each chemical were chosen, with the exception of the sodium borate. Because of the low Raman signal of the borate, a supersaturated solution was prepared and he Raman measurements were taken immediately after reaching room temperature.

#### 3.4.2. Raman Systems

Two different remote Raman systems were used to acquire the spectra used as standard for Raman cross section determination. A first fiber-coupled, 5-inch remote Raman system was used to obtain the Raman cross section of cyclohexane. A second improved, more sensitive, directly-coupled remote Raman system was used to obtain the spectra of inorganic salt solutions and organic liquids, along with the cyclohexane as a reference.

The 5-inch remote Raman system used to determine the Raman cross section of cyclohexane is composed of a 5-inch Meade ETX-125 Maksutov-Cassegrain telescope (125 mm clear aperture, 1900 mm focal length F/15), a Kaiser Optical Systems Holospec spectrometer (F/1.8) fitted with a Princeton Instruments Inc. I-MAX-1024-E intensified CCD detector, and a 532 nm mini Nd:YAG laser (Model ULTRA CFR, Big Sky Laser, 20 Hz, 8 ns/pulse) with a maximum power of 35 mJ/pulse. A similar system has been described and demonstrated by Sharma et al. (2002, 2003).

The spectra obtained were used to determine the Raman cross section of the polyatomic ions of inorganic salts and organic liquids via an improved remote Raman system composed of an 8-inch Advanced Ritchey-Cretien telescope (Meade LX200, 203 mm clear aperture, F/10), Kaiser Optical Systems F/1.8 HoloSpec spectrometer, thermo-electrically

Table 3.1:: Molecular weight, molar concentration, and estimated concentration for samples.

| **sample** | Concentration (mg/ml) | Molecular weight (g/mol) | Molar con-centration (mol/L) | Error[(b)] ± |
|---|---|---|---|---|
| $K_2CO_3$ | 100.47 | 138.2055 | 0.7270 | 0.0030 |
| $KNO_3$ | 101.845 | 101.1032 | 1.0073 | 0.0042 |
| $NH_4NO_3$ | 100.02 | 80.04336 | 1.2496 | 0.0052 |
| $Na_3PO_4$ $12H_2O$ | 15.512 | 380.1170 | 0.2495 | 0.0010 |
| $PO_4^{-3}$ [(a)] | 19.77305 | 94.9714 | 0.1633 | 0.0006 |
| $K_2SO_4$ | 99.955 | 174.2592 | 0.5736 | 0.0024 |
| $KClO_3$ | 69.89 | 122.5495 | 0.5703 | 0.0024 |
| $KClO_4$ | 14.775 | 138.5489 | 0.1066 | 0.0004 |
| $Na_2[B_4O_5(OH)_4]$ $8H_2O$ | 95.82115 | 381.3721 | 0.2513 | 0.0010 |
| acetone $(CH_3)_2CO$ | | 58.07914 | 13.6366 | 0.0172 |
| acetonitrile $CH_3CN$ | | 41.05192 | 19.1465 | 0.0244 |
| cyclohexane $C_6H_{12}$ | | 84.15948 | 9.2455 | 0.0119 |
| methanol $CH_3OH$ | | 32.04186 | 24.7114 | 0.0312 |
| ethanol $CH_3CH_2OH$ | | 46.06844 | 17.1267 | 0.0217 |
| carbon tetrachloride $CCl_4$ | | 153.8227 | 10.3151 | 0.0065 |
| benzene $C_6H_6$ | | 78.11184 | 11.2211 | 0.0128 |
| nitrobenzene $C_6H_5NO_2$ | | 123.1094 | 9.7393 | 0.0081 |
| dichloromethane $CH_2Cl_2$ | | 84.93258 | 15.6065 | 0.0118 |
| 2 propanol $C_3H_7OH$ | | 60.09502 | 13.0793 | 0.0166 |
| DI water $H_2O$ | | 18.01528 | 55.4085 | 0.0555 |

(a)The estimated amount of $PO_4^{-3}$ was obtained from standard polypropic acid buffer calculations. (b) Possible error in molarity estimated by error propagation from possible errors in the volume and mass measurements. For the pure liquids a maximum density error of ± 1 g/L was assumed.

cooled intensified CCD detector (Princeton Instruments PI-MAX), and Quantel Nd:YAG Q-switched Laser (CFR model, 532 nm emission, 100 mJ/p, 15 Hz, 10 ns per pulse). The telescope is coupled to the spectrometer through a 50 mm F/1.8 camera lens. The 532 nm Rayleigh scattering is rejected with a 532 nm Supernotch filter from Kaiser Optical Systems. This system can measure carbonate, sulfate, and nitrate containing chemicals and benzene at 120 m distance with single laser pulse excitation (~100 ns total measurement time). The details of this system and its schematics are described in Misra et al. (2012).

### 3.4.3 Methods

The 5-inch remote Raman system used for the absolute intensity calibration of cyclohexane was intensity calibrated by measuring a calibrated integrating sphere illuminated by a halogen tungsten lamp. The telescope of the 5-inch remote Raman system was focused on the front surface of the integrating sphere at a distance of 8.76 m. The field of view of the spectrometer at the target was set to 1 cm by fiber coupling the receiving optics to the spectrometer and adjusting the coupling optics of the system to match that field of view. The laser was later set to 1-cm spot at the same distance, 8.76 m. The intensity data were collected after the current of the tungsten lamp had completely stabilized, indicating that the temperature of the black body radiation emitted by the sphere is constant. A total of 100 spectra of 0.5 seconds exposure were collected using a 100 micron slit width. A large number of spectra (100) was averaged to improve the signal to noise ratio and minimize the effect of random noise. The final number of counts was transformed to 1 second equivalent to obtain the response function of the system. Once the response function has been determined, the spectral intensity counts can be converted to spectral radiance by dividing the measured counts by the response function of the system. The Raman signal is proportional to the number of molecules excited by the laser. In order to obtain a Raman cross-section, it is fundamental to know the exact number of molecules in the laser beam path. For clear liquids, the number of molecules excited by the laser is proportional to the volume of liquid in the laser beam path. To control the measured volume, the remote Raman data were collected from cyclohexane contained in a standard 1 mm path length fused-silica spectrophotometer cell. As described previously, the diameter of the laser beam at sample was set to 1 cm, thus totally enforcing the sample size. The cross section reference spectra of cyclohexane were measured with 60 seconds exposure time (1200 laser pulses).

In order to obtain the cross sections of the selected Raman bands in the inorganic salts and organic liquids the first term of equation (3.11) was calculated, using the integrated Raman signal of the 801 $cm^{-1}$ peak of cyclohexane as $I_{R,ref}$, calculated cross section for the 801 $cm^{-1}$ as $\beta_{ref}$, and the integrated Raman signal for a particular peak of the sample as $I_{R,s}$. In order to determine $I_{R,s}$ the Raman spectrum of the pure organic liquids were obtained. Determining $I_{R,s}$ of the inorganic salts Raman spectra in a water solution was done to obtain transparent samples and more accurately estimate the number of excited molecules. The results will serve as a baseline for future cross section measurements of the same chemicals in solid form where other factors greatly influence the Raman efficiency such as grain size,

impurities or internal dispersion. Significant peaks were selected for each sample, based on signal strength and relevance criteria. The concentration of each solution was selected to maximize the Raman signal without increasing absorption of the excitation wavelength. The concentration of each inorganic salt in water solution was determined (Table 3.1), along with the molecular weight, molar concentration, and error in the molar concentration for each sample. The estimated error in the concentration stems from the scale errors incurred while measuring weight and pipetting. Each sample, including the cyclohexane used as standard, was placed in identical 20 ml borosilicate glass vials. A custom holder was made to place each vial in the exact same position at 8.76 m from the collection optics (telescope), ensuring that every spectrum was acquired under the same conditions. A small correction was applied to account for the difference in measured volume produced by the different refractive index of each sample, as the edge of the 1 cm diameter beam bends between 4.9º and 7.4º as it enters the cylindrical borosilicate glass vials, for the lowest and highest refraction index (water and nitrobenzene, respectively). This correction was tested by confirming the final cross section result of the 993 $cm^{-1}$ band of benzene as measured along with cyclohexane in a 1 cm square, fused-silica spectrometer cell, where a correction for refraction is not necessary. The results were within 3% of each other. The laser power was 25 mJ per pulse at 15 Hz. Five consecutive spectra were recorded over 150 laser pulses for all the samples to ensure good quality Raman spectra and averaging out shot to shot variation in signal to noise ratio.

Every spectrum was wavelength and intensity calibrated using the custom Matlab software UH Raman-LIBS v1.61. The wavelength calibration was performed using the Raman peaks of calcium carbonate, cyclohexane, acetonitrile, benzene, calcium sulfate dihydrate, and the wavelengths of the emission of a neon lamp as a reference. The intensity calibration was performed using the emission of a Kaiser Optical Systems calibration accessory as a reference. This calibration accessory is equipped with a tungsten white lamp accompanied by matching calibration data in units of photons per area per second per wavenumber (photons $cm^{-2}$ $s^{-1}$ $(cm^{-1})^{-1}$) versus wavelength. The UH Raman-LIBS software takes a measured reference spectra of the lamp and obtains a calibration ratio with the calibration data that is later applied to every spectrum. This calibration is relative and removes the contribution of the response function of the system and is a critical step in obtaining the cross sections using a known cross section reference (McCreery, 2002).

Finally, the $I_{R,S}$ value for each studied Raman peak was defined by the total spectral area of the peak, and is proportional to the number of measured photons. Curve fitting was

used for isolated or moderately overlapping Raman peaks for isolated or moderately overlapping Raman peaks, such as the cyclohexane 801 $cm^{-1}$, and total integrated area along a Raman shift range for overlapping Raman signals, such as the C-H Raman lines of cyclohexane in the range 2730-3080 $cm^{-1}$. Peak fittings and spectral integrations were performed with the Grams/AI 8.0 software package (Thermo-Fisher Scientific, Inc.).

## 3.5 Results and discussion

### 3.5.1 Absolute intensity calibration of cyclohexane.

The calibrated spectral radiance of the integrating sphere as a function of wavelength (Fig. 3.1) provided values of spectral radiance ($L_\lambda$) of the integrating sphere in units of [Watts $sr^{-1}$ $cm^{-2}$ $nm^{-1}$] as a function of wavelength (in nm) for a lamp aperture size of 10 mm. The data were fitted to a polynomial equation to obtain intermediate values of $L_\lambda$. Next, the response function was obtained for the 5-inch remote Raman system from the data obtained from the measurement of the integrating sphere and calibrated spectral radiance data (Fig. 3.1) as number of counts per second per spectral radiance to determine the response function for the system (Fig. 3.2).

The measured Raman intensity of cyclohexane in number of counts versus wavelength in the x axis (in nm) was normalized to 1 s exposure and 1 cm sample path (Fig. 3). The spectral radiance of the cyclohexane was calculated from a division of the number of normalized counts by the response function. The spectral radiance of the sample is given as a

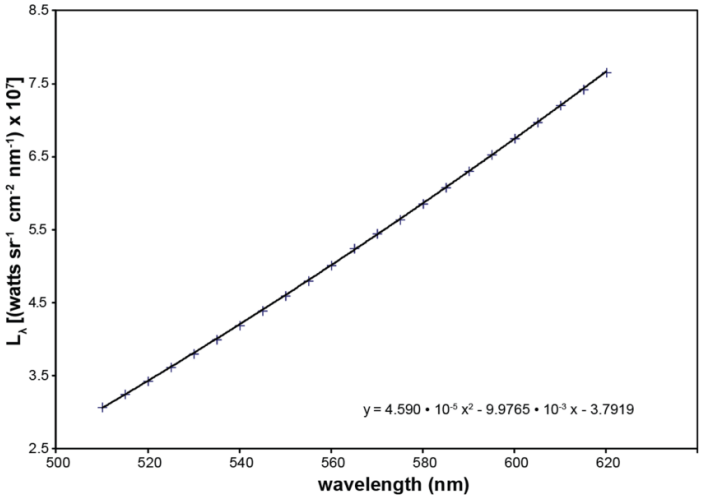


Figure 3.1: Polynomial function used as reference spectral radiance of the integrating sphere. The polynomial function is plotted along its equation and manufacturer provided calibration points (+).

function of wavelength (Fig. 3.4). The input power of the laser was obtained using equation (3.3), the spectral radiance ($L_\lambda$) of the 801 $cm^{-1}$ peak of cyclohexane using equation (3.4), and the Raman efficiency of the 801 $cm^{-1}$ peak of cyclohexane using equation (3.2). The experimental parameters were summarized (Table 3.2 ) for the remote Raman setup using 5-inch telescope and the 801 $cm^{-1}$ Raman peak of cyclohexane. For a Maksutov-Cassegrain telescope the effective area is the area of the primary mirror minus the area of the central obstruction (secondary mirror). Listed are the spectral radiance ($L_\lambda$), full width at half maximum ($\Delta\lambda$), sample distance from the target (R), telescope area, solid angle subtended by the telescope at the measurement distance ($\Omega$), laser parameters, and Raman efficiency for the subtended angle. Assuming that Raman Scattering is isotropic, the total Raman efficiency of cyclohexane over a $4\pi$ solid angle is $3.19 \cdot 10^{-7}$.

The Raman cross section of cyclohexane was calculated following equation (3.5), substituting the spectral radiance of the cyclohexane 801 $cm^{-1}$ peak in watts $sr^{-1}$ $cm^{-2}$ as $L_\lambda$ and its FWHM in nm (Table 3.3). The laser beam parameters are represented by P and A, N (r) is the number density of molecules in the cyclohexane sample in molecules per unit volume, and x = 1 cm is assumed as the sample path length. The actual sample path length was 0.1 cm, however, in the calculation the counts are normalized to 1 cm.

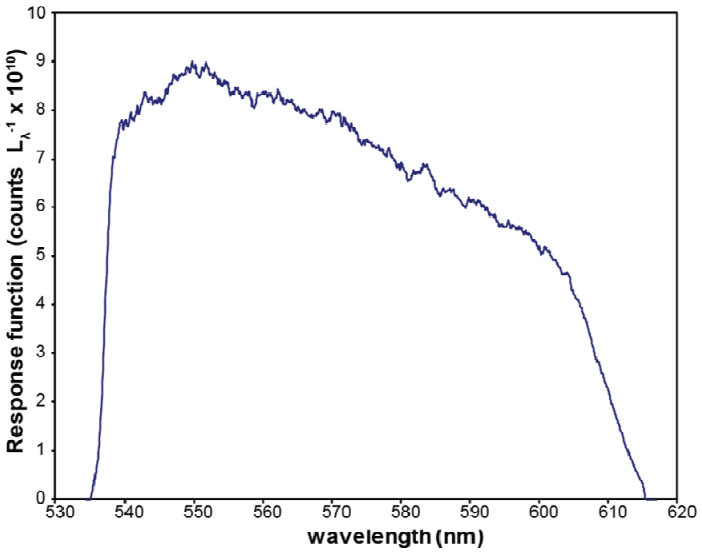


Figure 3.2: Response function of the 5-inch remote Raman system in counts per spectral radiance. The system is most sensitive in the green region of the spectrum (545-560 nm)

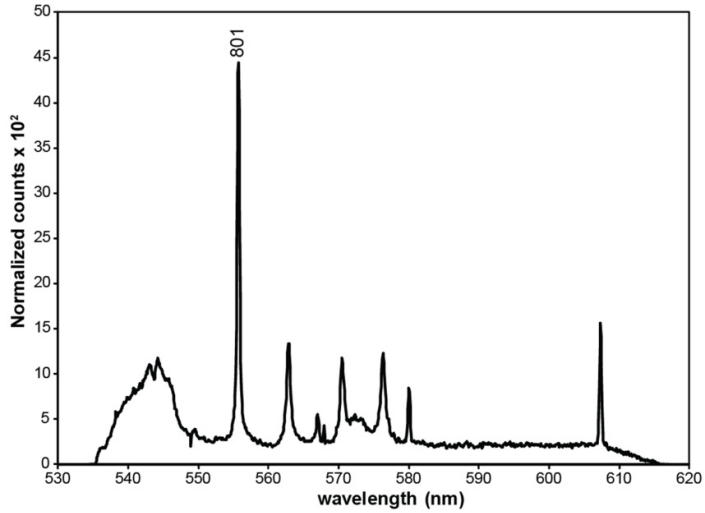


Figure 3.3: Cyclohexane remote Raman spectrum recorded with the 5-inch remote Raman system with 60 seconds exposure time (1200 laser pulses), beam diameter 1 cm, 1-mm sample path, 8.76 m range. Counts have been scaled to 1 s exposure time (20 pulses) and 1-cm sample path. The 801 cm-1 peak of cyclohexane is the major band at 555.8 nm. The Raman bands of atmospheric oxygen and nitrogen appear at 580.1 and 607.4 nm (1555 and 2331 cm-1), respectively. The Raman signal of the quartz spectrometer cell contributes to the spectrum with broad glass bands at around 543 and 573 nm. Note the almost 0 sensitivity at both ends.

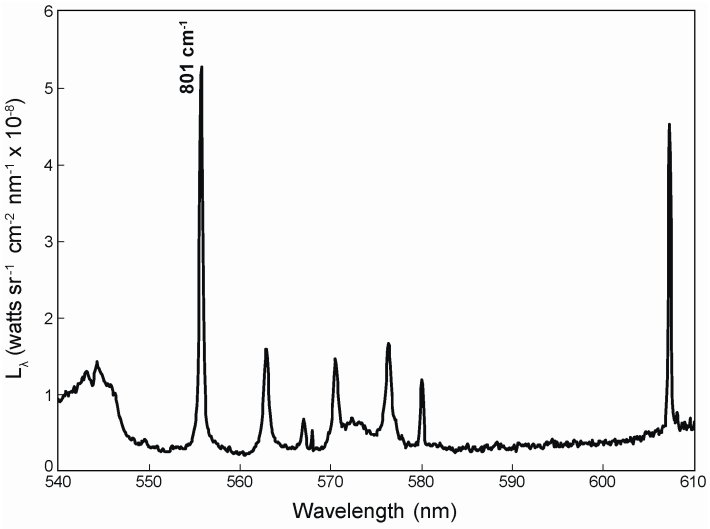


Figure 3.4: Cyclohexane remote Raman spectrum of Fig. 3.3 calibrated in units of spectral radiance. The edges, below 540 and over 615 nm have been excluded due to lack of sensitivity on the edges of the ICCD.

| Table 3.2: Measured Raman data and experimental parameters for the fiber coupled remote Raman system using 5 inch diameter Maksutov-Cassegrain telescope. | |
|---|---|
| $L_\lambda$ | $5.28 \cdot 10^{-8}$ watts $sr^{-1}$ $cm^{-2}$ $nm^{-1}$ |
| $\Delta\lambda$ | 0.42903 nm, 14.0756 $cm^{-1}$ |
| R | 876 cm |
| Telescope area | 116.7454 $cm^2$ |
| $\Omega$ | $1.52 \cdot 10^{-4}$ sr |
| Laser frequency | 20 Hz |
| Laser Pulse energy | 35 mJ |
| Input laser power | 0.7 W |
| Raman efficiency ($801cm^{-1}$) | $3.86 \cdot 10^{-12}$ |

| Table 3.3: Experimental values for the cyclohexane standard | |
|---|---|
| Raman peak | 801 $cm^{-1}$ |
| $L_\lambda$ | $5.28 \cdot 10^{-8}$ watts $sr^{-1} \cdot cm^{-2} \cdot nm^{-1}$ |
| $\Delta\lambda$ | 0.42903 nm |
| P (Power) | 0.7 W |
| A (Beam Area) | 0.785 $cm^2$ |
| N(r) | $5.5811 \cdot 10^{-21}$ molecules$\cdot cm^{-3}$ |
| X | 1 cm |

Using equation (3.6) a differential cross section is obtained for the 801 $cm^{-1}$ peak of cyclohexane for the remote Raman back scattering geometry using 532 nm pulsed laser excitation of $\beta_{532} = 4.55 \cdot 10^{-30}$ $cm^2$ $sr^{-1}$ $molec^{-1}$. The reported literature value for the Raman cross section of the 801 $cm^{-1}$ Raman peak of cyclohexane with a green wavelength excitation was obtained for 514.5 nm laser excitation in 1986. The obtained value of $\beta$ was 5.2 $cm^2$ $sr^{-1}$ $molec^{-1}$ (Trulson and Mathies, 1986). The reported cyclohexane cross section at 514.5 nm was extrapolated to the cross section at 532 nm excitation, according to the $\upsilon^4$ excitation frequency dependence of the Raman cross section, using equation (3.12).

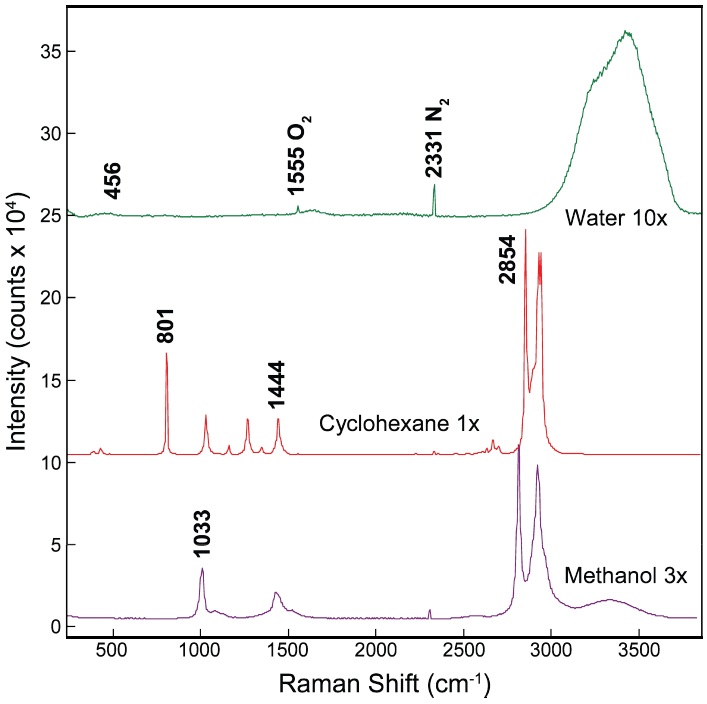


Figure 3.5: Remote Raman spectra of methanol, cyclohexane, and water using 150 pulses, ICCD gain 250, 25 mJ/pulse. The spectra of methanol and water have been shifted vertically for clarity, methanol threefold and water tenfold. It is apparent that the Raman signal of cyclohexane is about ten and three times stronger than that of the methanol and water. The signal strength and signal to noise ratio of a Raman measurement are closely related to the sample Raman cross section.

Substituting $\upsilon^o$ as the wave number of the excitation laser and $\upsilon_j$ as the wavenumber of the Raman peak, 801 $cm^{-1}$, a frequency correction factor of 1.148183 was obtained between both wavelengths as was an extrapolated cyclohexane Raman cross section at 532 nm to $\beta_{532} = 5.2x10^{-30}/1.148183 = 4.53x10^{-30}$ $cm^2$ $sr^{-1}$ $molec^{-1}$. The measured differential Raman cross-section of cyclohexane, $4.55x10^{-30}$ $cm^2$ $sr^{-1}$ $molec^{-1}$, is in good agreement with the value reported in the literature. This $\upsilon^4$ excitation frequency dependence extrapolation was used to compare the cross section results with others found in the literature. The intensity calibrated cyclohexane spectrum acquired as a reference along with the inorganic salt ions and organic liquids (Fig. 3.5) and is in good agreement with that provided by (McCreery, 2002). The intensity ratios between the C-C stretch line at 801 $cm^{-1}$ and the C-H stretching region are consistent with different measurements at the UH laboratory and the work of McCreery, and can be used as a Raman intensity standard, as stressed by McCreery.

| Table 3.4: Differential Raman cross sections for selected Raman lines. | | | | | |
|---|---|---|---|---|---|
| | Center ($cm^{-1}$) | Spectral area ($(cm^{-1})^2$ $10^5$) | Number density ratio | β ($10^{-30}$) | Error % |
| cyclohexane | **801.6** | 7.19 | 1 | 4.55 | |
| cyclohexane C-H | **2730-3080** | 88.8 | 1 | 56.2 | 3.7 |
| $K_2CO_3$ 100mg/ml | **1064.6** | 0.254 | 0.0786 | 1.91 | 4.2 |
| $KNO_3$ 100mg/ml | **1046.9** | 0.981 | 0.109 | 5.34 | 3.7 |
| $NH_4NO_3$ 100mg/ml | **1046.3** | 1.28 | 0.135 | 5.63 | 3.7 |
| $K_2SO_4$ 100mg/ml | **979.7** | 0.518 | 0.0620 | 4.96 | 4.3 |
| $Na_3PO_4$ $10H_2O$ 100mg/ml ($PO_4^{-3}$) | **936.8** | 0.0999 | 0.0177 | 3.35 | 7.8 |
| $KClO_3$ 70mg/ml | **929.9** | 0.575 | 0.0617 | 5.52 | 5.1 |
| $KClO_4$ 15mg/ml | **933.3** | 0.106 | 0.0115 | 5.45 | 7.1 |
| $Na_2[B_4O_5(OH)_4]8H_2O$ 100mg/ml ($BO_2$) | **745.0** | 0.0633 | 0.0553 | 0.679 | 7.7 |
| ($BO_3$) | **876.5** | 0.0272 | 0.0553 | 0.292 | 11.6 |
| Acetone C-C ss | **787.7** | 4.99 | 1.47 | 2.04 | 3.6 |
| C-H ss | **2925.8** | 25.8 | 1.47 | 10.6 | 3.5 |
| Acetonitrile C-C ss | **920.5** | 1.96 | 2.07 | 0.563 | 3.8 |
| C-N ss | **2252.7** | 9.95 | 2.07 | 2.86 | 4.2 |
| C-H ss | **2943.6** | 14.6 | 2.07 | 4.20 | 3.9 |
| Methanol C-O ss | **1033.5** | 3.90 | 2.67 | 0.863 | 3.7 |
| CH ss-as | **2650-3100** | 28.8 | 2.67 | 6.36 | 7.7 |
| Ethanol C-O ss | **883.1** | 2.96 | 1.85 | 0.967 | 3.5 |
| C-H ss-as | **2780-3100** | 42.0 | 1.85 | 13.7 | 3.5 |
| O-H ss-as | **3130-3670** | 7.26 | 1.85 | 2.37 | 4.1 |
| $CCl_4$ ss | **459.2** | 18.3 | 1.12 | 10.6 | 3.5 |
| sd | **217.0** | 11.0 | 1.12 | 6.39 | 3.5 |
| Benzene C-H rs | **992.9** | 25.0 | 1.21 | 13.7 | 3.5 |
| C-H ss-as | **2990-3150** | 42.7 | 1.21 | 23.3 | 3.6 |
| Nitrobenzene C-N ss | **1347.4** | 61.0 | 1.05 | 39.9 | 4.4 |
| C-H ss | **3084.3** | 31.2 | 1.05 | 20.4 | 3.6 |
| Dichloromethane C-Cl ss | **703.1** | 11.8 | 1.69 | 4.40 | 3.5 |
| CH ss | **2990.6** | 11.5 | 1.69 | 4.30 | 3.9 |
| 2-propanol | **819.4** | 3.76 | 1.42 | 1.63 | 3.5 |
| | **2917**$^+$ | 55.9 | 1.42 | 24.2 | 3.7 |
| | **3354**$^+$ | 11.7 | 1.42 | 5.04 | 4.3 |
| water O-H ss-as | **3362**$^+$ | 50.1 | 6.00 | 4.96 | 3.6 |
| O-H b | **456.3** | 0.168 | 6.00 | 0.0167 | 9.6 |

Abbreviations: symmetrical stretch (ss); antisymmetrical stretch (as); symmetric deformation (sd); ring symmetrical stretch (rs); and bending (b). Limits of integration areas are separated by a dash and + denotes centers of mass as weighted by spectral area contribution. Number density ratio is the number density ratio versus the cyclohexane standard.

The C-H stretching region of cyclohexane shows prominent lines at 2854 $cm^{-1}$, corresponding to $CH_2$ symmetrical stretch vibrations, and two bands 2924 and 2940 $cm^{-1}$ corresponding to $CH_2$ antisymmetric stretch vibrations enhanced by Fermi resonance with the 1$^{st}$ overtone of the $CH_2$ scissors vibration found at 1462 $cm^{-1}$ (as a shoulder of the more intense 1444 $cm^{-1}$). The Raman cross section of the C-H stretch region of cyclohexane was determinined by integrating the spectral intensity between 2730 and 3080 $cm^{-1}$ and obtained a value of $5.62x10^{-29}$ $cm^2$ $sr^{-1}$ $molec^{-1}$. This is also in very good agreement with the value provided by Trulson and Mathies (1986) for 532 nm pulsed laser excitation, $5.73x10^{-29}$ $cm^2$ $sr^{-1}$ $molec^{-1}$, for the same spectral region.

The remote Raman measurements taken with the 8-inch remote Raman system a (Figs. 3.5 through 3.15) show some contribution of atmospheric gases as all measurements were performed in air with the laboratory lights on and at room temperature. The Raman signals corresponding to symmetrical stretching vibrations of $O_2$ and $N_2$ molecules appear in every spectra at 1555 and 2331 $cm^{-1}$ with the same intensity because the same amount of air column was excited by the remote Raman system between the system and the targets. These signals can be used to visualize the spectral intensities of the Raman bands of each sample, and provide an estimate of their relative Raman efficiencies. In the Raman spectra of solutions, the water Raman bands from the solvent overlap with the Raman spectrum of the solute. The differential Raman cross sections obtained for the cyclohexane 801 $cm^{-1}$ and C-H stretch bands and the cross section for each selected Raman band in each of the studied samples are summarized (Table 3.4). The concentration of the solutions are described where applicable, estimated spectral area are obtained from peak fittings and integrations, and molecular number density ratio is given with respect to that of cyclohexane (where <1 means lower molecules for unit volume than cyclohexane, and >1 more molecules, respectively). The cross section is expressed in units of $cm^2$ $sr^{-1}$ $molecule^{-1}$. The listed errors (Table 3.4) stem from possible errors in the volume and mass measurements, the shot to shot variability and reproducibility of the peak fitting and integrations procedure.

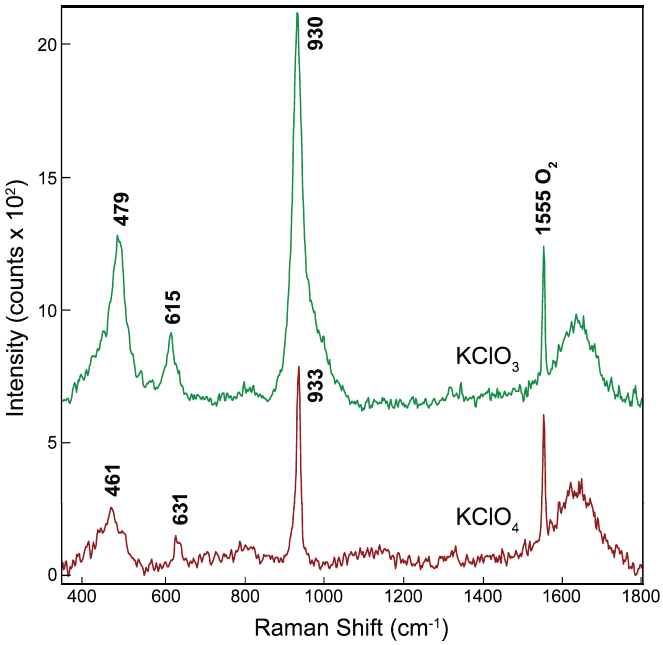


Figure 3.6 Remote Raman spectra of the 70 mg/ml $KClO_3$ water solution and 15 mg/ml $K_2ClO_4$ water solution. Same experimental conditions as Fig. 3.5.

### 3.5.2 Cross section of $ClO_3$ and $ClO_4$ ions

The remote Raman spectrum of the 70 mg/ml solution of $KClO_3$ along with the remote Raman spectrum of the 15 mg/ml $KClO_4$ solution were measured (Fig. 3.6). The three main signals in the $KClO_3$ spectrum at 930, 615, and 479 $cm^{-1}$ correspond to vibrations of the $ClO_3^-$ ions. The main band at 930 $cm^{-1}$ is produced by the symmetrical stretching vibration of the Cl-O bonds and has a calculated cross section of 5.52 x $10^{-30}$ $cm^2$ $sr^{-1}$ $molec^{-1}$. Two additional bands appear at 479 and 615 $cm^{-1}$ corresponding to the $\upsilon_3$ and $\upsilon_4$ vibrational modes of the $ClO_3^-$ ions (Ramdas, 1953; Robinson, 1963; Sprowles and Plane, 1975). The spectrum also shows the O-H bending modes of the water solvent at around 1630 $cm^{-1}$. These peaks appear in the subsequent Raman spectra of water solutions along with the Raman lines of the different polyatomic species. The Raman spectrum of the 15 mg/ml solution of $KClO_4$ (Fig. 3.6) shows its characteristic main vibration at 933 $cm^{-1}$ corresponding to the symmetrical stretching vibration of the tetrahedral ion $ClO_4^-$ with a calculated cross section of 5.45·$cm^2$ $sr^{-1}$ $molec^{-1}$. Additional bands appear in the spectrum at 461 and 631 $cm^{-1}$ in good accordance with previous measurements (Ross, 1962; Stein and Appelman, 1983). The value of the differential Raman cross section of the main band is on the order of that in Dudik et al. (1985) adjusted for 532 nm using equation (12), 11.06 x $10^{-30}$ $cm^2$ $sr^{-1}$ $molec^{-1}$. The factor of

two difference probably arises from the reference data used for that study (Abe et al., 1977), which was obtained from Raman measurements of a solution of benzene and cyclohexane with different excitation wavelengths and scattering geometries.

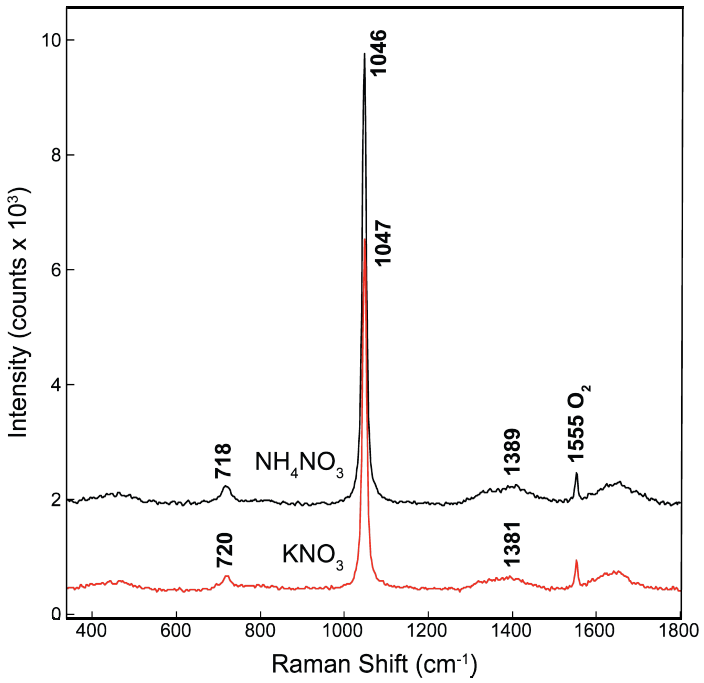


Figure 3.7: Remote Raman spectra of the 100 mg/ml $KNO_3$ water solution and 100 mg/ml $NH_4NO_3$ water solution. Same experimental conditions as Fig. 3.5.

### 3.5.3 Cross section of $NO_3$ ion

The Remote Raman spectra of the $KNO_3$ and $NH_4NO_3$ water solutions (Fig. 3.7) are very similar to each other, as expected. They show Raman peaks corresponding to vibrations of the $NO_3^-$ ions. The main band corresponding to symmetrical stretching of the N-O bond appears at 1046.6 $cm^{-1}$. The differential Raman cross sections for this signal are 5.3 and $5.6 \cdot 10^{-30}$ $cm^2$ $sr^{-1}$ $molec^{-1}$, obtained from the spectrum of $KNO_3$ and $NH_4NO_3$ water solutions, respectively. Additional $NO_3^-$ ion Raman bands appear in the $NH_4NO_3$ solution spectrum at 716 and 1389 $cm^{-1}$ with $\upsilon_4$ and $\upsilon_3$ character, respectively (Rousseau et al., 1968). The slight differences in the peak positions (0.6 $cm^{-1}$) and cross sections are probably caused by different cation perturbations induced by the different $K^+$ and $NH_4^+$ ions also present in the solution (Dean and Wilkinson, 1985). The differential cross section provided by Dudik et al.

(1985) for the nitrate ion is 9.49 x $10^{-30}$ $cm^2$ $sr^{-1}$ $molec^{-1}$, corrected for the wavelength difference. The reasons for the small discrepancy are the same as for the differential Raman cross section of perchlorate, described previously.

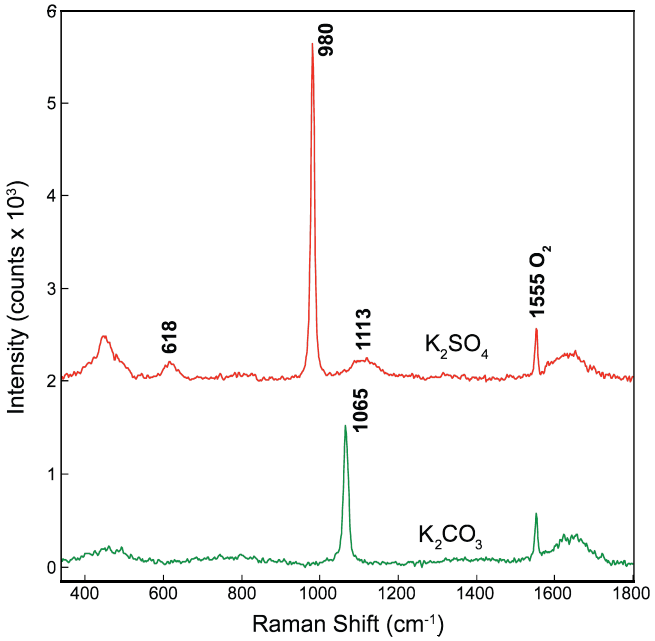


Figure 3.8: Remote Raman spectra of the 100 mg/ml $K_2CO_3$ water solution and 100 mg/ml $K_2SO_4$ water solution. Same experimental conditions as Fig. 3.5.

### 3.5.4 Cross section of $CO_3$ ion

The remote Raman spectrum of the $K_2CO_3$ water solution in (Fig. 3.8) shows its main Raman band at 1065 $cm^{-1}$, arising from the symmetrical stretch mode of oxygen in the $CO_3^{-2}$ ions (Bischoff et al., 1985). The obtained differential cross section value is 1.91 x $10^{-30}$ $cm^2$ $sr^{-1}$ $molec^{-1}$.

### 3.5.5 Cross section of $SO_4$ ion

Tthe 980 $cm^{-1}$ line in the $K_2SO_4$ water solution spectra (Fig. 3.8) corresponds to the symmetrical stretching mode of oxygen in the $SO_4^{2-}$ ions. The two additional sulfate peaks found at 618 and 1113 $cm^{-1}$ arise from internal antisymmetrical stretch vibrations, $\upsilon_4$ and $\upsilon_3$, respectively (Rull and Sobrón, 1994; White, 2009; Wiens et al., 2005). A cross section value of 4.96 x $10^{-30}$ $cm^2$ $sr^{-1}$ $molec^{-1}$ for the main 980 $cm^{-1}$ was obtained. As for the cases of the perchlorate and nitrate ions, the adjusted value provided by Dudik et al. (1985), 8.62 x $10^{-30}$ $cm^2$ $sr^{-1}$ $molec^{-1}$ is about a factor of two higher that the number obtained in this study. Despite the systematic higher values, likely caused by different laser wavelength used in their study,

the result of their study yielded the cross sections of the Raman symmetrical stretching lines of the perchlorate, nitrate, and sulfate ions with values within 15% of each other, in good agreement with the results in this study.

### 3.5.6 Cross section of $PO_4$ ion

The Raman spectra of the $Na_3PO_4 \cdot 12H_2O$ and the $Na_2[B_4O_5(OH)_4]\ 8H_2O$ water solutions (Fig 3.9) show low signal to noise ratio resulting from the low molar concentration of the phosphate and borate ions in the solutions, and not necessarily due to smaller cross sections of the measured Raman signals. The $Na_3PO_4 \cdot 12H_2O$ 100mg/ml water solution shows its main line at 937 $cm^{-1}$, the symmetrical stretching mode of the $PO_4^{-3}$ tetrahedral ion, consistent with previous studies (Pye and Rudolph, 2003). In this solution, the symmetrical stretching mode of $HPO_4^{-2}$ at around 987 $cm^{-1}$ is not observed coming from the reaction $PO_4^{3-} + H_2O \leftrightarrow HPO_4^{2-} + OH^-$ of the phosphate ion with water because of its low concentration (0.0862M). A value for the cross section of the symmetrical stretching mode of the $PO_4^{-3}$ tetrahedra of $3.35 \cdot 10^{-30}$ $cm^2$ $sr^{-1}$ $molec^{-1}$ was obtained.

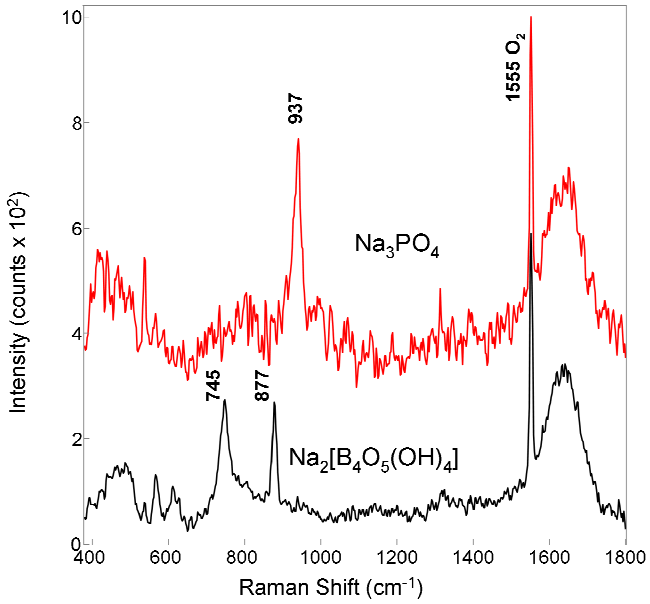


Figure 3.9: Remote Raman spectra of the 100 mg/ml $Na_3PO_4 \cdot 12H_2O$ 100 mg/ml water solution and 100 mg/ml $Na_2[B_4O_5(OH)_4] \cdot 8H_2O$ water solution. Average of five 150 pulses acquisitions, gain 250, 25 mJ/pulse.

### 3.5.7 Cross section of $BO_x$ ion

The remote Raman spectrum of the $Na_2[B_4O_5(OH)_4]$ $8H_2O$ 100 mg/ml water solution (Fig. 3.9) shows two main bands at 747 and 878 $cm^{-1}$ Raman shift. As sodium tetraborate enters water solution, the borate dissociates into $B_4O_7^- + 3H_2O \rightarrow 2H_3BO_3 + 2BO_2^-$ (Manov et al., 1944). The Raman bands observed are the symmetrical stretch of the $BO_2^{-2}$ ion in solution at 745 $cm^{-1}$ and the symmetrical stretch of the unbounded $BO_3^{-3}$ ion at 876 $cm^{-1}$ (Hibben, 1939). Therefore it is possible to calculate a cross section value for the $BO_2$ group and the orthoborate ion $BO_3^{-3}$, which is present in several borate minerals such as borax and kernite (Giese, 1966; Kalidasan et al., 2015). Thus, one obtains values of $6.79 \times 10^{-31}$ and $2.92 \times 10^{-31}$ $cm^2\ sr^{-1}\ molec^{-1}$ for the differential Raman cross sections of the $BO_2^{-2}$ and $BO_3^{-3}$ ions, respectively.

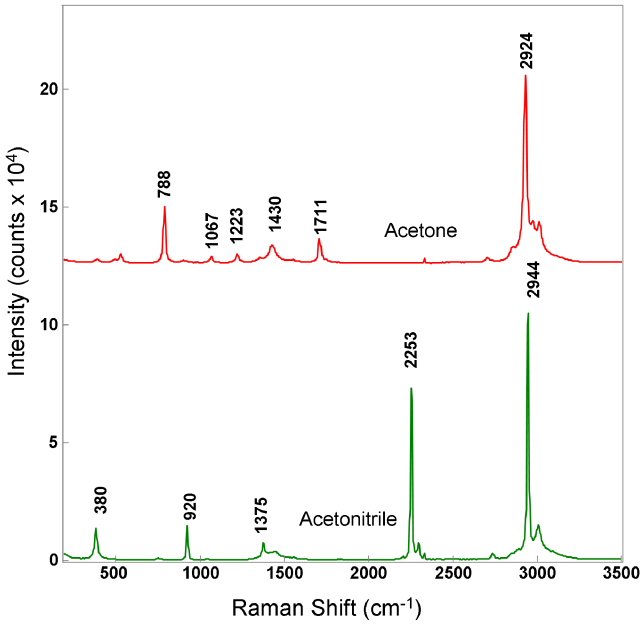


Figure 3.10: Remote Raman spectra of acetone and acetonitrile. Same experimental conditions as Fig. 3.5.

The measured Raman spectra of the organic liquids, and water are a perfect match with the Raman spectra of the corresponding chemical and most show a wealth of Raman signals in the fingerprint region. This study reports the Raman cross sections of the most intense or more distinct bands, as well as the cross section of some of the C-H, O-H, C-N, or C-Cl symmetrical stretching regions.

### 3.5.8 Cross section of acetone

The Raman spectrum of acetone (Fig. 3.10) shows the main band at 788 $cm^{-1}$ arising from C-C bond stretch vibrations (Shimanouchi, 1972) and gives a Raman cross section of $2.04 \times 10^{-30}$ $cm^2$ $sr^{-1}$ $molec^{-1}$, and the $CH_3$ group symmetrical stretch signal at 2926 $cm^{-1}$ (Shimanouchi, 1972) with a cross section value of $1.06 \times 10^{-29}$ $cm^2$ $sr^{-1}$ $molec^{-1}$.

### 3.5.9 Cross section of acetonitrile

In the Raman spectrum of acetonitrile (Fig. 3.10) three strong signals were selected at 920, 2253, and 2944 $cm^{-1}$ corresponding to C-C stretch, C-N stretch, and $CH_3$ symmetrical stretch vibrations, respectively. The obtained cross section values were $5.63 \times 10^{-31}$, $2.87 \times 10^{-30}$, and $4.20 \times 10^{-30}$ $cm^2$ $sr^{-1}$ $molec^{-1}$. The corrected literature values of Dudik et al. (1985) are $8.71 \times 10^{-31}$ and $7.16 \times 10^{-30}$ $cm^2$ $sr^{-1}$ $molec^{-1}$ for the 920 and 2253 $cm^{-1}$ signals with 514 nm excitation, in good agreement with the values from this study given the wavelength difference.

### 3.5.10 Cross section of methanol

In the Raman spectrum of methanol (Fig. 3.5) the C-O stretch line at 1033 $cm^{-1}$ and the broad C-H symmetrical and antisymmetrical stretch Raman signals in the C-H stretching region were selected. The latter is composed of two broad main signals. The integrated overall Raman intensity between 2650 and 3100 $cm^{-1}$ (Mammone et al., 1980) represents cross section values of $8.62 \times 10^{-31}$ and $6.36 \times 10^{-30}$ $cm^2$ $sr^{-1}$ $molec^{-1}$for the C-O stretch and C-H stretch lines, respectively.

### 3.5.11 Cross section of ethanol

In the ethanol Raman spectrum (Fig. 3.11) three regions were selected: the strong peak at 883 $cm^{-1}$ corresponding to C-C stretch vibrations; and the regions between 2780 and 3100, and 3130 and 3670 $cm^{-1}$, corresponding to $CH_3$ stretch and O-H stretch vibrations, respectively (Mammone et al., 1980; Yu et al., 2007). Thus, Raman cross section values of $9.67 \times 10^{-31}$ $cm^2$ $sr^{-1}$ $molec^{-1}$ for the 885 $cm^{-1}$ signal and $1.37 \times 10^{-29}$ and $2.37 \times 10^{-30}$ $cm^2$ $sr^{-1}$ $molec^{-1}$ for the $CH_3$ and O-H stretching lines, respectively were obtained.

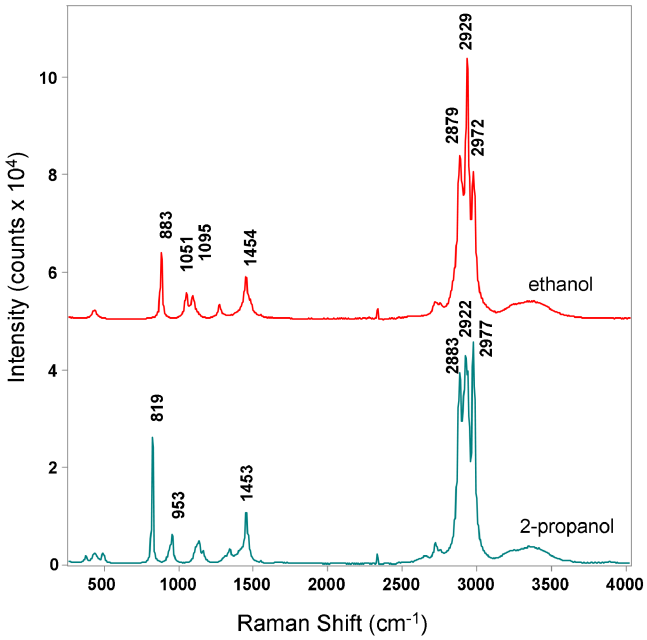


Figure 3.11: Remote Raman spectra of ethanol and 2-propanol. Same experimental conditions as Fig. 3.5.

### 3.5.12 Cross section of 2-propanol

Similarly, in the spectrum of 2-propanol (isopropanol) the strong C-C stretch band at 819 $cm^{-1}$ and two regions centered at 2921 and 3354 $cm^{-1}$ with signals arising from C-H and O-H stretch vibrations, respectively (Yu et al., 2014) were chosen. While processing this spectrum every peak was curve fitted to better separate C-H and O-H contributions. The centers listed as 2920 and 3354 $cm^{-1}$ are actually centers of mass as weighted by spectral area contribution. They are composed of 5+ large peaks corresponding to C-H stretch vibrations and two broad bands corresponding to O-H stretch vibrations. Values of $1.68 \times 10^{-30}$, $2.50 \times 10^{-29}$ and $5.22 \times 10^{-30}$ $cm^2$ $sr^{-1}$ $molec^{-1}$ as differential Raman cross section were obtained for each of the selected areas at 819, 2921, and 3354 $cm^{-1}$.

### 3.5.13 Cross section of dichloromethane.

For the dichloromethane spectrum, the cross sections were determined for the 703 $cm^{-1}$ $CCl_2$ symmetrical stretch peak, and the 2991 $cm^{-1}$ $CH_2$ symmetrical stretch peak as $4.40 \times 10^{-30}$ and $4.30 \times 10^{-30}$ $cm^2$ $sr^{-1}$ $molec^{-1}$, respectively (Shimanouchi, 1972).

### 3.5.14 Cross section of benzene

For the Raman spectrum of benzene (Fig. 3.12) along with the Raman spectrum of nitrobenzene the line at 993 $cm^{-1}$ was selected and the integrated spectral area between 2990 and 3150 $cm^{-1}$, correspond to the C-H ring stretching vibration and C-H stretch vibrations,

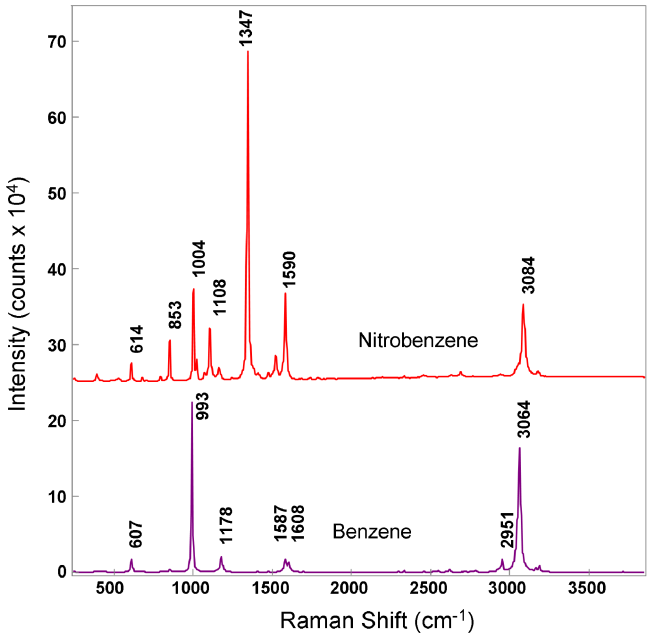


Figure 3.12: Remote Raman spectra of benzene and nitrobenzene. Same experimental conditions as Fig. 3.5.

respectively (Shimanouchi, 1972). Cross section values of 1.41 x $10^{-29}$ and 2.33 x $10^{-29}$ $cm^2$ $sr^{-1}$ $molec^{-1}$, respectively were obtained. Previous measurements by other authors of the 993 $cm^{-1}$ benzene peak cross sections yielded 2.67 x $10^{-29}$, 2.49 x $10^{-29}$, 2.35 x $10^{-29}$, 2.07 x $10^{-29}$ $cm^2$ $sr^{-1}$ $molec^{-1}$, as corrected from 514 nm laser excitation (Abe et al., 1977; Schomacker et al., 1986; Schrötter and Klöckner, 1979; Trulson and Mathies, 1986), and 0.834 x $10^{-29}$ $cm^2$ $sr^{-1}$ $molec^{-1}$, as corrected from 488 nm laser excitation (Skinner and Nilsen, 1968). All the literature values are of the same order as obtained in this study. The differences are probably the result from including a smaller peak at 983 $cm^{-1}$ in the calculations, different excitation lasers, and pulsed versus CW lasers, and measurement techniques. Stimulated Raman was also observed in Raman from benzene in other experiments (Fig. 5.11). Therefore, another possible explanation is that older measurements of the cross section of benzene might be affected by some contribution of stimulated Raman, which has a larger cross section.

Similarly, the corrected literature value of $3.95 \times 10^{-29}$ $cm^2$ $sr^{-1}$ $molec^{-1}$ for the 3060 $cm^{-1}$ line is within the order of the one reported here (McCreery, 2002).

### 3.5.15 Cross section of nitrobenzene

The C-N symmetrical stretch and the C-H stretch signals in the nitrobenzene spectrum located at 1347 and 3084 $cm^{-1}$, respectively (Clarkson and Ewen Smith, 2003) were selected and yielded $3.96 \times 10^{-29}$ and $2.04 \cdot 10^{-29}$ $cm^2$ $sr^{-1}$ $molec^{-1}$ for each of the signals. The cross section of the C-N symmetrical stretch line in liquid nitrobenzene was obtained by (Sakamoto et al., 1993) with a 488 nm laser. Correcting for 532 nm laser excitation, their value is $2.49 \times 10^{-29}$ $cm^2$ $sr^{-1}$ $molec^{-1}$, which is in reasonably good agreement with the result from this study.

### 3.5.16 Cross section of carbon tetrachloride

The 459 and 217 $cm^{-1}$ lines in the carbon tetrachloride spectrum correspond to symmetric stretch vibrations and symmetric degenerated deformation vibrations in the $CCl_4$ highly symmetric molecule (Shimanouchi, 1972). Thus, cross section values are $1.06 \times 10^{-29}$ and $6.39 \times 10^{-30}$ $cm^2$ $sr^{-1}$ $molec^{-1}$ for these two Raman signals. The cross section of the 459 $cm^{-1}$ line in a 90% solution of $CCl_4$ in $CS_2$, corrected from 488 nm laser excitation, is $7.95 \times 10^{-29}$ $cm^2$ $sr^{-1}$ $molec^{-1}$ (Yin et al., 2005). Their work suggests that the cross section is lower at full concentration, in good agreement with the result of this study.

### 3.5.17 Cross section of water

Finally, the measured spectrum of water (Fig. 5) shows all the expected Raman signals. The 456 $cm^{-1}$ librational mode of liquid water and the O-H stretching region curve fitted between 2700 and 3900 $cm^{-1}$. The O-H bending peaks are also visible in the spectrum at around 1630 $cm^{-1}$, as are lower frequency translational modes in the lower end of the measurement range (Carey and Korenowski, 1998). A cross section value of $1.67 \times 10^{-32}$ $cm^2$ $sr^{-1}$ $molec^{-1}$ for the 456 $cm^{-1}$ librational mode and $4.96 \times 10^{-30}$ $cm^2$ $sr^{-1}$ $molec^{-1}$ for the O-H stretching region were obtained. This latter value is in agreement with the values obtained and reviewed by Faris and Copeland (1997), approximately $5 \times 10^{-30}$ $cm^2$ $sr^{-1}$ $molec^{-1}$ for 532 nm laser excitation.

## 3.6 Conclusions

The Raman cross sections of various organic liquids and inorganic polyatomic ions determined in this study were obtained using remote Raman systems with a 532 nm pulsed laser. The laser excitation wavelength, type, and measurement geometry are similar to those

of the Raman systems in upcoming Mars planetary missions. The differential cross sections obtained in this study are in good agreement with literature values. Some values are a match with previous studies, which validates the methods and results used. The cross sections obtained especially agree with previous studies with 532 nm laser excitation (water) and with 532 nm pulse lasers (cyclohexane C-H), stressing the need to measure cross sections for particular wavelengths and geometries. The small discrepancies seem to result from different wavelength excitations and measurement geometries. The selected sample suite allows one to provide Raman cross section values for polyatomic ions of interest to planetary science. The presented Raman cross-section values will provide a baseline for the detection capabilities of the upcoming and future planetary Raman systems, as well as serve as a tool for the interpretation of the measured spectra.

# CHAPTER 4: REMOTE DETECTION OF AMINO ACIDS AND ORGANICS USING A COMPACT REMOTE RAMAN INSTRUMENT

## 4.1 Abstract

Sharp spectral Raman features are widely recognized to provide univocal and accurate chemical characterization of organic and inorganic compounds. Therefore Raman spectroscopy can be used to detect biological materials and biomarkers in the context of planetary exploration. Amino acids are of particular interest as they are the basic constituents of proteins and nucleic acids. A portable, compact time-resolved remote-Raman instrument is used it to demonstrate daytime detection of amino acids and nucleobases from a distance of 8 m. The measured spectra allowed to univocally identifying 20 proteinogenic amino acids, four nucleobases, and some non-proteinogenic amino acids, despite the presence of native fluorescence, especially in aromatic compounds. α and β amino acids could also be distinguish from each other, as well as different polymorphs. The used remote Raman system is well suited for planetary exploration applications, with no requirement for sample preparation or collection, and rapid measurement times.

## 4.2 Introduction

Water, water bearing minerals, organic compounds, and elements such as C, N, O, S, P, H, Fe, Mn, etc., are necessary for biological processes. The detection of these elements and compounds plays a significant role in NASA's search for past and present life in the Solar System.

The detection of biological materials and biomarkers is an important part of the NASA planetary exploration program (Mustard et al., 2013). Amino acids and nucleobases are of particular interest because they are essential for life as the basic constituents of proteins and nucleic acids. Amino acids have been reported in Martian meteorites. Callahan et al. (2013) reported extraterrestrial γ-amino-n-butyric acid (γ-ABA), β-alanine (β-ala), and glycine in the Martian shergottite RBT 04262. Glycine has also been reported in samples returned by NASA's Stardust spacecraft from comet 81 P/Wild 2 (Elsila et al., 2009). Among the amino acids found there are proteinogenic (e.g., L-alanine (L-ala) or L-Glutamic acid (L-glu)), and non-proteinogenic (e.g., β-aminoisobutyric acid, β-AIB). Recently, the Rosetta mission provided evidence of the presence of nonvolatile organic macromolecules on the surface of the comet 67P/Churyumov-Gerasimenko (Capaccioni et al., 2015). Amino acids and nucleobases are also found in other primitive Solar System materials, such as CM, CR, and CI carbonaceous chondrites (Botta et al., 2007; Callahan et al., 2011; Pearce and Pudritz,

2015), and have been studied as Titan chemical analogs (Khare et al., 1986; Neish et al., 2010).

Raman spectroscopy has been recognized as a powerful technique capable of identifying a large variety of chemicals, including: pure elements (e.g., carbon, silicon, and sulfur,); simple molecules (e.g., diatomic oxygen and nitrogen, water, carbon dioxide, etc.); inorganic chemicals (e.g., carbonates, oxides, perchlorates, nitrates, sulfates, etc.); organic compounds (e.g., polyaromatic hydrocarbons (PAHs), methane, and methane hydrates); biogenic compounds (e.g., amino acids, proteins, sugars, etc.); and rock forming minerals (calcite, gypsum, olivine, etc.). Raman spectra can be obtained from any state of aggregation (solid, liquid, and gas phase). Raman spectroscopy has been successfully used for the detection and characterization of amino acids and nucleobases (Jenkins et al., 2005; Otto et al., 1986), which demonstrates the potential of Raman spectroscopy for planetary exploration (Mustard et al., 2013).

### 4.3 Instrument description

A micro-Raman spectrometer could be mounted in the payload of a lander vehicle as a contact instrument, e.g., the RLS Raman spectrometer added onboard the ExoMars rover instrument suite for future ESA Mars exploration mission (Edwards et al., 2012; Lopez-Reyes et al., 2013). A remote system would save precious time and risky traverses. At the University of Hawai‘i, a compact, high throughput, portable remote Raman, fluorescence, and laser-induced breakdown spectroscopy (LIBS) system was developed with a 532 nm pulsed laser for planetary exploration under the Mars Instrument Development Program (Gasda et al., 2015; Misra et al., 2011). The compact time-resolved remote Raman, fluorescence and LIBS system (Fig. 4.1.) consists of: (1) a telescopic 500 mm Bower (F/8) camera lens as collection optics; (2) a custom made miniature spectrograph that occupies 1/14th the volume of a comparable commercial spectrograph from Kaiser Optical Systems Inc.; (3) a custom mini-ICCD detector from Syntronics LLC; and (4) a small frequency-doubled 532 nm Nd:YAG pulsed laser (Big Sky Laser - Ultra) with (5) a 10x beam expander. The system is completed with: (6) a 532 nm

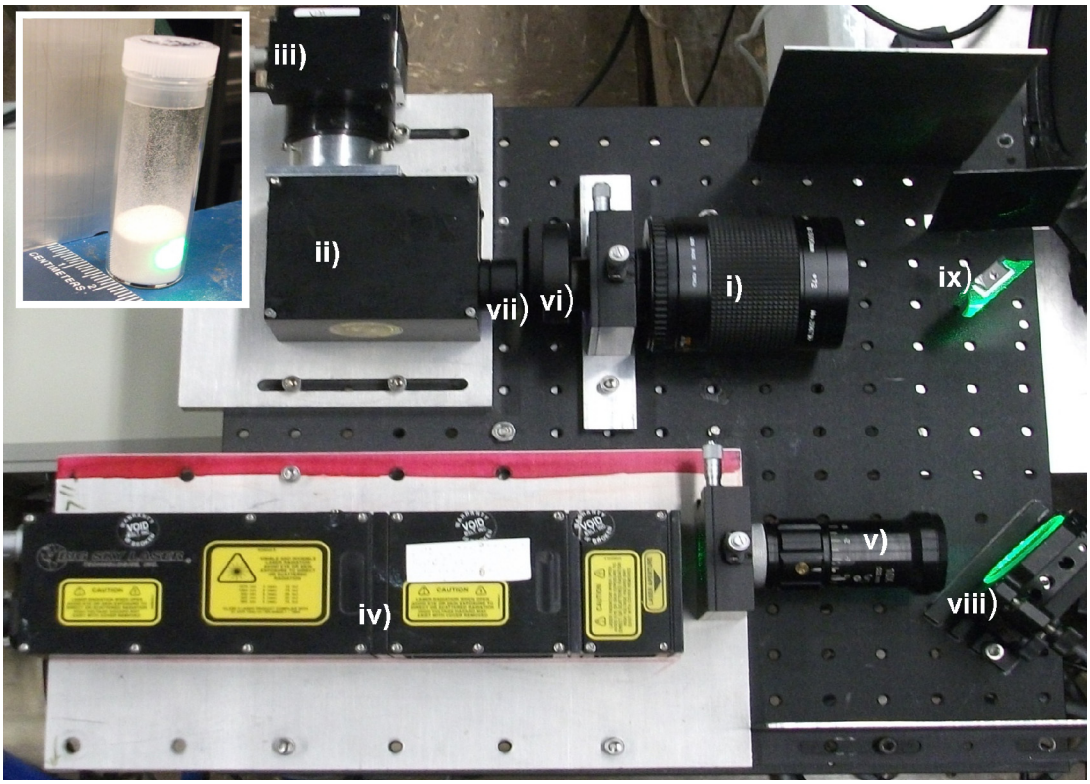


Figure 4.1: Portable remote Raman, fluorescence and LIBS system at the University of Hawai‘i. Inset shows the L-tryptophan being excited by the laser at 8 m distance (placed to the right of this image).

long pass filter (Semrock); (7) an optical coupling lens (f30 mm, F1.2); and (8) a front coated laser mirror and (9) a regular aluminum mirror acting as turning mirrors. The laser power is adjustable up to 30 mJ per pulse at 20 Hz. The beam expander allows varying the laser spot size at 10 m distance between ~300 μm and a few centimeters. The two turning mirrors make the system coaxial, with the Raman scattered signal measured by the backscattering geometry. The scattered signal is collected through the camera lens and focused in the 50 μm entrance slit of the spectrometer with the help of the coupling lens. The long pass filter between the camera lens and the coupling lens rejects intense 532 nm Rayleigh scattering coming from the sample. The system is mounted atop a Quickset pan and tilt mount and a utility cart, allowing it to aim samples in different directions. The ICCD detector, pan, and tilt mount are all controlled by a computer. The spectral images were acquired using custom software developed by HIGP software engineer Mr. Mark Wood, using the control software provided by the manufacturer as a starting point. In the remote Raman mode the system is

capable of measuring various minerals, water, ices, and atmospheric gases from a 50 m range with a 10 s integration time. At shorter distances of 10 m or less, good quality Raman spectra can be obtained within 1 s. The time-gated system is capable of detecting both the target mineral as well as the atmospheric gases before the target using their Raman fingerprints. Various materials can easily be identified through glass, plastic, and water media. The time-gating capability makes the system insensitive to an enclosing window material, which is highly desirable for future missions to Venus (where instruments are expected to be within the lander), and allows for time resolved spectroscopy. Using time resolution, luminescence can be minimized during Raman measurements and fluorescence life-time measurements can be performed as well. Inversely, the timing can be adjusted to measure the fluorescence, which can aid in the characterization of organics (Berlanga et al., 2015). The remote LIBS range is 10 m and LIBS spectra of various minerals can be obtained with single laser pulse excitation. The remote LIBS capability provides additional elemental verification of the targeted material (Gasda et al., 2015).

### 4.4 Samples and methodology

The measured samples were all of the proteinogenic amino acids (21 L-amino acids and glycine kit, Fluka, Sigma-Aldrich), some non-proteinogenic amino acids such as 2-aminoisobutyric acid, sarcosine, and five nucleobases (purchased from Sigma) along with several polyaromatic hydrocarbons, such as anthracene. Samples were placed and measured inside glass vials. Glass has a significantly lower Raman cross-section compared with of organics and amino acids. Remote Raman measurements were recorded from 8 m distance with 200 laser pulses excitation (10 s at 20 Hz) using a 10 mJ/pulse laser power output, and an approximately 8 mm laser spot on the target. The delay of the gated ICCD camera was adjusted at -400 ns to pre-trigger the camera at the arrival of the Raman signal, with a 400 ns camera gate width. Because the ICCD is only exposed for 0.84 μs the Raman signal is easily measured in well lit environments. The mini-ICCD detector was operated using our custom software and spectra were wavelength and intensity calibrated using UH-Raman LIBS v.1.61 software. Raman spectra shown in Figures 4.4 through 4.7 were baseline corrected using the commercial software Grams/AI 7.02.

## 4.5 Results

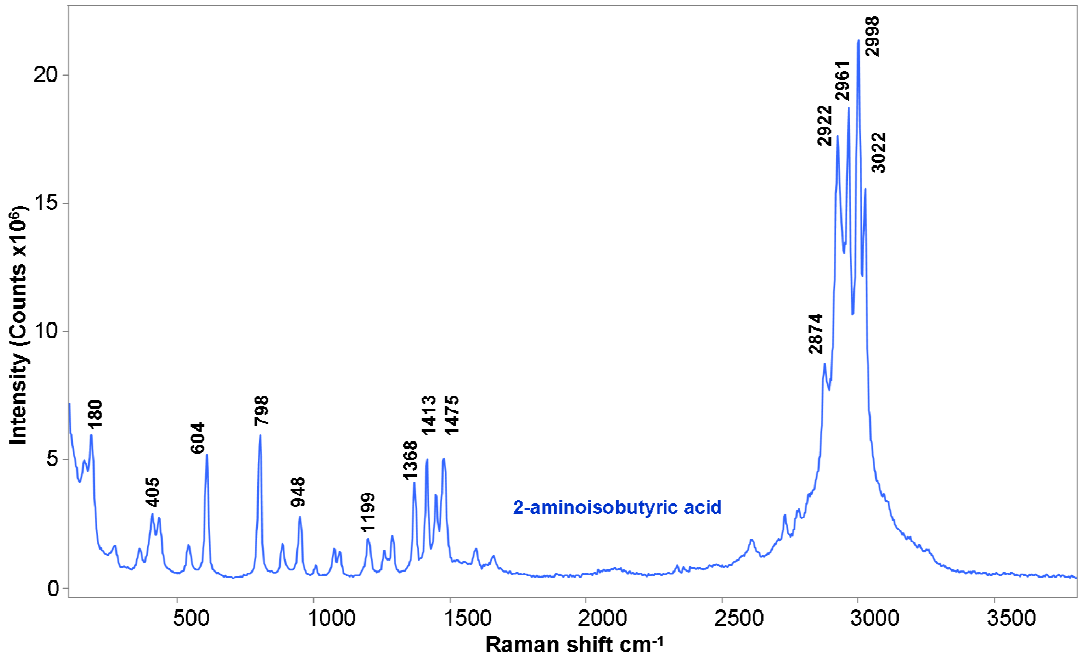


Figure 4.2: Raman spectrum of the non-proteinogenic amino acid 2-aminoisobutyric acid. Integrated over 200 laser pulses, 30 mJ/pulse, at 10 m range.

The Raman spectrum of the non-proteinogenic amino acid 2-aminoisobutyric acid illustrates the ability of the miniature spectrometer to measure the entire spectrum in one single acquisition (Fig. 4.2). The Raman spectra of five nucleobases fall in the ranges 300 to 1800 $cm^{-1}$ (the Raman fingerprint region) and 2800 to 3400 $cm^{-1}$ (C-H stretching region) (Fig. 4.3). Most of the nucleobases are easily detectable, with the exception of guanine, because of a large fluorescence background. A faster laser pulse and optical detector could help separate the Raman signal from fluorescence in the time domain.

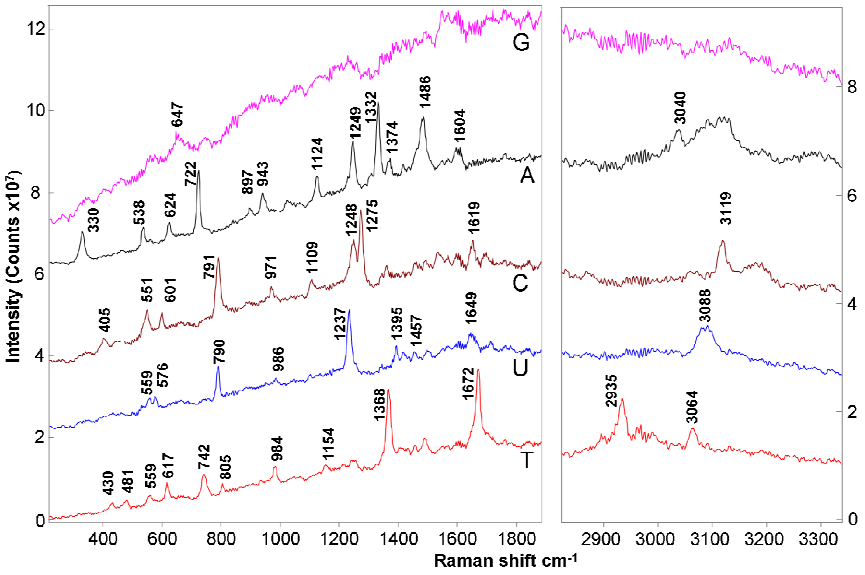


Figure 4.3: Raman spectra of adenine (A), guanine (G), thymine (T), cytosine (C) and uracil (U). Integrated over 200 laser pulses, 30 mJ/pulse, at 10 m range. Spectra are vertically shifted for clarity.

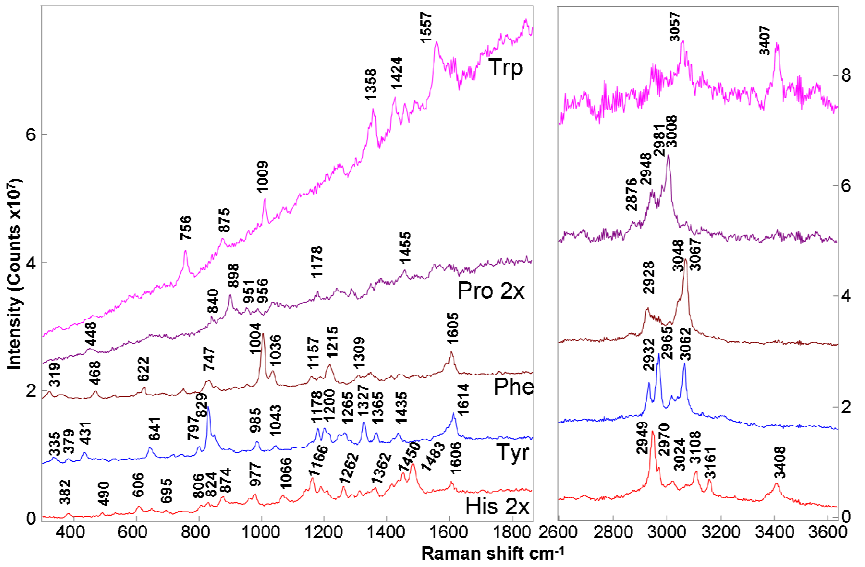


Figure 4.4: Raman spectra of aminoacids with aromatic rings L-phenylalanine (Phe), L-tyrosine (Tyr), L-tryptophan (Trp), L-histidine (His) and L-proline (Pro). Integrated over 200 laser pulses, 30 mJ/pulse, at 10 m range. Histidine and proline spectra have been scaled for clarity.

(Blacksberg et al., 2016). The Raman spectra of 14 proteinogenic amino acids and β-alanine were measured in the ranges 300 to 1800 $cm^{-1}$, and 2600-3600 $cm^{-1}$ (C-H stretching) (Fig. 4.4 through 4.8). The measured Raman peaks of the 20 proteinogenic amino acids along with their relative intensities were listed (Tables 4.1 through 4.5); as well as the the Raman shifts and assignments for the most prominent fingerprint Raman bands detected in the remote Raman spectra of the 20 standard amino acids (Table 4.6). The majority of the Raman bands in the Raman fingerprint region arise from CH, $CH_2$, and $CH_3$ deformation vibrational modes. The range between 2600 and 3600 $cm^{-1}$ shows bands that result from C–H stretching, aromatic C-H stretching, $NH_2$ stretching, and O-H stretching, and that are about four times more intense than the strongest bands in the fingerprint region. The bands in the range 2600 to 3000 $cm^{-1}$correspond to C-H stretch vibrations. The aromatic C-H stretch vibrations appear in the region from 3000 to 3100 $cm^{-1}$ (Fig. 4.4). The stretch vibrations of $NH_2$ are observable in primary amines (Arg, His, Lys, Fig. 4.5) from 3330 to 3400 $cm^{-1}$. The heterocyclic ring structure of histidine, an α-amino acid, can be characterized by two sharp bands at 3109 and 3160 $cm^{-1}$ (Brulé et al., 2014; Culka et al., 2010; Du et al., 2014; Movasaghi et al., 2007; Sjöberg et al., 2014; Zhu et al., 2011).

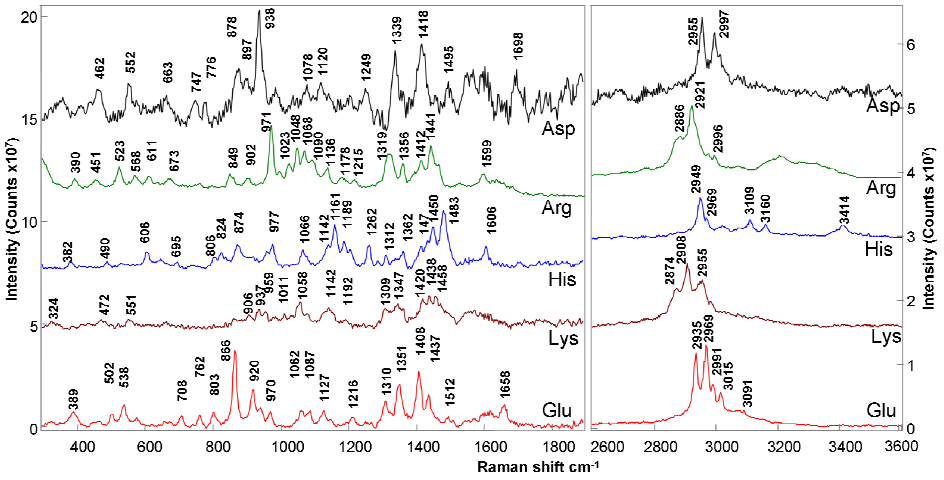


Figure 4.5: Raman spectra of amino acids with electrically charged side chains. L-aspartic acid (Asp), L-arginine (Arg), L-lysine (Lys), L-glutamic acid (Glu) and L-histidine (His). Integrated over 200 laser pulses, 30 mJ/pulse, at 8 meter range. Right hand box in the figure shows the same spectra in the C-H stretching and O-H stretching region. Spectra are baseline corrected and vertically shifted for clarity.

Table 4.1: Peak positions and relative intensities measured in the spectra of amino acids with aromatic rings.

| **Trp*** | **RI** | **Pro** | **RI** | **Phe** | RI | **Tyr** | | **His** | **RI** |
|---|---|---|---|---|---|---|---|---|---|
| | | | | | | 158.9 | vw | 158.3 | m |
| | | | | | | | | 191.5 | w |
| | | | | | | 253.9 | vw | 267.2 | m |
| | | | | 319.0 | w | 310.4 | vw | 295.2 | vw |
| | | | | | | 335.4 | vw | | |
| | | | | 362.9 | w | 379.1 | vw | 382.1 | m |
| | | | | 413.7 | vw | 431.2 | w | | |
| | | 448.2 | w | 468.5 | w | 472.5 | vw | 490.3 | w |
| | | | | | | 491.4 | vw | | |
| | | | | 525.9 | vw | 526.1 | vw | 530.7 | w |
| | | | | 605.5 | vw | | | 606.2 | m |
| | | 641.2 | vw, sh | 621.9 | w | 641.3 | w | 649.8 | vw,d |
| | | 694.5 | vw | 683.1 | vw | | | | |
| | | | | | | 714.4 | vw | 694.6 | w |
| 755.9 | m | | | 747.5 | w | 741.9 | vw | | |
| | | | | 786.3 | vw | 797.5 | w | 805.7 | w |
| | | | | 820.7 | m | **829.1** | **vs** | 824.3 | w,sh |
| | | 841.6 | w | 833.2 | m | 845.9 | m | | |
| 874.6 | w | | | | | 879.5 | m | 874.3 | m |
| | | **898.2** | **s** | | | 896.5 | vw | | |
| | | 919.2 | w | 913.8 | vw | | | 915.5 | w |
| | | 951.4 | vw | 951.6 | vw | | | 960.7 | w |
| | | 984.4 | vw | | | 984.7 | w | 977.4 | m |
| **1009.0** | **s** | | | **1004.3** | **vs** | | | | |
| | | 1033.0 | w | | | | | | |
| | | 1056.5 | w | | | 1043.4 | w | 1065.5 | w |
| | | 1082.2 | vw | | | 1098.3 | vw | 1079.4 | vw |
| | | | | | | 1113.8 | vw | | |
| | | | | 1036.0 | m | 1154.6 | vw | 1141.7 | w |
| | | | | 1157.3 | w | 1161.9 | vw | **1161.4** | s |
| | | 1174.6 | w | 1184.8 | w | 1178.3 | m | 1189.5 | w |
| | | | | | | 1200.1 | m | | |
| | | | | 1214.9 | m | 1213.5 | w | 1207.1 | w |
| | | 1237.7 | w | | | 1247.3 | w | | |
| | | 1264.3 | vw | | | 1265.1 | m | 1262.0 | m |
| | | 1285.8 | vw | 1308.2 | w | 1282.9 | vw | | |
| 1336.3 | w | 1349.9 | vw | 1340.3 | w | **1326.8** | **vs** | 1312.2 | m |
| **1358.3** | **s** | 1374.1 | w | 1353.2 | w | 1364.5 | m | 1360.3 | w |
| | | | | 1411.1 | vw | 1419.2 | w | 1417.2 | vw |
| 1423.7 | m | | | 1438.1 | vw | 1433.9 | m | 1432.7 | vw |
| 1457.9 | vw | 1450.8 | w | 1446.8 | vw | 1518.8 | vw | 1449.9 | m |
| | | | | | | | | **1482.8** | **s** |
| 1557.2 | m | | | | | | | | |
| 1575.8 | w | | | 1587.1 | w | 1590.0 | vw | | |
| | | | | 1605.0 | m,d | 1602.3 | vw | | |
| | | | | | | 1613.9 | m | | |
| | | | | | | | | | |
| | | | | 2864.5 | w | 2931.7 | m | 2949.1 | vs |
| | | 2948.4 | m, sh | 2928.4 | m | 2965.3 | vs,d | 2971.3 | w |
| | | 2984.5 | w | 2969.1 | w | 3015.7 | w | 3023.4 | w |
| 3057.0 | s | 3006.4 | s | 3047.6 | m | 3040.9 | w | 3109.99 | s |
| | m | | | 3067.0 | vs,d | 3062.3 | s | 3160.3 | s |
| 3407.0 | | | | | | 3210.5 | w | 3408.3 | w |

*Trp has the strongest fluorescence in the Raman spectra excited with 532 nm laser (see Fig. 4.4)
Abbreviations: doublet or multiple unresolved lines (d); shoulder (sh); very weak (vw); weak (w); medium (m); strong (s); very strong (vs). Trp = trypthophan; Pro = proline; Phe = phenylalanine; Tyr = tyrosine; His = histidine

Table 4.2:Peak positions and relative intensities measured in the spectra of amino acids with electrically charged side chains. Histidine is listed in table 4.1 as it is also an aromatic amino acid.

| **Glu** | | **Lys** | | **Arg** | | **Asp** | |
|---|---|---|---|---|---|---|---|
| | | | | | | 187.9 | Vw |
| | | | | **290.2** | **s** | 272.1 | w |
| 388.6 | m | 324.6 | w | 388.2 | vw | 357.3 | w |
| | | | | 420.0 | vw | | |
| | | 471.8 | vw | 452.7 | vw | 467.4 | w |
| 502.2 | w | | | | | | |
| **538.4** | **s** | | | 523.2 | w | | |
| 577.4 | w | 545.5 | m | 569.1 | vw | 551.7 | w |
| | | | | 607.6 | w | 599.1 | vw |
| | | | | 665.1 | vw | | |
| 708.5 | w | | | | | 747.3 | vw |
| 762.2 | w | | | 758.7 | vw | 777.7 | w |
| 802.6 | w | | | | | | |
| | | | | 847.7 | m, sh | | |
| **866.5** | **vs** | 858.7 | m | 856.8 | vw | 871.6 | w |
| **919.9** | **s** | 903.5 | m | 900.2 | vw | 901.2 | vw |
| 942.1 | w | 936.6 | m | | | **937.2** | **vs** |
| 969.7 | w | 957.9 | w | **970.0** | **vs** | | |
| | | | | 996.0 | w | 990.3 | vw |
| | | 1006.8 | w | 1021.4 | w | | |
| | | 1034.8 | vw | 1046.3 | m | | |
| 1062.3 | w | **1054.1** | **s** | 1068.8 | w | | |
| 1087.2 | sh,w | 1079.2 | w | 1090.8 | w,d | 1081.6 | w |
| 1127.5 | w | | | | | | |
| 1149.2 | vw | 1143.5 | d | 1134.8 | w | 1119.3 | vw |
| | | | | 1174.8 | vw,d | | |
| 1215.9 | vw | | | 1215.2 | w,d | | |
| | | | | 1286.1 | vw | 1256.3 | vw |
| 1310.2 | w | **1309.4** | **vs,d** | 1319.7 | m,d | | |
| | | | | | | 1335.8 | m |
| **1351.4** | **s** | 1349.5 | d | 1358.3 | m | 1359.8 | vw |
| **1407.7** | **s** | 1420.5 | vw | 1411.2 | m | 1418.3 | w |
| 1437.4 | w | **1441.2** | **s** | 1440.3 | m | | |
| | | **1458.9** | **s,d** | 1464.7 | w | | |
| 1512.4 | vw | | | 1525.9 | vw | | |
| | | | | 1595.7 | w | | |
| | | | | 1628.7 | vw | | |
| 1658.4 | w | | | | | 1691.4 | vw |
| | | | | | | | |
| | | 2869.7 | m | 2770.8 | vw | | |
| | | | | 2880.8 | s | | |
| | | 2912.8 | vs | 2919.7 | vs | | |
| 2935.1 | vs | | | 2932.6 | m | | |
| 2971.7 | vs | 2959.3 | m | | | 2955.8 | vs |
| | | | | 2973.3 | w | | |
| 2992.3 | m | | | 2997.4 | m | 2996.5 | s |
| 3017.3 | w | | | | | 3014.6 | w |
| | | | | 3205.8 | w | | |

Abbreviations: doublet or multiple unresolved lines (d); shoulder (sh); very weak (vw); weak (w); medium (m); strong (s); very strong (vs). Glu = glutamic acid; Lys = lysine; Arg = arginine; and Asp = aspartic acid.

Table 4.3: Peak positions ($cm^{-1}$) and relative intensities (RI) measured in the spectra of amino acids with polar uncharged side-chains.

| **Gln** | | **Thr** | | **Ser** | | **Asn** | |
|---|---|---|---|---|---|---|---|
| 344.3 | w | 337.1 | vw | | | 335.8 | w, d |
| | | 383.8 | vw | | | 374.2 | vw |
| | | 419.2 | vw | | | 408.1 | vw |
| 453.6 | m | 446.5 | w | | | 450.2 | vw |
| | | | | 513.4 | m | 520.0 | vw |
| 543.0 | sh,w | | | | | 540.3 | w |
| | | **563.5** | **s** | | | 582.0 | vw |
| 623.8 | m | | | 609.4 | m | 606.5 | vw,d |
| 653.8 | vw | | | | | 662.0 | vw |
| | | 701.9 | vw | | | | |
| | | 743.2 | vw | | | 753.7 | w, d |
| 777.5 | w | | | | | 798.1 | w |
| | | | | 813.5 | m | 837.1 | w, d |
| **849.4** | **vs** | 871.9 | s | **852.4** | **s** | 877.8 | vw |
| | | | | | | 894.3 | vw |
| **896.9** | **s** | 903.2 | vw | 921.5 | w | 910.7 | vw |
| 925.9 | vw | 930.8 | s | | | **940.6** | **s** |
| | | | | 967.9 | w | 986.0 | vw |
| 1000.6 | w | | | 1007.6 | m | 1002.3 | vw |
| 1052.4 | m | 1041.8 | w,sh | 1090 | vw | 1072.6 | m |
| **1097.4** | **s** | 1195.1 | w | | | | |
| 1134.6 | w | **1114.4** | **s. sh** | 1131.3 | vw,d | 1107.2 | vw |
| 1165.3 | m | | | | | 1153.0 | m, d |
| 1204.9 | vw | | | 1219.6 | vw,d | 1235.2 | w |
| 1284.9 | w | | | | | 1262.9 | vw |
| 1308.7 | m | 1305.9 | vw | 1298.5 | w | | |
| **1331.2** | **s** | **1340.0** | **vs** | **1324.9** | **vs** | **1330.6** | **s** |
| 1357.7 | w | | | | | 1358.6 | m |
| **1418.5** | **s** | 1417.4 | w | 1414.9 | w,d | **1417.0** | **vs** |
| 1450.1 | m | 1451.1 | w | 1461.7 | m | 1497.0 | vw |
| 1498.4 | w | | | | | | |
| 1551.0 | vw | 1548.0 | vw | | | 1560.9 | vw |
| 1605.0 | m | 1598.3 | vw | | | | |
| 1623.1 | w | | | | | 1621.8 | w,sh |
| 1647.1 | w | 1639.1 | vw | | | | |
| 1688.3 | m | | | | | | |
| | | | | | | | |
| 2817.0 | vw | 2878.5 | vs | | | | |
| 2902.0 | vw | | | 2904.9 | w | | |
| 2932.7 | vs | 2940.4 | s, sh | | | 2941.9 | vs,sh |
| 2959.1 | vs | 2977.4 | m | 2960.8 | vs | 2965.7 | s |
| 2990.3 | w | 2996.8 | m | | | 2976.3 | vs |
| | | 3021.6 | s | 2998.2 | m | | |
| 3180 3220 | m | | | | | 3070-3790 | w |
| | | | | | | 3347.3 | m |
| 3407.0 | w | | | | | 3391.0 | s |

Abbreviations: doublet or multiple unresolved lines (d); shoulder (sh); very weak (vw); weak (w); medium (m); strong (s); very strong (vs). Gln = glutamine; Thr = threonine; Ser = serine; and Asn = asparagine.

Table 4.4: Peak positions ($cm^{-1}$) and relative intensities (RI) measured in the spectra of the amino acids L-methionine (Met), L-leucine (Leu), L-isoleucine (Ile), and L-valine (Val).

| **Val** | | **Ile** | | **Leu** | | **Met** | |
|---|---|---|---|---|---|---|---|
| 332.7 | w | 364.0 | w | 348.0 | vw | 337.5 | w |
| | | 388.1 | vw | | | 352.8 | w |
| | | 422.0 | vw | 402.6 | vw | 419.4 | vw |
| | | 489.4 | vw | 457.3 | m | | |
| **541.7** | **vs** | 536.8 | m | 534.0 | m | 543.4 | m |
| | | 556.4 | w | | | | |
| 664.4 | w | 675.8 | w | 669.8 | w | 644.4 | w |
| | | 710.2 | w | | | 681.8 | w |
| 753.3 | w,d | 749.5 | m | | | **720.4** | **vs** |
| 776.2 | m | 768.9 | w | 773.4 | vw | 763.2 | m |
| | | 801.6 | vw | | | 803.4 | w |
| 824.3 | w | 825.5 | w | **835.9** | **s** | | |
| 849.5 | m | 852.5 | w | 846.9 | vw | | |
| | | 872.7 | vw | | | 874.2 | m |
| 902.2 | vw | 922.6 | m | 923.9 | m | | |
| **948.3** | **s** | | | 944.7 | w | 952.8 | w |
| 964.4 | w | 964.4 | vw | 963.5 | w | | |
| | | 993.1 | m | 1003.6 | vw | 986.4 | vw |
| 1028.5 | vw | 1033.1 | m,sh | 1030.2 | w | | |
| 1066.1 | vw | 1090.7 | w | 1082.0 | m | | |
| 1124.9 | w | 1137.8 | vw | 1129.7 | m | | |
| 1185.8 | vw,d | 1189.0 | vw | 1180.1 | m,d | 1173.0 | w,d |
| | | | | 1239.6 | vw | 1244.1 | w |
| 1271.9 | w | | | 1297.3 | w | | |
| | | 1309.6 | vw | 1314.5 | w | 1320.3 | m |
| 1330.6 | w,d | **1328.2** | **s** | **1340.6** | **vs,sh** | 1332.0 | w |
| 1351.5 | m,d | **1355.0** | **s,sh** | | | 1352.5 | m |
| 1397.6 | w,d | 1396.6 | m | | | | |
| | | 1418.6 | vw | 1408.1 | m,d | 1412.5 | m |
| 1427.0 | w | | | | | 1425.6 | m |
| **1452.6** | **s,sh** | **1447.6** | **vs,sh** | **1455.1** | **vs, sh** | **1447.3** | **s** |
| 1509.9 | w | 1513.9 | vw | 1512.3 | vw | | |
| | | | | 1557.1 | vw | | |
| | | | | 1584.4 | vw | | |
| 1636.3 | w | | | 1625.0 | w | | |
| | | | | | | | |
| | | | | 2718.0 | vw | | |
| | | | | 2767.5 | vw | | |
| 2880.7 | w | | | | | 2855.8 | vw |
| | | 2881.2 | s | 2875.5 | s,d | 2880.9 | w |
| 2909.8 | vs | 2891.7 | vs | 2901.5 | vs | 2916.0 | vs |
| 2946.1 | m | 2949.1 | s, d | 2935.9 | s,d | 2936.9 | m |
| | | | | 2960.5 | m | | |
| 2969.9 | vs | | | 2967.8 | s | 2972.0 | w,d |
| 2995.3 | w,d | 2993.5 | w | 2986.3 | m | | |

Abbreviations: doublet or multiple unresolved lines (d); shoulder (sh); very weak (vw); weak (w); medium (m); strong (s); very strong (vs).

Table 4.5: Peak positions ($cm^{-1}$) and relative intensities (RI) measured in the spectra of the amino acids L-glycine (Gly), L-cysteine (Cys), and L-α-alanine (Ala).

| **Gly** | | **Cys** | | **Ala** | |
|---|---|---|---|---|---|
| | | | | 159.2 | vw |
| | | | | 192.9 | vw |
| | | | | 265.8 | vw |
| | | | | 283.7 | vw, sh |
| 356.8 | vw | 364.3 | vw | 323.1 | vw |
| | | | | 398.5 | w, sh |
| | | 443.2 | m | | |
| 503.3 | m | | | | |
| 558.8 | vw | 536.0 | w | 531.8 | w |
| 606.0 | vw | **639.4** | **vs** | | |
| 685.1 | w | 692.3 | w | 652.3 | vw |
| | | 772.9 | w | 772.6 | vw |
| | | 806.6 | vw | | |
| | | 822.6 | w | | |
| **892.7** | **vs** | 868.4 | w | **851.2** | **vs** |
| 928.7 | vw | 940.9 | w | 920.7 | vw |
| | | 1006.3 | vw | | |
| 1048.0 | w | 1066.7 | w | 1019.9 | w |
| | | 1109.2 | vw | 1112.7 | w |
| 1155.1 | vw | 1140.4 | vw | 1146.9 | vw |
| | | 1199.6 | w | | |
| | | 1269.4 | vw | 1236.9 | vw |
| 1323.1 | m | 1294.0 | w | 1305.4 | m |
| 1336.5 | m | 1344.9 | m | 1358.7 | m |
| 1395.7 | m,sh | 1398.5 | w | 1409.0 | w |
| 1438.4 | m | 1424.9 | m | 1461.4 | m |
| | | | | 1482.2 | m |
| | | | | 1498.7 | vw |
| 1501.9 | vw | 1525.5 | vw | | |
| 1576.7 | vw | 1575.0 | vw | 1596.3 | w |
| 1674.2 | vw | | | | |
| | | **2550.7** | **vs** | | |
| | | | | 2606.4 | vw |
| | | | | 2735.7 | vw |
| 2863.7 | vw | | | 2881.3 | m |
| | | | | 2934.8 | m |
| 2963.6 | vs,d | 2958.2 | s | 2966.4 | vs |
| | | | | 2987.2 | m |
| 2999.4 | m | 2998.6 | w | 3001.1 | s |
| 3103.6 | vw | | | 3080.1 | vw |

Abbreviations: doublet or multiple unresolved lines (d); shoulder (sh); very weak (vw); weak (w); medium (m); strong (s); very strong (vs).

Table 4.6: Raman shifts and assignments for prominent fingerprint Raman bands detected in the remote Raman spectra of the 20 standard amino acids.

| Amino acid | Raman shift ($cm^{-1}$) | Assignment |
|---|---|---|
| **Amino acids with aromatic rings** | | |
| Trp | 1009.0 s | Ring breathing (1) |
| | 1358.3 s | $CH_2$ wagging (1) |
| Pro | 898.2 s | Ring breathing (5) |
| Phe | 1004.3 vs | Ring breathing (1) |
| Tyr | 829.1vs | Ring breathing + Fermi res.(1) |
| | 1326.8 vs | C-C antissym. ring stretching (3) |
| His | 1161.4 s | C-N stretching (3) |
| | 1482.8 s | C-N-C stretching (3) |
| **Amino acids with electrically charged side-chains** | | |
| Amino acid | Raman shift ($cm^{-1}$) | Assignment |
| Glu | 538.4 s | |
| | 866.5 vs | COOH deformation (1) |
| | 919.9 s | C–C–N stretching (1) |
| | 1351.4 s | N-C-H sym. stretching (4) |
| | 1407.7 s | COO– sym. stretching (1) |
| Lys | 1054.1 s | C-N stretching$_{(amino\ side)}$ (3) |
| | 1309.4 vs | C-C stretching (3) |
| | 1441.2 s | $CH_2$ scissors (3) |
| | 1458.9 s | $CH_2$ scissors (3) |
| Arg | 290.2 s | Lattice mode |
| | 970.0 vs | C-C stretching (4) |
| Asp | 937.2 vs | out-of-plane bending vibration of the UH group from the carboxylic acid group (1) |
| **Amino acids with polar uncharged side-chains** | | |
| Amino acid | Raman shift ($cm^{-1}$) | Assignment |
| Gln | 849.4 vs | ν(CC) stretching (1) |
| | 896.9 s | ν(CC) stretching (6) |
| | 1097.4 s | ν(CN) sym. stretching (1) |
| | 1331.2 s | CH deformation (1) |
| | 1418.5 s | C-O stretching (6) |
| Thr | 563.5s | Rocking $CO_2^-$ (1) |
| | 1114.4 s | $NH_3$ rocking (1) |
| | 1340.0 vs | C-H derfomation (1) |
| Ser | 852.4 s | ν(CCN) sym. stretching (1) |
| | 1324.9 vs | C-O stretching (7) |
| Asn | 940.6 s | C-C stretching (1) |
| | 1330.6 s | C-N deformation (1) |
| | 1417.0 vs | C-N stretching (1) |
| **Amino acids with hydrophobic side-chains** | | |
| Amino acid | Raman shift ($cm^{-1}$) | Assignment |
| Val | 541.7 vs | $CO_2$ rocking (4) |
| | 948.3 s | C-C stretching |
| | 1452.6 s | $CH_3$ asym. deformation (4) |
| Ile | 1328.2 s | H-C-C wagging (4) |
| | 1355.0 s | COO sym. stretching (4) |
| | 1447.6 vs | Cγ asym. rocking (4) |
| Leu | 835.9 s | C-C sym. stretching (3) |
| | 1340.6 vs | C-C stretching (3) |
| | 1455.1 vs | $CH_3$ scissors (3) |
| Met | 720.4 vs | C-S stretching (1) |
| | 1447.3 s | $CH_2$, $CH_3$ scissors (3) |
| Ala | 851.2 vs | ν(CCN) sym. stretching (1) |
| **Other amino acids** | | |
| Amino acid | Raman shift ($cm^{-1}$) | Assignment |
| Gly | 892.7 vs | ν(CCN) sym. stretching (3) |
| | 1323.1 m | $CH_2$ wagging (3) |
| Cys | 639.4 vs | $COO^-$ wagging (2) |
| | 2550.7 vs | S-H stretching (4) |

References: (1) Culka et al., 2010; (2) Brulé et al., 2014; (3) Sjöberg et al., 2014; (4) Zhu el al., 2011; (5) Mary et al., 2009; (6) Baran et al., 2007; and (7) Murli et al., 2006. Abbreviations: Ala = α-alanine; Arg = arginine; Asn = asparagine; Asp = aspartic acid; Cys = cysteine; Glu = glutamic acid; Gln = glutamine; Gly = glycine; His = histidine; Ile = isoleucine; Lys = lysine; Leu = leucine; Met = methionine; Phe = phenylalanine; Pro = proline; Ser = serine; Thr = threonine; Trp = trypthophan; Tyr = tyrosine; and Val = valine.

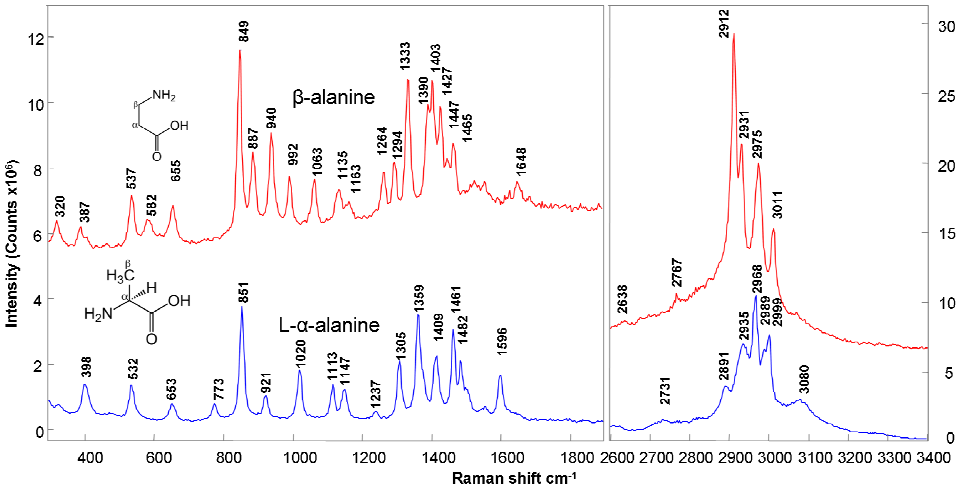


Figure 4.6: Raman spectra of the non-polar simple amino acids L-α-alanine and β-alanine. L-α-alanine is second to L-leucine in biological occurrence, in β-alanine the amino group is at the β-position from the carboxylate group. Right hand box in the figure shows the same spectra in the C-H stretching region. Integrated over 200 laser pulses, 30 mJ/pulse, at 8 meter range. Spectra are baseline corrected and vertically shifted for clarity.

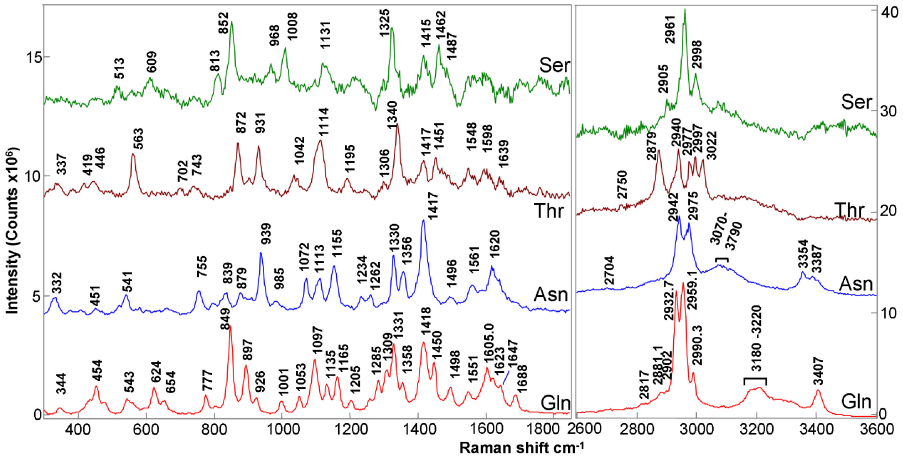


Figure 4.7: Raman spectra of amino acids with polar uncharged side chains. L-glutamine (Gln), L-asparagine (Asn), L-threonine (Thr), and L-serine (Ser). Integrated over 200 laser pulses, 30 mJ/pulse, at 8 meter range. Right hand plot in the figure shows the same spectra in the C-H stretching and O-H stretching region. Spectra are baseline corrected and vertically shifted for clarity.

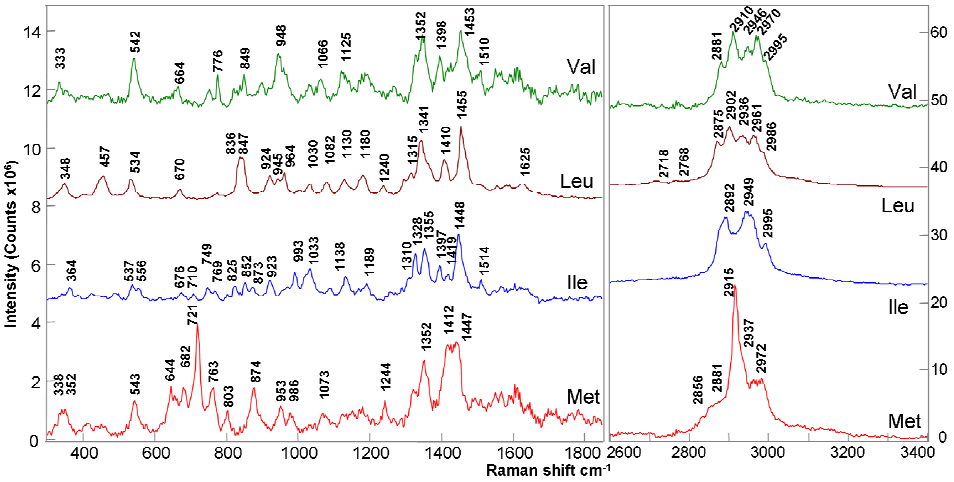


Figure 4.8: Raman spectra of amino acids in the ranges 300 - 1850 and 2600 – 3400 $cm^{-1}$. L-methionine (Met), L-leucine (Leu), L-isoleucine (Ile), and L-valine (Val). Integrated over 200 laser pulses, 30 mJ/pulse, at 8 meter range. Spectra are baseline corrected and vertically shifted for clarity.

The complexity of the bands in the low frequency region, and sensitivity of these bands to shift because of minute structural changes provide a fingerprint for each organic molecule. For example, the smallest amino acid glycine and exact polymorph were univocally identified. At ambient conditions, glycine exists as α-glycine (space group $P2_1/n$), β-glycine (space group $P2_1$) and γ-glycine (space group $P3_1$), with γ-glycine being the most stable phase followed by α- and β-glycine (Goryainov et al., 2006; Isakov et al., 2014). The peak positions of the $NH_3$ rocking vibrational modes (1155.1 $cm^{-1}$) in combination with the positions of the C-N stretch and $CH_2$ symmetrical stretch vibrations (1048.0 and 2963.6 $cm^{-1}$ respectively) are characteristic of γ-glycine and they differ between the three polymorphs. Very similar amino acids, such as α- and β-alanine, can be easily distinguished by a slight shift in the lines of the Raman fingerprint region (Fig. 4.6). The CH deformational modes are found at slightly different positions because of the influence of the side-chain characteristics of each amino acid. Some bands result from vibrational modes on the side-chains. For example, L- phenylalanine (Fig. 4.4) is an aromatic amino acid and some Raman bands arising from CH rings are expected. The most prominent are found at 1004 $cm^{-1}$ and 3068 $cm^{-1}$, arising from the ring-breathing vibration in mono-substituted aromatic compounds and aromatic C–H stretch vibrations, respectively

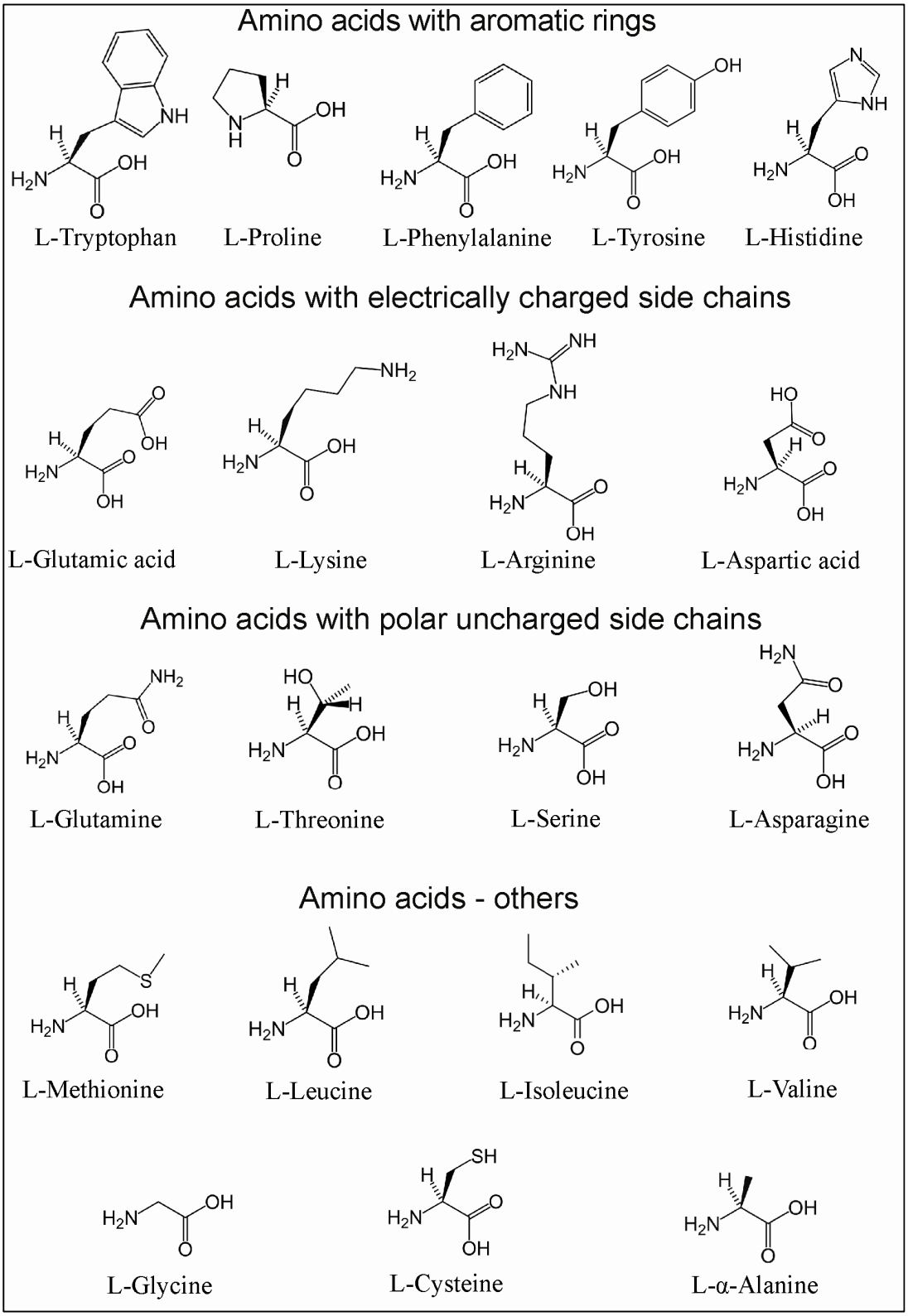


Figure 4.9: Grouped table of the measured 20 standard amino acids' structures.

(Elsila et al., 2009). The same bands in L-tryptophan are shifted to 1009 and 3057 $cm^{-1}$, making the distinction between both amino acids straightforward and unequivocal. A similar band arising from para-substituted ring vibration appears at 830 $cm^{-1}$ in the L-Tyr spectrum. Both L- phenylalanine and L-tryptophan show some fast fluorescence that does not hinder the Raman detection capabilities at 8 m range. Similar fluorescence was also measured for L-aspartic acid (Asp, Fig. 4.5), L-threonine (Thr, Fig. 4.7), L-serine (Ser, Fig. 4.7), and L-valine (Val, Fig. 4.8). For aromatic amino acids the fluorescence might arise from free electrons inside the aromatic rings, in the other amino acids it may be indicative of the biological origin of the measured material. This sensitivity to organics-derived florescence could also be of great help for the search of biomarkers in planetary exploration (Berlanga et al., 2015; Gasda et al., 2015).

### 4.6 Conclusions

Daytime detection of amino acids and nucleobases from a distance of 8 m is demonstrated using a portable, compact remote-Raman instrument. The remote Raman system is well suited for planetary exploration applications, with no requirement for sample preparation or collection, and has rapid measurement times.

# CHAPTER 5: REMOTE RAMAN MEASUREMENTS OF MINERALS, ORGANICS AND INORGANICS AT 430 METER RANGE

Submitted to Applied Optics as Acosta-Maeda, T.E., Misra, A.K., Sharma, S.K., Berlanga, G., Muchow, D., and Muzangwa, L. (2016) Remote Raman Measurements of Minerals, Organics and Inorganics at 430 m Range

## 5.1 Abstract

Raman spectroscopy is a characterization technique able to identify different molecules and crystal arrangements based on the interaction of the energy of their vibrational and rotational modes with light. The capability to analyze and detect water or water bearing minerals, minerals and organic materials is of special interest for planetary science, as they can indicate habitability or provide information about the geological context of the sample. Using a portable pulsed remote Raman system with a commercial 8" telescope a frequency doubled Nd-YAG pulsed laser and a spectrometer equipped with an intensified CCD camera, it was possible to acquire good quality Raman spectra of various materials from a 430 meter remote distance during daylight with detection times of 10 seconds, and as low as 1 second, in the realistic context that both the exciting source and the detector are part of the same measurement system. Remote Raman spectra at this distance provided unambiguous detection of compounds important for planetary science, such as water and water ice, dry ice, sulfur, sulfates, various minerals and organics, and atmospheric gases. These materials were both strong Raman scatters such as sulfur and weaker scatters such as water. Similar to a LIDAR system, the gated capability also allows measuring distance and performing distance selective measurements. This research work demonstrates significant improvement of the remote Raman technique as well as its suitability for Solar System exploration.

## 5.2 Introduction

Raman spectroscopy is a characterization technique able to identify different molecules and crystal arrangements based on the interaction of the energy of their vibrational and rotational modes with light (Ferraro et al., 2003). Molecular vibrational modes have particular energies unique to each chemical as they depend on atoms, bond strength and distance as well as molecular symmetry (Colthup et al., 1990). In the Raman Effect, the light scatters inelastically and yields a spectrum with frequency shifts from the light source, univocally identifying chemical compounds. Raman spectra can be obtained from gas, liquid or solid phases. In solids, Raman spectra also provide information on lattice modes, allowing to distinguish between mineral polymorphs (Triebold et al., 2011) and isomorphs (Frost et al., 2004). Raman spectroscopy requires no sample preparation and can provide univocal chemical characterization, of both organic and inorganic materials, without sample damage, and has successfully being used in a variety of fields ranging from geology to national security (Fini, 2004; Griffith, 1969; Hanlon et al., 2000; Kiefert and Karampelas, 2011;

Moore and Scharff, 2009; Petry et al., 2003; Rull Perez et al., 1999). Not surprisingly, Raman has been proposed and demonstrated as a powerful tool for planetary exploration (Angel et al., 2012; Rull Pérez and Martinez-Frias, 2006; Sharma et al., 2011; Wang et al., 1995). Micro-Raman systems have demonstrated their power by provided high quality spectra of small mineral grains in planetary materials (Wang et al., 2004) and a micro Raman instrument is part of the payload of the ExoMars 2018 mission of the European Space Agency (Lopez-Reyes et al., 2014). Remote Raman systems incorporate new traits to the Raman technique. Remote Raman systems are fitted with gated lasers and detectors which can perform fast measurements of planetary analogs under daylight at increasing distances (Misra et al., 2012; Rull et al., 2011; Sharma et al., 2011; Sharma et al., 2006; Sharma et al., 2009). The remote Raman technique employs lasers and detectors that can be timed down to nanoseconds, allowing for full Raman spectrum measurements while avoiding daylight background and some of the long-lived fluorescence that can undermine some Raman measurements (Blacksberg et al., 2016; Misra et al., 2005). In recent years, several research teams have been developing remote Raman systems in a wide area of applications (Bremer and Dantus, 2014; Bykov et al., 2015; Carter et al., 2005b; Dantus, 2014; Dogariu, 2013; Fulton, 2011; Gaft and Nagli, 2008; Gasda et al., 2015; Hokr et al., 2014; Hopkins et al., 2016; Izake et al., 2012; Lin et al., 2013; Loeffen et al., 2011; Moros and Laserna, 2011; Moros et al., 2011; Moros et al., 2013; Pettersson et al., 2010; Ramírez-Cedeño et al., 2010; Rull et al., 2011; Scaffidi et al., 2010; Sharma et al., 2011; Sharma et al., 2006; Sharma et al., 2009; Sharma et al., 2007; Wiens et al., 2016; Wu et al., 2000; Zachhuber et al., 2011a). For planetary science applications, larger measurement ranges increase the effective exploring area of a planetary rover, saving mission time and increasing the number of accessible targets (Abedin et al., 2015; Angel et al., 2012). A remote Raman system with a range in the order of hundreds of meters could also be developed (Angel et al., 2012; Measures, 1992) and can help best determine an optimal sampling sites in future asteroid sample return missions such as NASA's OSIRIX-Rex (Nakamura-Messenger et al., 2014) or discriminate between ices and different sulfates in Europa from a low orbit (Carlson et al., 2009). The University of Hawai'i (UH) has developed multiple remote Raman systems. A similar system used for this study can perform measurements of organic and inorganic chemicals such as benzene or calcite at 120 meters range (Misra et al., 2012) with a single laser pulse excitation. Pettersson et al. (2010) measured ammonium nitrate from a distance of 450 m during daylight and heavy rain, Chen et al. (2007b) measured benzene from 217 m meters with a single laser pulse,

Aggarwal et al. (2010) recorded the spectrum of sulfur with a continuous laser at nighttime up to a distance of 1500 m, and Hokr et al. (2014) measured ammonium nitrate with a single pulse from 400 m distance inducing stimulated Raman with the excitation laser at 8.5 m from the sample. This study reports the ability of our remote Raman system to perform good quality fast measurements at 430 m range, during broad daylight in Hawai‘i, of materials of interest to planetary exploration, both strong scatters such as sulfur and weak scatters such as water, in the realistic context that both the exciting source and the detector are part of the same measurement system. UH is collaborating with LANL and French partners IRAP and CNES under the Mars 2020 mission in which the SuperCam instrument will perform remote Raman analysis of Mars rocks, along with LIBS and time-resolved fluorescence (Wiens et al., 2016).

**5.3 Experimental setup:**

Figure 5.1: The 8 inch remote Raman+LIBS+Fluorescence System and the pan-&-tilt mount during the experiment. The system is mounted on a reinforced utility cart to improve aiming stability at large distances. The sample is located 430 m away, to the left of this image.

Figure 5.1 shows the remote Raman+LIBS+Fluorescence system in the UH Mānoa campus aiming at the target samples placed in a balcony at 430 meter range. The photograph shows the system with all its components mounted in a reinforced portable trolley during the measurements taken in this chapter. Figure 5.2 shows the system aiming at the target samples placed in a balcony 430 m away, with an inset showing a zoomed in image of the balcony with the laser hitting on the sample. Figure 5.3 shows a diagram depicting the layout of the main components of the system as well as the main optical paths. The system is gated with coaxial geometry, with the expanded laser beam brought to the optical axis of the detector by means of two elliptical turning mirrors. The optical collector is an 8-inch (203.2 mm) diameter telescope (Meade LX-200R Advanced Ritchey- Chretien, f/10). The sample is excited with a frequency- doubled Q-switched Nd:YAG pulsed laser source (Quantel Laser, ultra model, 532 nm, 100 mJ/pulse, 15 Hz, pulse width 10 ns). The spectra are recorded with a Kaiser Optical Systems f/1.8 HoloSpec spectrometer fitted with a 1024x256 pixels intensified CCD (ICCD) camera (PI-IMAX, Princeton Instrument, Trenton, NJ). The telescope is directly coupled to the spectrometer through a camera lens (50 mm, f/1.8) which focuses the Raman signal into the 50 μm entrance slit of the spectrometer. A 532-nm

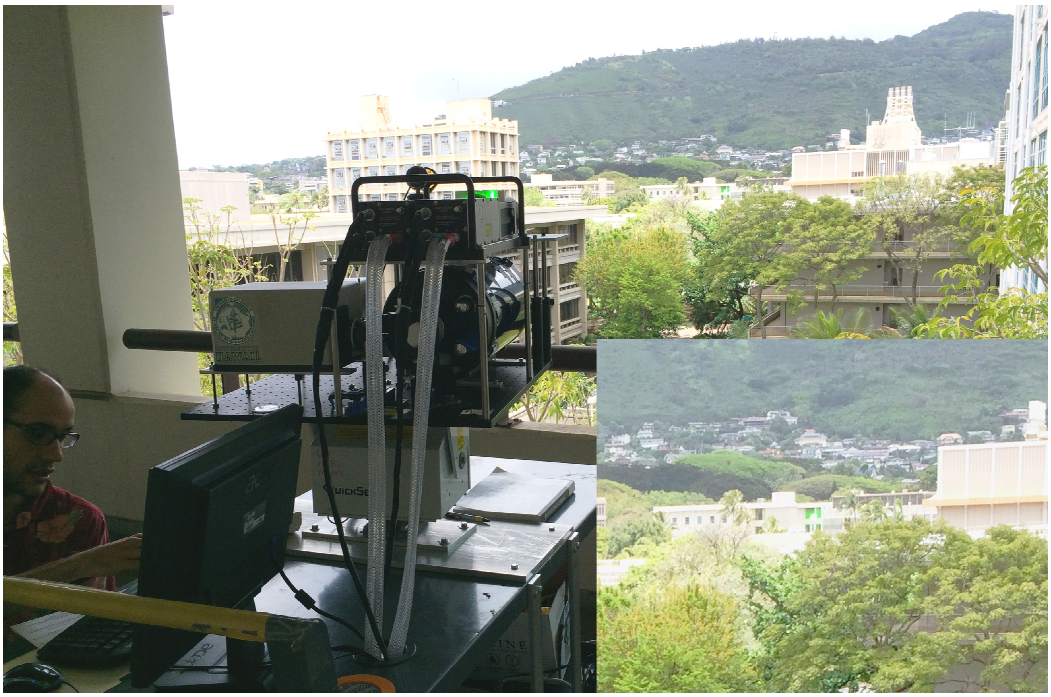

Figure 5.2: The system looking towards the sample in the distance. The inset shows a close up of the sample location 430 m from the system. The laser spot is visible in the image, the sample is not visible with the naked eye or a point and shut digital camera.

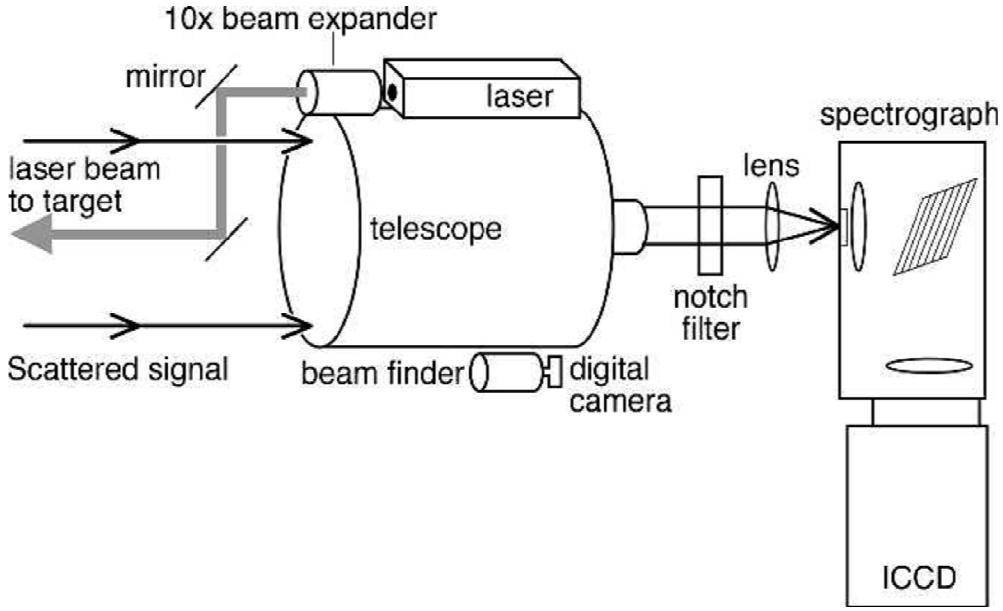


Figure 5.3: Schematic diagram of the directly coupled pulsed remote Raman system in coaxial geometry using an 8-inch telescope, an Nd-YAG laser, a gated ICCD detector, transmission spectrograph, and a 10X beam expander to produce a circular beam at the target.

SuperNotch filter (Kaiser Optical Systems) is used to remove the reflected and Rayleigh scattered laser light. Both the excitation and collection parts of the system are mounted on a pan-&-tilt scanner (QuickSet, Northbrook, IL) allowing to accurately aiming the system at large distances. This setup enforces that the coaxial optical alignment remains when moving the system, and through operational and wind vibrations and oscillations. The laser diameter is adjusted on the sample through a 10x beam expander mounted in front of the laser. This is used to obtain a parallel beam and a round laser spot of about 10 cm in diameter at 430 meter. With a large laser spot and large laser output power (100 mJ/pulse) it is possible to excite larger sample volume without photo-damaging or heating the sample, thus exciting more molecules and generating more Raman signal. Liquid samples were placed in large vials and powdered samples were placed inside 6 inch diameter petri dishes. For laser safety, each sample was placed in a wooden box with one side open, facing the system. The system was aimed by roughly pointing the trolley towards the sample and then using the pan-&-tilt scanner and a custom sight on the side of the optical tube to bring the laser onto the sample. The laser spot position oscillated around 5 cm from its center

position throughout the experiment run, mainly because of wind induced vibrations. The laser-collection optics were fine-adjusted by optimizing the measured fluorescence signal from tree leafs located beyond the sample; these are visible above the sample location (Fig. 5.2), at more than 1600 m range. The timing was set up by connecting the trigger signal from the laser q-switch to the input sync port of the ICCD. The timing has an accuracy of about 10 ns, which allows the system to take a reference time 0 when the laser is fired, introduce a delay in the ICCD camera response, and take a measurement when the inelastically scattered Raman photons arrive to the camera (Misra et al., 2011). By varying the delay and the measurement gate, it is possible to measure different volumes of atmospheric gas at different distances in front of the sample, as well as measuring only the sample. For the sample measurements in this chapter I used 25 mJ per pulse at laser power at 15 Hz repetition rate with 2900 ns delay and 50 ns measurement gate width. After correcting for electronic delay and delay incurred before the laser beam leaves the system, the sample distance was calculated using the delay and the speed of light to be 430 m. This distance was confirmed by using the measurement tool of Google maps (Google Maps, 2015). The spectrometer uses a holographic volume-phase transmission grating that allows to measure between 50 and 4200 $cm^{-1}$ with a spectral resolution of 8 $cm^{-1}$. The transmission grating splits the spectral range into two traces that that spread horizontally into two traces at different heights on the sample. The data from the ICCD were acquired using the software package WinSpec 32-bit Windows Princeton Instruments from Roper Scientific. Every spectrum was generated and wavelength calibrated using the custom Matlab software UH Raman-LIBS v1.61. The wavelength calibration was performed using the Raman peaks of calcium carbonate, cyclohexane, acetonitrile, calcium sulfate dehydrate and atmospheric nitrogen as a reference. Spectral plots were created with the GRAMS/AI 8.0 software package from Galactic Industries. Spectra are shown as measured, with no baseline or cosmic ray correction, intensity calibration or stitching procedures.

### 5.4 Samples

The rock and rock-forming mineral samples, quartz, gypsum and anhydrite, were from Ward's Natural Science Establishment, Inc., Rochester, NY, and were measured without any sample preparation. The organic liquids cyclohexane**,** acetone, acetonitrile, methanol, benzene were ACS grade purchased from Fisher Scientific. Potassium nitrate ($KNO_3$), ammonium nitrate ($NH_4NO_3$), potassium chlorate ($KClO_3$), sulfur, and urea were purchased

from Fisher Scientific; and potassium perchlorate ($KClO_4$) was purchased from Alfa Aesar. The water ($H_2O$) was regular tap water from Honolulu, Hawai‘i. The ice was made from regular tap water and dry ice was purchased as cooling pellets from the chemistry supplier in the UH Mānoa campus.

**5.5 Results and Discussion:**

This chapeter shows the successfull measurement of acetone, benzene, cyclohexane, dry ice, gypsum, potassium chlorate, potassium perchlorate, potassium nitrate, ammonium nitrate, marble rock, methanol, quartz, sulfur, urea, water and water ice, acetonitrile, anhydrite, and magnesium sulfate (Epsom salt) at a range of 430 m with integration times of 10 s or less. Tree leaf fluorescence was measured in a nearby mountain, as far as 1600 m away. All the measurements were taken outdoors on broad daylight. Figures 5.4 and 5.5 show time series measurements of powdered ammonium nitrate and sulfur respectively, located at 430 m. In a pulsed Raman system the detector needs to be timed to the arrival of the Raman and Rayleigh signals from the sample. The measured target distance stems from the time the

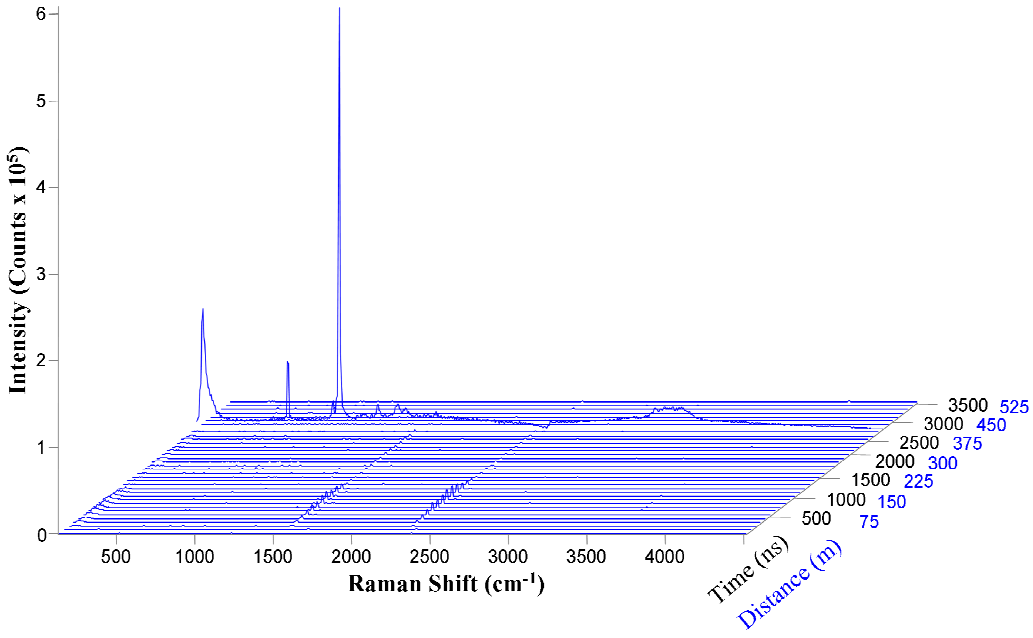


Figure 5.4: Time series measurements of ammonium nitrate ($NH_4NO_3$) at 430 m. The Y axis shows the detected intensity in counts while the X axis shows the Raman shift in $cm^{-1}$. The Z axis shows the delay time in nanoseconds, along with the sample distance corresponding to each indicated delay. Each spectrum was taken at 100 ns intervals, with 100 ns exposure time added over 15 laser pulses with 100 mJ/pulse laser power.

laser photons, travelling at the speed of light, take in going to the sample and back to the system. Time zero is the time at which the laser pulse leaves the system, and the delay time indicates the time at which the camera starts collecting the signal. The expected arrival time is simply determined by sample distance and speed of light. At shorter distances the system looks at and measures the atmospheric gases between the system and the sample, the oxygen and nitrogen symmetrical stretching vibrations are visible at 1555 and 2331 $cm^{-1}$. Their intensity decreases as the distance increases, as expected, as the irradiance of the scattered signal is proportional to the inverse of the square of the target distance. The Raman signal from the sample arrived with a delay of 2900 ns, indicating a sample distance of 430 m.

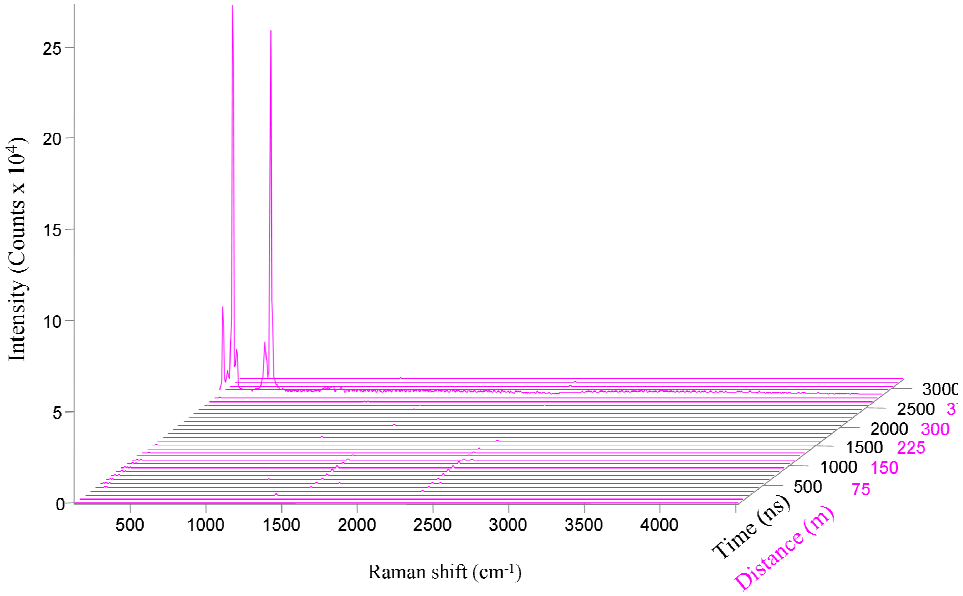


Figure 5.5:Time series measurements of sulfur at 430 m. Each spectrum was taken at 100 ns intervals, with 100 ns exposure time added over 15 laser pulses with 100 mJ/pulse laser power.

No signal is detected after the sample since the mineral target stops the laser from travelling further. Fig. 5.4 shows clear detection of ammonium nitrate with fingerprint Raman bands in low as well as high frequency region. In Fig. 5.5, Raman bands of sulfur are easily detected. In Figure 5.4, the signal from the atmospheric gases appears larger than in the time series in Figure 5.5. This is because the ammonium nitrate Raman signal is about 5 times weaker than that of the sulfur, and the data for ammonium nitrate is accumulated over 10 s integration time in comparison to the 1 s integration time for the sulfur target. Sulfur has a very large Raman cross section (Aggarwal et al., 2010), larger than both atmospheric oxygen, nitrogen

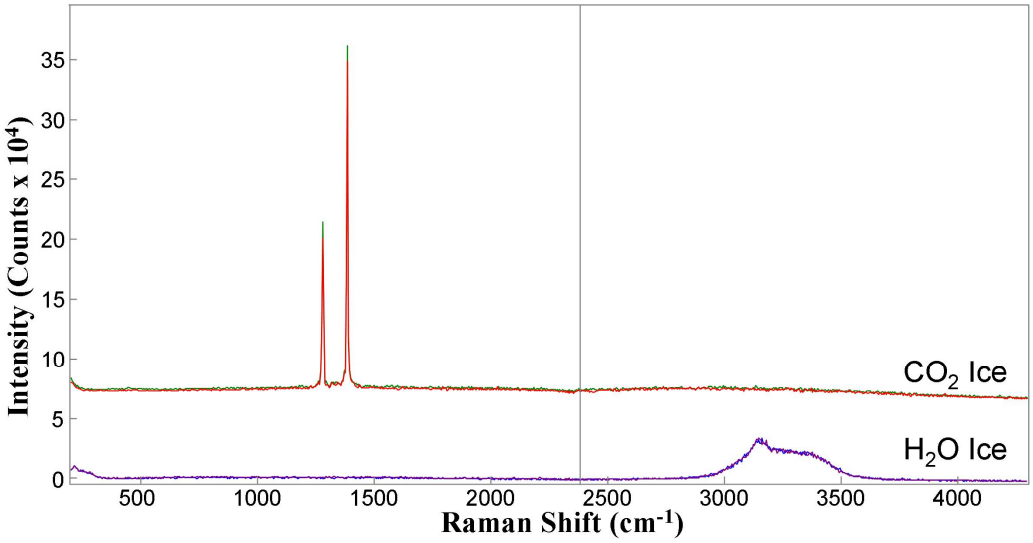


Figure 5.6: Remote Raman spectra of $CO_2$ ice (dry ice) and water ice with 10 s acquisition time at 430 meter range. Each spectrum was acquired over 150 laser pulses with 100 mJ/pulse laser power. Two consecutive spectra are shown as measured for each sample to demonstrate repeatability.

or ammonium nitrate. Three of the eleven fundamental modes of the cyclic crown-shaped $S_8$ molecules give three intense Raman peaks at 153, 219 and 473 $cm^{-1}$, which are clearly visible in Fig. 5.5 (Misra et al., 2012). These peaks originate from the doubly degenerate bending ($\nu_8$), symmetric bending ($\nu_2$), and symmetric stretching ($\nu_1$) vibrational modes of the cyclic molecule (Harvey and Butler, 1986; Pasteris et al., 2001).

Figure 5.6 shows the remote Raman spectra of dry ice (solid $CO_2$) and water ice (solid $H_2O$) with 10 seconds acquisition time. Dry ice and water ice are commonplace in the Solar System. Both spectra are very distinct. Carbon dioxide spectrum shows its characteristic doublet at 1284 and 1392 $cm^{-1}$ (Cahill and Leroi, 1969). The $\nu_1$ totally symmetric stretching vibration of $CO_2$ at 1305 $cm^{-1}$ is Raman active and is in Fermi resonance with the 2 $\nu_1$ overtone of the I.R. active bending mode of the linear carbon dioxide molecule at 667 $cm^{-1}$. Therefore, the spectrum of dry ice shows two strong Raman lines. The water ice spectrum shows the symmetric and antissymetric stretch vibrational modes of the H-O-H bond of the water molecule between 3100-3600 $cm^{-1}$. The ice spectrum is can be distinguished from the water spectrum by the sharper solid water peak at ~3100 $cm^{-1}$. The sharper peak is due to increased ordering in the solid phase. The band also experiments a downward shift due to the

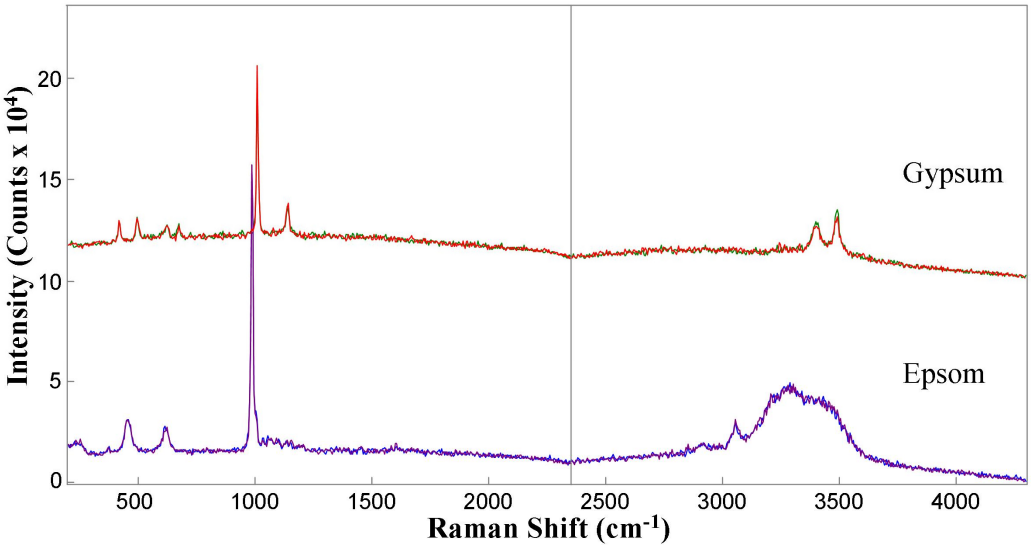


Figure 5.7 Remote Raman spectra of $CaSO_4 \cdot 2H_2O$ (Gypsum) and $MgSO_4 \cdot 7H_2O$ (Epsom) at 430 m range. Same experimental conditions as in fig. 5.6. Two consecutive spectra are shown for each sample to demonstrate the reproducibility of the system.

strengthening of the O-H bond and its position depends on temperature and can help in determining the temperature of the measured water ice (Furić and Volovšek, 2010).

Figure 5.7 shows the remote Raman spectra of gypsum ($CaSO_4 \cdot 2H_2O$) and epsum salt ($MgSO_4 \cdot 7H_2O$) with 10 seconds integration time, equivalent to 150 laser pulses. Gypsum and Epsom salt are both hydrated sulfates and therefore show similar Raman peaks corresponding to the symmetric stretching vibrations $\upsilon_1$ in the sulfate ions $SO_4$ at 1008 and 984 $cm^{-1}$ respectively (Wang et al., 2006). The slight difference in peak positions and the sharp contrast in the O-H stretching region (~3400 $cm^{-1}$) are enough to differentiate between both minerals at 430 meters. This capability could help identifying different sulfates on the surface of Jupiter's satellite Europa (McKinnon and Zolensky, 2003) or to confirm the chemical compound of Homestake in Mars, believed to be mostly gypsum based on Alpha Particle X-Ray Spectrometer and Pancam instrument measurements onboard the Opportunity rover (Squyres et al., 2012).

Figure 5.8 shows the remote Raman spectra of ammonium nitrate ($NH_4NO_3$), potassium nitrate ($KNO_3$), with 10 second integration time, equivalent to 150 laser pulses. In the potassium nitrate spectrum, the 1052 $cm^{-1}$ peak corresponds to the symmetric stretching vibrations $\upsilon_1$ in the nitrate ions $NO^{3-}$. The 1349 $cm^{-1}$ peak corresponds to the $\upsilon_3$ mode. The $NH_4NO_3$ and $KNO_3$ molecules both contain $NO^{3-}$ ions, and the 1044, 1288, and 1655 $cm^{-1}$

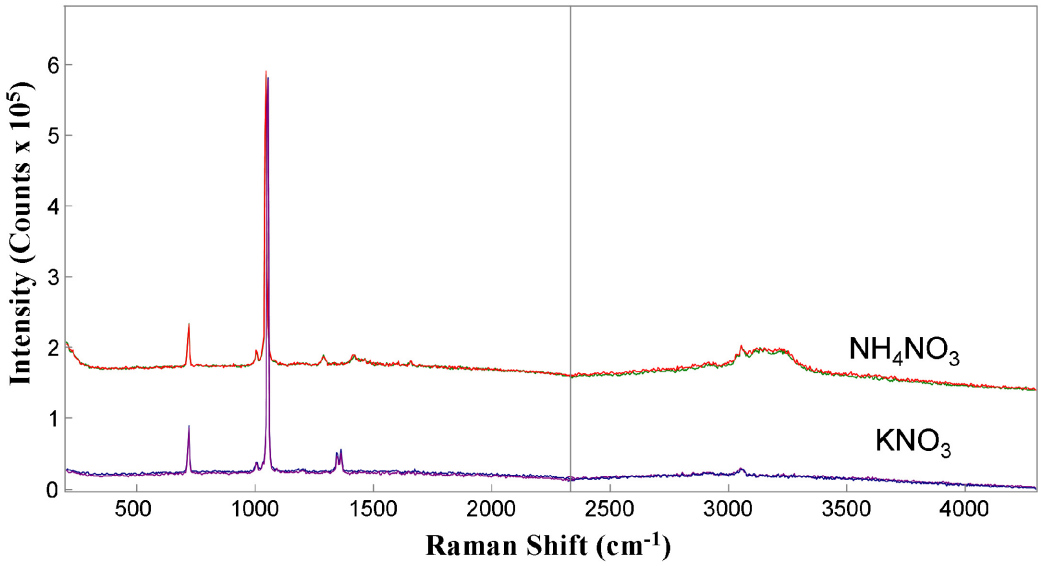


Figure 5.8 Remote Raman spectra of $NH_4NO_3$ and $KNO_3$ at 430 m range. Same experimental conditions as in fig. 5.6.

Raman vibrational modes of $NH_4NO_3$ are analogous to the 1052, 1349, and 1664 $cm^{-1}$ peaks in $KNO_3$ (Kettle, 1982). In the ammonium nitrate, the multiple peaks between 1400 and 1500 $cm^{-1}$ are the result of vibrational coupling between some ammonium ion deformation and nitrate stretching (Kettle, 1982), and are distinct from the signature peaks of potassium nitrate in the same spectral area. The signal in the N-H stretching region between 3000-3300 $cm^{-1}$is characteristic f the ammonium ion in the ammonium nitrate and is also in stark difference with the potassium nitrate The sharper band appearing at 3015 $cm^{-1}$ is due to C-H stretching vibrations of the polystyrene petridish, also detectable at this distance. All the powdered solids contained in petridishes showed this signals throughout the experiment run.

Figure 5.9 shows the Raman spectrum of potassium chlorate ($KClO_3$) and potassium perchlorate ($KClO_4$) with 10 second integration time, equivalent to 150 laser pulses at 15 Hz repetition rate. Potassium chlorate and potassium perchlorate show distinct Raman peaks that allow unequivocal chemical identification at 430 meter range in as low as 1 second integration time. The potassium chlorate shows its fingerprint peak at 930 $cm^{-1}$ very clearly, while the potassium perchlorate appears at 942 $cm^{-1}$, both bands due to symmetric stretching vibrations $\upsilon_1$ in the chlorate or perchlorate ions respectively. Besides different Raman shifts, the shoulder of the main peak in the potassium perchlorate spectrum at 924 $cm^{-1}$ is characteristic from the perchlorate. It arises from the first overtone of the symmetric bending

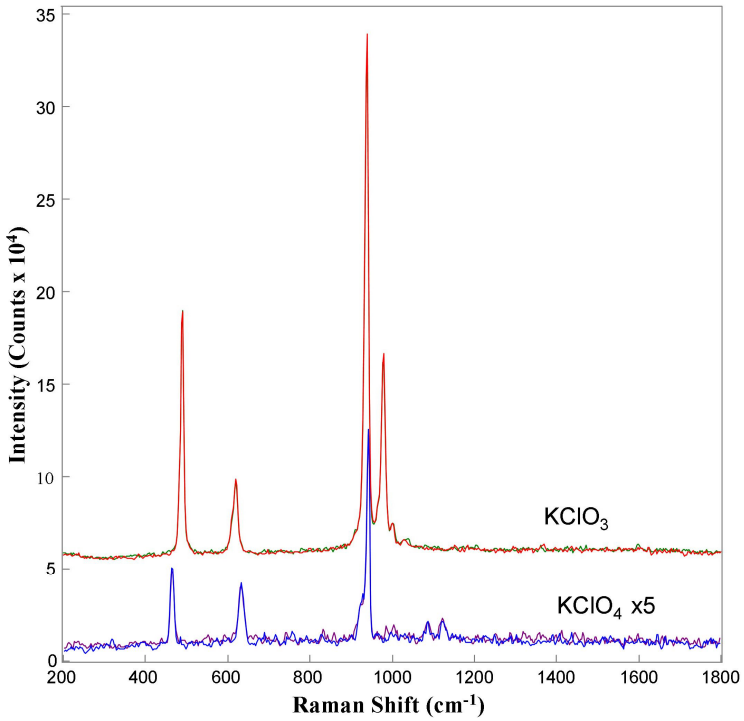


Figure 5.9: Remote Raman spectra of $KClO_3$, and $KClO_4$ at 430 m range with 1 s detection time. The KClO4 spectra have been scaled 5 fold for clarity. Same experimental conditions as in fig 5.6.

vibration of the $ClO_4$ ion, enhanced by Fermi resonance (Bini et al., 1990). The other other Raman peaks of the $ClO_4^-$ ion are found at 629 $cm^{-1}$arising from the antisymmetric bending ($\upsilon_4$) mode, and 1087 and 1125 $cm^{-1}$, arising from antisymmetric stretching ($\upsilon_3$) vibrational modes (Lutz et al., 1983; Toupry et al., 1983). In the chlorate, the two additional bands appear at 489 and 619 $cm^{-1}$ corresponding to the $\upsilon_3$ and $\upsilon_4$ vibrational modes of the $ClO_3^-$ ions (Ramdas, 1953; Robinson, 1963; Sprowles and Plane, 1975). Figure 5.10 shows the distinct Raman spectra of ammonium nitrate, potassium nitrate, potassium chlorate and urea acquired with fast 1 s integration time, equivalent to 15 laser pulses. The plot demonstrates that these chemicals, as well as water and $CO_2$ ices, sulfur and the sulfates, can be univocally identified at 430 meters distance with 1 s measurement. The urea peaks are found at 1002 $cm^{-1}$ as well as at 1160 $cm^{-1}$. These two peaks correspond to the two $NH_2$ rocking vibrations in the planar $NH_2$-CO-$NH_2$ urea molecule. The peak at 1468 $cm^{-1}$ corresponds to the anti-symmetric NCN stretching mode and the peak at 1540 $cm^{-1}$ to a $NH_2$ bending mode. The

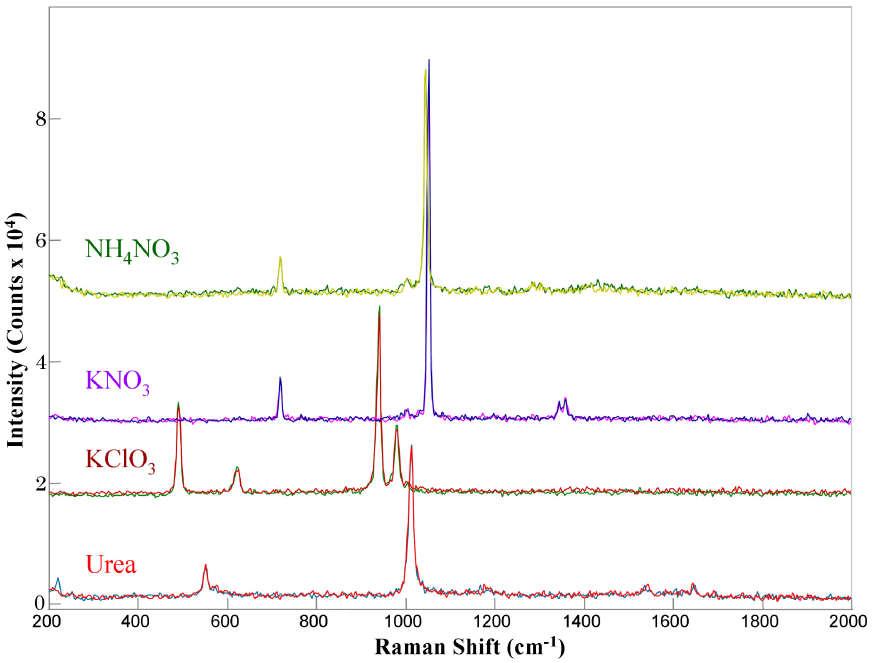


Figure 5.10: Remote Raman spectra of $NH_4NO_3$, $KNO_3$, $KClO_3$, and urea at 430 m range with fast 1 s detection time (15 pulses) and 100 mJ/pulse laser power. Two consecutive spectra are shown for each sample to demonstrate repeatability.

1578

and 1647 $cm^{-1}$ urea peaks are also visible and correspond to stretching modes of the free and hydrogen bonded C-O group (Frost et al., 2000).

Figure 5.11 shows the remote Raman spectra of the organic liquids cyclohexane, benzene and methanol. The three liquids are easily measured and differentiated by the differences in their chemistries and molecular symmetries. The C-H stretching region of cyclohexane shows prominent lines at 2854 $cm^{-1}$, corresponding to $CH_2$ symmetrical stretch vibrations, and two bands 2924 and 2940 $cm^{-1}$ corresponding to $CH_2$ antisymmetric stretch vibrations enhanced by Fermi resonance with the 1st overtone of the $CH_2$ scissors vibration found at 1462 $cm^{-1}$ (as a shoulder of the more intense 1444 $cm^{-1}$). The benzene spectrum is dominated by the strong line at 993 $cm^{-1}$ due to C-H ring stretching vibrations and the peak in the spectral area between 2990 and 3150 $cm^{-1}$, arising from C-H stretch vibrations. The Raman spectrum of methanol is shows the C-O stretch line at 1033 $cm^{-1}$ and the broad C-H symmetrical and antisymmetrical stretch Raman signals in the C-H stretching region (Mammone et al., 1980; McCreery, 2002; Shimanouchi, 1972). The measured benzene spectrum has an unusual weak line at 1978 $cm^{-1}$. This line showed to change its intensity

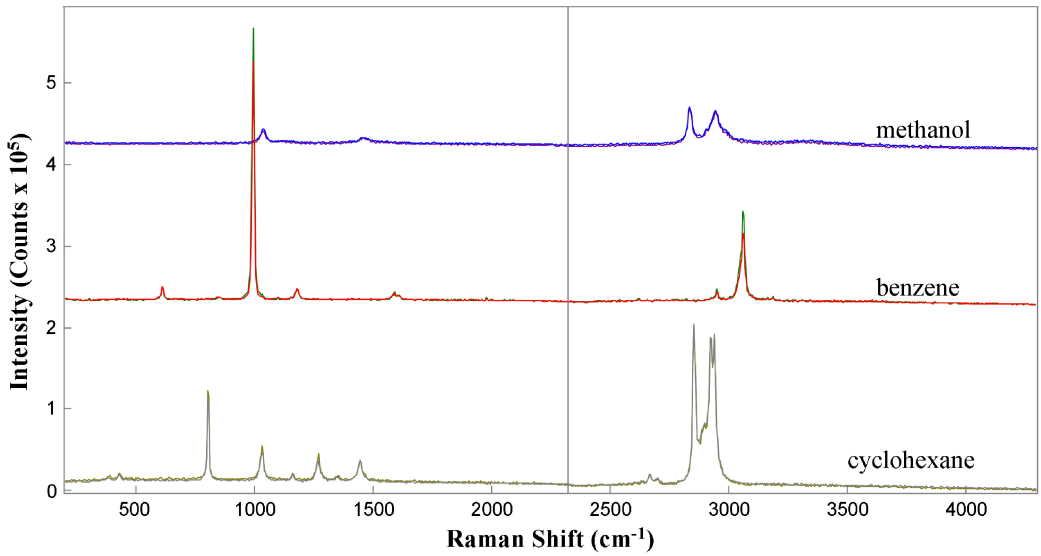


Figure 5.11: Remote Raman spectra of cyclohexane, benzene and methanol at 430 m range. Same experimental conditions as in fig 5.6.

proportionally to the intensity of the main C-H ring stretching line at 993 $cm^{-1}$, suggesting that it is the first overtone of the C-H ring stretching vibration. This peak and a more intense benzene spectrum is probably observed because of stimulated Raman emission because self focusing of the laser inside the cylindrical bottle filled with benzene. Being able to induce and measure stimulated Raman from a distance can aid in improving signal to noise ratio and increase measurement ranges (Hokr et al., 2014).

## 5.6 Conclusions

This work demonstrates the capability of a medium-size portable remote Raman system to detect various chemicals and minerals from a distance of 430 m in the afternoon with sunlight shining on the samples. Good quality Raman spectra of water ice, dry ice, sulfur, gypsum, Epsum, potassium nitrate, ammonium nitrate, potassium chlorate, potassium perchlorate, urea, benzene, cyclohexane, and methanol were obtained with short integration times (≤10 s) using an 8" telescope as collection optics. Materials with strong Raman cross-section could be detected with just 1 s integration time. The capability to analyze and detect water or water bearing minerals, minerals and organic materials is of special interest for planetary science, as they can indicate habitability or provide information about the geological context of the sample. Remote Raman spectra at this distance provided unambiguous detection of compounds important for planetary science, such as water and

water ice, dry ice, sulfur, sulfates, and various minerals and organics. This research work demonstrates significant improvement of the remote Raman technique as well as its suitability for Solar System exploration.

# CHAPTER 6: CONCLUSIONS

### 6.1 Raman spectroscopy for planetary science

Raman spectroscopy is a powerful tool that can be used to determine the chemical composition and structure of a variety of samples. Raman spectra arise from the quantified vibrational energy of molecules, which in turn depend on vibrational modes, and these are unique to each molecule (Ferraro et al., 2003). Thus, Raman spectroscopy can provide accurate and unequivocal identification of the minerals, glasses, liquids, gasses, and organic materials one might expect to encounter during planetary exploration (Wang et al., 1995). Furthermore, Raman spectra provide information on molecule and crystal structures and can be used to discriminate polymorphs or small structural variations of the same chemical (Acosta-Maeda et al., 2013). Not surprisingly, new minerals have been characterized using a Raman spectrum as one of the first proofs (Gillet et al., 2000). Moreover, Raman spectroscopy can often be performed without sample preparation and without inducing sample damage. These advantages of Raman spectroscopy make the technique a good candidate to analyze the materials within reach of a planetary rover, providing more accurate information than a simpler alpha particle X-ray spectrometer and with a broader scope than a Mössbauer spectrometer. With that in mind, the European Space Agency included the Laser Raman Spectrometer in its Exomars 2018 mission, a micro-Raman system with a 532 nm Nd-YAG laser that will measure ground drill cores of Martian samples (Rull Perez and Maurice, 2016). However, Raman spectra are not simple to measure, and often low signal or fluorescence interference hinders the measurement. Therefore it is fundamental to develop techniques and apply technological advances to make Raman spectroscopy more versatile. Once a measurement is taken, its interpretation requires the use of the accumulated Raman database available in the literature since the 1920s. This dissertation aims, in part, to add knowledge to the database in the field of planetary science and to develop and apply measurement techniques that could be used with great advantage by Raman users and scientists.

Remote Raman sensing is the idea behind remote Raman spectroscopy. This technique can also be installed in a planetary exploration rover, increasing its measurement range and allowing to measure points of difficult access (Angel et al., 2012). NASA acknowledged this by including remote Raman capabilities to the Supercam instrument in the Mars 2020 mission, in combination with laser induced breakdown spectroscopy (Wiens and Maurice, 2016). This dissertation also aims to provide a baseline for what can be expected from measured samples of interest related to planetary science, such as geologic materials,

organic compounds or water. Finally, this dissertation also aims to develop better more suitable remote systems: sensitive and with longer measurement range; and more compact and with lower power consumption; with the intention of making space worthy instrumentation.

Using the Raman equipment at the Hawai‘i Institute of Geophysics and Planetology I performed a comprehensive Raman study of a highly shocked meteorite sample. Most of the shocked meteorites belong to the ordinary chondrite type, but also to other meteorite families, including Martian meteorites. The study of these meteorites is fundamental to understand impact processes in the Solar System, of paramount importance since impacts on Earth have, and are bound to happen with catastrophic consequences. Furthermore, the understanding of the mineral phases and relationships in the shocked silicates translates into better understanding the high pressure phases present in the Earth's mantle, whose properties can help constraining Earths layering or its bulk composition. Raman spectra using different excitation wavelengths and Raman mapping allowed identification of mineral phases such as olivine, wadsleyite, ringwoodite, high-Ca clinopyroxene, majorite-pyrope, jadeite, maskelynite, and lingunite in a heavily shocked L6 chondrite, as well as establishing phase relationships between the different high pressure polymorphs at the induced ~18.5 GPa ~1875 K forming conditions. I found evidence of chemical fractionation during a solid-state olivine-ringwoodite transformation. I also observed resonance Raman effects on the spectra of different colored ringwoodite, and the Raman mapping showed a clear relationship between a Raman peak and the optical properties of the ringwoodite. This work suggest that ringwoodite can exist in the known pure spinel structure, or in the spinel structure with some of the atoms in the marginally inverse structure, with a small amount of iron in fourfold coordination inside the spinel structure. During this part of the research I found Raman mapping in combination with the use of different excitation laser wavelengths instrumental in obtaining the results and final interpretation. Also, the data provided should help in characterizations, should an in-situ measurement in a Solar System’s planetary body or a researcher in a laboratory encounter similar spectra.

In the field of remote Raman, three differen three different studies were conducted: one aimed to provide physical Raman constants (cross sections) useful to planetary exploration; another to demonstrate the ability of a compact system to detect and characterize organic materials; and a last one to test and demonstrate the possibility of performing Raman measurements at a large range of 430 m. The last study could be considered part of an

international research race to increase measurement ranges. Although some other authors have performed measurements at larger distances (Aggarwal et al., 2010), to my knowledge, the long range results presented in this dissertation are the highest quality spectra taken from a diverse set of samples in realistic conditions, outdoors and in broad daylight. Throughout the developing and testing of systems and techniques, focused was on the capability to analyze and detect water or water bearing minerals, minerals and organic materials of special interest for planetary science. These can indicate habitability or provide information about the geological context of the measured samples.

Chapter 3 provided a detailed description of the methods used to determine the Raman cross sections of different ions of interest to planetary science as observed with 532 nm laser excitation remote Raman systems, the same wavelength the upcoming Mars missions are going to use. The cross section is a constant for each compound that describes its intrinsic ability to generate Raman signal (McCreery, 2000). Also shown is the calculated cross sections and observed Raman spectra of a variety of organic and inorganic compounds, such as sulfate, alcohols or water. As an example, this dissertation quantitatively described that ne can expect to more easily obtain carbohydrate spectra, than sulfate, carbonate or borate, in that order. One can expect that the obtained data will provide an accurate baseline for the detection capabilities of the upcoming and future planetary Raman systems, as well as serve as a tool for the interpretation of the measured spectra. The results presented in Chapter 4 were obtained with a compact remote Raman system, which includes a spectrometer 1/32 the volume of commercial versions with the same sensitivity and range, and a miniaturized low voltage intensified CCD camera. Within the limitations of laser power and limited collection optics diameter, I demonstrated that most amino acids and nucleobases can be detected from a distance of 8 m using a portable, compact remote-Raman instrument. The system is well suited for planetary exploration applications, with no requirement for sample preparation or collection, and rapid measurement times. It can be expected such a system to perform better that the Raman systems currently scheduled to fly (Gasda et al., 2015), and as such the current design can be used as a stepping-stone for the design of future planetary missions' Raman instruments, as well as a baseline for their detecting capabilities. The same can be said about the results shown in Chapter 5. There it was demonstrated the capability of a medium size portable remote Raman system to detect various chemicals and minerals from a distance of 430 m under broad daylight. This work demonstrated that good quality Raman spectra of water ice, dry ice, sulfur, gypsum, Epsum, potassium nitrate, ammonium nitrate,

potassium chlorate, potassium perchlorate, urea, benzene, cyclohexane, and methanol can be obtained with short integration times (≤10 s) using an 8" telescope for collection optics. Materials with strong Raman cross-section, such as sulfur, chlorates and nitrates, could be detected with just 1 s integration time. Remote Raman spectra at this distance provided unambiguous detection of compounds important for planetary science, such as water and water ice, dry ice, sulfur, sulfates, and various minerals and organics. The research work presented in Chapter 5 demonstrates significant improvement of the remote Raman technique as well as its suitability for Solar System exploration.

In summary, I can strongly conclude that the advantages of Raman spectroscopy make the technique a good candidate to analyze the materials within reach of a planetary Rover. For example, Raman capability could help identifying different sulfates on the surface of Jupiter's satellite Europa (McKinnon and Zolensky, 2003) or fast and unequivocally confirming the chemical compositions of samples such as Homestake in Mars (Squyres et al., 2012), believed to be gypsum formed in an aqueous environment. Remote Raman is a technique in development. However, recent advancements have made it suitable to increase a rover's sampling range, and will yield useful results in upcoming and future planetary missions, especially in integrated combination with other techniques, such as laser induced breakdown spectroscopy or time-resolved fluorescence. The work presented will help with the interpretation of measurements taken with current systems and will aid in the development in future more powerful systems. This work also sends a strong reminder that micro-Raman technique can be used for a lot more that mineral identification, in this case describing in detail the petrology of the high pressure mineral phases in a highly shocked meteorite, and explaining the structural origin of an observed (and identified as such) Raman resonance.

It is important not to forget that Raman spectroscopy, and thus the developments presented in this dissertation, can be extremely useful in a variety of other fields. The results and ideas regarding remote Raman translate well to the fields of explosive detection or monitoring of toxic residues from safe distances (Misra et al., 2012). Micro-Raman continues to be a strong technique in fields as unalike as medicine (Kamemoto et al., 2010) or civil engineering (Potgieter-Vermaak et al., 2006).

## 6.1 Future Work

Despite the information, examples, data and ideas given in this dissertation, Raman spectroscopy has yet to be performed outside Earth. I expect future measurements to be challenging and full of discoveries.

In the future, I will keep up with new technological developments in the fields of optics, laser optics and fast high sensitivity light detectors, in order to best apply the new devices to the goal of developing faster, more sensitive, longer reaching, more compact and lower power consuming remote Raman systems. I can focus in different areas of the process, from optics design to data interpretation. Collaboration with industry and other researchers needs to continue to develop photonics tailored to the planetary Raman application. Every new design needs to be tested in order to best define which direction to follow. To help with future data interpretation, one can design experiments to quantify the thumb rule of 1% detection limit of Raman spectroscopy for a variety of materials of planetary interest (e.g., detection limit of magnesium sulfate in water or $CO_2$ ice). Most notably, Chapter 3 shows Raman cross sections of ions in solution. The dissertation shows that one can attempt the design and perform an experiment to determine the more realistic solid cross sections of the same ions, when applicable. Extrapolation of the results reported in Chapter 5 suggests the possibility of performing Raman measurements at ~2 km. One can further test such system capabilities and improve aiming and aligning by designing experiments that exceed the dimensions of our research facilities. I am currently working in a concept that uses remote operated vehicles or unmanned aerials devices to bring small optics close to the measured sample while keeping the bulk of the system (collector, spectrometer, and detector) at a distance. This concept could also be used for planetary exploration; to increase the sampling range of a rover.

Regarding Chapter 2, the possibilities are endless in meteoritics. For the sample studied here, I observed a gradual change of mineralogy along the thickness of the studied melt vein. One could use Raman spectroscopy to try to determine the formation conditions of the varying assemblage as a function of pressure and temperature. Such study might shed light on the formation conditions of lingunite or the ordered-disordered ringwoodite. Some X-ray diffraction data on the same sample suggest that pure spinel white ringwoodite is composed of large crystals, while marginally inverse spinel blue ringwoodite is polycrystalline. Confirmation of the observations in other samples is pending and I hope to build a hypothesis that marries all the observations, and plan then to test such a hypothesis on

the same or different samples. In addition to continuing this study, in the future it will be possible to develop advanced micro-Raman systems using low-power pulsed lasers and gated detectors, similar to remote Raman systems, to minimize background signals from room light and mineral phosphorescence. These systems could also perform micro-LIBS on the material to confirm elemental composition. The advanced micro-Raman systems would not require dark rooms or expensive optical tables, making it feasible to have Raman systems in most laboratories for Earth and planetary materials characterization.

## **APPENDIX 1.** Sample from Chapter 2.

The meteorite used for the study of Chapter 2 of this dissertation work is the Taiban (b), L6-S6 ordinary chondrite. It was found in De Baca County, New Mexico in 1975 (Taiban (b) of Lange D. E., et al. 1980, Catalog of the meteorite collection of the Institute of Meteoritics at the University of New Mexico. Special Publication 21, UNM Institute of Meteoritics.). Thin slides of the same meteorite were used in the work of Stöffler et al. (1991). This is was not the Taiban (b) LL6 ordinary chondrite found in the same area in 1984 (Jeffrey N. Grossman, Meteoritical Bulletin 84, 2000), nor the Taiban meteorite found in 1934 (Grady, M. M. (2001) Catalogue of Meteorites, 5th Ed. Natural History Museum (London, England) Cambridge University Press). A new name must be assigned to the Taiban (b) meteorite used in this study in order to avoid confusion.

# REFERENCES CITED


Abe, N., Wakayama, M., and Ito, M. (1977) Absolute Raman intensities of liquids. Journal of Raman Spectroscopy, 6, 38-41.

Abedin, M.N., Bradley, A.T., Sharma, S.K., Misra, A.K., Lucey, P.G., McKay, C.P., Ismail, S., and Sandford, S.P. (2015) Mineralogy and astrobiology detection using laser remote sensing instrument. Applied Optics, 54, 7598-7611.

Acosta-Maeda, T.E., Misra, A.K., Gasda, P.J., and Sharma, S.K. (2014) Stand-off detection of amino acids and organics using a compact remote Raman instrument. 45th Lunar and Planetary Science Conference, The Woodlands, Texas, abstract# 2331.

Acosta-Maeda, T.E., Misra, A.K., Muzangwa, L.G., Berlanga, G., Muchow, D., Porter, J., and Sharma, S.K. (2016a) Remote Raman measurements of minerals, organics and inorganics at 430 meter range. Applied Optics (Submitted).

Acosta-Maeda, T.E., Misra, A.K., Porter, J.N., Bates, D.E., and Sharma, S.K. (2016b) Remote Raman efficiencies and cross-sections of organics and inorganic chemicals Applied Spectroscopy (In Press).

Acosta-Maeda, T.E., Misra, A.K., Sharma, S.K., Berlanga, G., Muchow, D., and Muzangwa, L. (2016c) Remote Raman measurements of minerals, organics and inorganics at 430 m range. 47th Lunar and Planetary Science Conference, The Woodlands, Texas, abstract# 3053.

Acosta-Maeda, T.E., Scott, E.R.D., Sharma, S.K., and Misra, A.K. (2013) The pressures and temperatures of meteorite impact: Evidence from micro-Raman mapping of mineral phases in the strongly shocked Taiban ordinary chondrite. American Mineralogist, 98, 859-869.

Acosta, T.E., Scott, E.R.D., and Sharma, S.K. (2012a) Micro-Raman mapping of mineral phases in the strongly shocked Taiban ordinary chondrite. 43rd Lunar and Planetary Science Conference, abstract# 2725.

Acosta, T.E., Scott, E.R.D., Sharma, S.K., and Misra, A.K. (2012b) Micro-Raman of mineral phases in the strongly shocked Taiban ordinary chondrite: ringwoodite coloration. European Planetary Science Congress, 364.

Agee, C.B., Li, J., Shannon, M.C., and Circone, S. (1995) Pressure-temperature phase diagram for the Allende meteorite. Journal of Geophysical Research: Solid Earth, 100, 17725-17740.

Aggarwal, R.L., Farrar, L.W., and Polla, D.L. (2010) Measurement of the absolute Raman scattering cross sections of sulfur and the standoff Raman detection of a 6-mm-thick sulfur specimen at 1500 m. Journal of Raman Spectroscopy, 42, 461-464.

Aggarwal, R.L., Farrar, L.W., Saikin, S.K., Andrade, X., Aspuru-Guzik, A., and Polla, D.L. (2012) Measurement of the absolute Raman cross section of the optical phonons in type Ia natural diamond. Solid State Communications, 152, 204-209.

Akaogi, M., Ross, N.L., McMillan, P., and Navrotsky, A. (1984) The $Mg_2SiO_4$ polymorphs (olivine, modified spinel and spinel); thermodynamic properties from oxide melt solution calorimetry, phase relations, and models of lattice vibrations. American Mineralogist, 69, 499-512.

Albrecht, A.C. (1961) On the theory of Raman intensities. The Journal of Chemical Physics, 34, 1476-1484.

Angel, S.M., Gomer, N.R., Sharma, S.K., and McKay, C. (2012) Remote Raman Spectroscopy for planetary exploration: A review. Applied Spectroscopy, 66, 137-150.

Angel, S.M., Kulp, T.J., and Vess, T.M. (1992) Remote-Raman spectroscopy at intermediate ranges using low-power CW lasers. Applied Spectroscopy, 46, 1085-1091.

Baran, E.J., Viera, I., and Torre, M.H. (2007) Vibrational spectra of the Cu(II) complexes of L-asparagine and L-glutamine. Spectrochimica Acta Part A: Molecular and Biomolecular Spectroscopy, 66, 114-117.

Beegle, L., and Bhartia, R. (2016) Scanning Habitable Environments with Raman & Luminescence for Organics & Chemicals (SHERLOC). Mars Future Rover Plans, NASA 2020 Launch. Available: http://mars.nasa.gov/mars2020/mission/science/for-scientists/instruments/sherloc/ (accessed June 16th, 2016). Jet Propulsion Laboratory, California Institute of Technology.

Berlanga, G., Acosta-Maeda, T.E., Misra, A.K., Sharma, S.K., and Flynn, L.P. (2015) Standoff Time-Resolved Fast Fluorescence of Organics and Amino Acids. 46th Lunar and Planetary Science Conference, Abstrac# 2613.

Bild, R.W., and Tallant, D.R. (1984) Raman microscopy of the Londran meteorite. Meteoritics, 19, 190.

Bini, R., Foggi, P., Salvi, P.R., and Schettino, V. (1990) FTIR study of vibrational relaxation in potassium perchlorate crystal. The Journal of Physical Chemistry, 94, 6653-6658.

Binns, R., Davis, R., and Reed, S. (1969) Ringwoodite, natural $(Mg,Fe)_2$ spinel in the Tenham meteorite. Nature, 221, 943-944.

Bischoff, W.D., Sharma, S.K., and MacKenzie, F.T. (1985) Carbonate ion disorder in synthetic and biogenic magnesian calcites; a Raman spectral study. American Mineralogist, 70, 581-589.

Blacksberg, J., Alerstam, E., Maruyama, Y., Cochrane, C.J., and Rossman, G.R. (2016) Miniaturized time-resolved Raman spectrometer for planetary science based on a fast single photon avalanche diode detector array. Applied Optics, 55, 739-748.

Botta, O., Martins, Z., and Ehrenfreund, P. (2007) Amino acids in Antarctic CM1 meteorites and their relationship to other carbonaceous chondrites. Meteoritics & Planetary Science, 42, 81-92.

Boyer, H., Smith, D., and Lasnier, B. (1985) Raman microprobe determination of natural and synthetic coesite. Physics and Chemistry of Minerals, 12, 45-48.

Bremer, M.T., and Dantus, M. (2014) Detecting micro-particles of explosives at ten meters using selective stimulated Raman scattering. CLEO: QELS_Fundamental Science, JTh2A. 5.

Brulé, T., Yockell-Lelièvre, H., Bouhélier, A., Margueritat, J., Markey, L., Leray, A., Dereux, A., and Finot, E. (2014) Sorting of enhanced reference Raman spectra of a single amino acid molecule. The Journal of Physical Chemistry C, 118, 17975-17982.

Bykov, S.V., Mao, M., Gares, K.L., and Ashera, S.A. (2015) Compact solid-state 213 nm laser enables standoff deep ultraviolet Raman spectrometer: measurements of Nitrate photochemistry. Applied Spectroscopy, 69, 895-901.

Cahill, J.E., and Leroi, G.E. (1969) Raman spectra of solid $CO_2$, $N_2O$, $N_2$, and CO. The Journal of Chemical Physics, 51, 1324-1332.

Callahan, M.P., Burton, A.S., Elsila, J.E., Baker, E.M., Smith, K.E., Glavin, D.P., and Dworkin, J.P. (2013) A search for amino acids and nucleobases in the Martian meteorite Roberts Massif 04262 using liquid chromatography-mass spectrometry. Meteoritics & Planetary Science, 48, 786-795.

Callahan, M.P., Smith, K.E., Cleaves, H.J., Ruzicka, J., Stern, J.C., Glavin, D.P., House, C.H., and Dworkin, J.P. (2011) Carbonaceous meteorites contain a wide range of extraterrestrial nucleobases. Proceedings of the National Academy of Sciences, 108, 13995-13998.

Cançado, L.G., Jorio, A., and Pimenta, M.A. (2007) Measuring the absolute Raman cross section of nanographites as a function of laser energy and crystallite size. Physical Review B, 76, 064304.

Capaccioni, F., Coradini, A., Filacchione, G., Erard, S., Arnold, G., Drossart, P., De Sanctis, M.C., Bockelee-Morvan, D., Capria, M.T., Tosi, F., Leyrat, C., Schmitt, B., Quirico, E., Cerroni, P., Mennella, V., Raponi, A., Ciarniello, M., McCord, T., Moroz, L., Palomba, E., Ammannito, E., Barucci, M.A., Bellucci, G., Benkhoff, J., Bibring, J.P., Blanco, A., Blecka, M., Carlson, R., Carsenty, U., Colangeli, L., Combes, M., Combi, M., Crovisier, J., Encrenaz, T., Federico, C., Fink, U., Fonti, S., Ip, W.H., Irwin, P., Jaumann, R., Kuehrt, E., Langevin, Y., Magni, G., Mottola, S., Orofino, V., Palumbo, P., Piccioni, G., Schade, U., Taylor, F., Tiphene, D., Tozzi, G.P., Beck, P., Biver, N., Bonal, L., Combe, J.-P., Despan, D., Flamini, E., Fornasier, S., Frigeri, A., Grassi, D., Gudipati, M., Longobardo, A., Markus, K., Merlin, F., Orosei, R., Rinaldi, G.,

Stephan, K., Cartacci, M., Cicchetti, A., Giuppi, S., Hello, Y., Henry, F., Jacquinod, S., Noschese, R., Peter, G., Politi, R., Reess, J.M., and Semery, A. (2015) The organic-rich surface of comet 67P/Churyumov-Gerasimenko as seen by VIRTIS/Rosetta. Science, 347.

Carey, D.M., and Korenowski, G.M. (1998) Measurement of the Raman spectrum of liquid water. The Journal of Chemical Physics, 108, 2669-2675.

Carlson, R.W., Calvin, W.M., Dalton, J.B., Hansen, G.B., Hudson, R.L., McCord, T.B., and Moore, M.H. (2009) Europa's surface composition. In R.T. Pappalardo, W.B. McKinnon, and K. Khurana, Eds. Europa, p. 283-328. University of Arizona Press.

Carter, J.C., Angel, S.M., Lawrence-Snyder, M., Scaffidi, J., Whipple, R.E., and Reynolds, J.G. (2005a) Standoff detection of high explosive materials at 50 meters in ambient light conditions using a small Raman instrument. Applied Spectroscopy, 59, 769-775.

Carter, J.C., Scaffidi, J., Burnett, S., Vasser, B., Sharma, S.K., and Angel, S.M. (2005b) Stand-off Raman detection using dispersive and tunable filter based systems. Spectrochimica Acta Part A: Molecular and Biomolecular Spectroscopy, 61, 2288-2298.

Chen, M., Chen, J., Xie, X., and Xu, J. (2007a) A microstructural investigation of natural lamellar ringwoodite in olivine of the shocked Sixiangkou chondrite. Earth and Planetary Science Letters, 264, 277-283.

Chen, M., and El Goresy, A. (2000) The nature of maskelynite in shocked meteorites: not diaplectic glass but a glass quenched from shock-induced dense melt at high pressures. Earth and Planetary Science Letters, 179, 489-502.

Chen, M., Li, H., Goresy, A.E.L., Liu, J., and Xie, X. (2006) Fracture-related intracrystalline transformation of olivine to ringwoodite in the shocked Sixiangkou meteorite. Meteoritics & Planetary Science, 41, 731-737.

Chen, M., Sharp, T.G., Goresy, A.E., Wopenka, B., and Xie, X. (1996) The Majorite-Pyrope + Magnesiowüstite Assemblage: Constraints on the History of Shock Veins in Chondrites. Science, 271, 1570-1573.

Chen, M., and Xie, X.D. (2008) Two distinct assemblages of high-pressure liquidus phases in shock veins of the Sixiangkou meteorite. Meteoritics & Planetary Science, 43, 823-828.

Chen, T., Madey, J.M.J., Price, F.M., Sharma, S.K., and Lienert, B. (2007b) Remote Raman Spectra of Benzene Obtained from 217 Meters Using a Single 532 nm Laser Pulse. Applied Spectroscopy, 61, 624-629.

Chopelas, A. (1991a) Single crystal Raman spectra of forsterite, fayalite, and monticellite. American Mineralogist, 76, 1101-1109.

Chopelas, A. (1991b) Thermal properties of β-$Mg_2SiO_4$ at mantle pressures derived from vibrational spectroscopy: Implications for the mantle at 400 km depth. Journal of Geophysical Research: Solid Earth, 96, 11817-11829.

Chopelas, A., Boehler, R., and Ko, T. (1994) Thermodynamics and behavior of c-$Mg_2SiO_4$ at high pressure: implications for $Mg_2SiO_4$ phase equilibrium. Physics and Chemistry of Minerals, 21, 351-359.

Clarkson, J., and Ewen Smith, W. (2003) A DFT analysis of the vibrational spectra of nitrobenzene. Journal of Molecular Structure, 655, 413-422.

Coleman, L.C. (1977) Ringwoodite and majorite in the Catherwood meteorite. Canadian Mineralogist, 15, 97-101.

Colthup, N.B., Daly, L.H., and Wiberley, S.E. (1990) Introduction to Infrared and Raman Spectroscopy, 3rd Edition. 547 p. Academic Press, Boston.

Cooney, J. (1965) Satellite observation using Raman component of laser backscatter. In Zirkind, Ed. Proceedings of the Symposium on Electromagnetic Sensing of the Earth from Satellites, p. 1. Polytechnic Press of the Polytechnic Institute, Brooklyn, New York.

Cooney, T.F., Scott, E.R.D., Krot, A.N., Sharma, S.K., and Yamaguchi, A. (1999) Vibrational spectroscopic study of minerals in the Martian meteorite ALH84001. American Mineralogist, 84, 1569.

Cornell, R.M., and Schwertmann, U. (2003) The Iron Oxides. Structure, Reactions, Ocurrences and Uses, 2nd Edition. Wiley-VCH Verlag GmbH & Co. KGaA, Weinheim.

Culka, A., Jehlička, J., and Edwards, H.G.M. (2010) Acquisition of Raman spectra of amino acids using portable instruments: Outdoor measurements and comparison. Spectrochimica Acta Part A: Molecular and Biomolecular Spectroscopy, 77, 978-983.

Cynn, H., Anderson, O.L., and Nicol, M. (1993) Effects of Cation Disordering in a Natural $MgAl_2O_4$ Spinel Observed by Rectangular Parallelepiped Ultrasonic Resonance and Raman Measurements. In R.C. Liebermann, and C.H. Sondergeld, Eds. Experimental Techniques in Mineral and Rock Physics: The Schreiber Volume, p. 415-444. Birkhäuser Basel, Basel.

Cynn, H., Sharma, S.K., Cooney, T.F., and Nicol, M. (1992) High-temperature Raman investigation of order-disorder behavior in the $MgAl_2O_4$ spinel. Physical Review B, 45, 500-502.

Damen, T.C., Leite, R.C.C., and Porto, S.P.S. (1965) Angular dependence of the Raman scattering from benzene excited by the He-Ne cw Laser. Physical Review Letters, 14, 9-11.

Dantus, M. (2014) Single-beam stimulated Raman scattering for sub-microgram standoff detection of explosives. Laser Science, LW5I. 1.

de Faria, D.L.A., Venâncio Silva, S., and de Oliveira, M.T. (1997) Raman microspectroscopy of some iron oxides and oxyhydroxides. Journal of Raman Spectroscopy, 28, 873-878.

Dean, K.J., and Wilkinson, G.R. (1985) Raman study of the symmetric $\nu_1$ vibrational mode of $N_3^-$ and $NO_3^-$ in aqueous solutions. Journal of Raman Spectroscopy, 16, 22-26.

Dirac, P.A.M. (1927) The quantum theory of dispersion. Proceedings of the Indian Academy of Science, Section A, 114, 710.

Dogariu, A. (2013) Standoff explosive detection and hyperspectral imaging using coherent anti-Stokes Raman spectroscopy. Laser Science, LTh4G. 4.

Du, P., Ma, L., Cao, Y., Li, D., Liu, Z., Wang, Z., and Sun, Z. (2014) Stable Ag@oxides nanoplates for surface-enhanced Raman spectroscopy of amino acids. ACS Applied Materials & Interfaces, 6, 8853-8858.

Dubessy, J., Caumon, M.-C., Rull, F., and Sharma, S. (2012) Instrumentation in Raman spectroscopy: elementary theory and practice. In J. Dubessy, M.-C. Caumon, and F. Rull, Eds. Raman Spectroscopy Applied to Earth Sciences and Cultural Heritage, EMU Notes in Mineralogy, Vol. 12, p. 83-172. European Mineralogical Union and the Mineralogical Society of Great Britain and Ireland.

Dudik, J.M., Johnson, C.R., and Asher, S.A. (1985) Wavelength dependence of the preresonance Raman cross sections of $CH_3CN$, $SO_4^{2-}$, $ClO_4^-$, and $NO_3^-$. The Journal of Chemical Physics, 82, 1732-1740.

Edwards, H.G.M., Hutchinson, I., and Ingley, R. (2012) The ExoMars Raman spectrometer and the identification of biogeological spectroscopic signatures using a flight-like prototype. Analytical and Bioanalytical Chemistry, 404, 1723-1731.

Elsila, J.E., Glavin, D.P., and Dworkin, J.P. (2009) Cometary glycine detected in samples returned by Stardust. Meteoritics & Planetary Science, 44, 1323-1330.

Faris, G.W., and Copeland, R.A. (1997) Wavelength dependence of the Raman cross section for liquid water. Applied Optics, 36, 2686-2688.

Feng, L., Lin, Y., Hu, S., Xu, L., and Miao, B. (2011) Estimating compositions of natural ringwoodite in the heavily shocked Grove Mountains 052049 meteorite from Raman spectra. American Mineralogist, 96, 1480-1489.

Ferraro, J.R., Nakamoto, K., and Brown, C.W. (2003) Introductory Raman Spectroscopy, 2nd Edition. Academic Press, San Diego.

Ferroir, T., Beck, P., Van de Moortèle, B., Bohn, M., Reynard, B., Simionovici, A., El Goresy, A., and Gillet, P. (2008) Akimotoite in the Tenham meteorite: Crystal

chemistry and high-pressure transformation mechanisms. Earth and Planetary Science Letters, 275, 26-31.

Fini, G. (2004) Applications of Raman spectroscopy to pharmacy. Journal of Raman Spectroscopy, 35, 335-337.

Fries, M., Sellar, G., Allwood, A., and Bhartia, R. (2011) Raman in a Combined Instrument Package: Co-Registered and "Smart Raman" Techniques. CORALS II, Abstract 4087.

Fritz, J., Greshake, A., and Stöffler, D. (2005) Micro-Raman spectroscopy of plagioclase and maskelynite in Martian meteorites: Evidence of progressive shock metamorphism. Antarctic meteorite research, 18, 96.

Frosch, T., Tarcea, N., Schmitt, M., Thiele, H., Langenhorst, F., and Popp, J. (2007) UV Raman imaging - A promising tool for astrobiology: comparative Raman studies with different excitation wavelengths on SNC Martian meteorites. Analytical Chemistry, 79, 1101-1108.

Frost, R.L., Kloprogge, J.T., and Martens, W.N. (2004) Raman spectroscopy of the arsenates and sulphates of the tsumcorite mineral group. Journal of Raman Spectroscopy, 35, 28-35.

Frost, R.L., Kristof, J., Rintoul, L., and Kloprogge, J.T. (2000) Raman spectroscopy of urea and urea-intercalated kaolinites at 77 K. Spectrochimica Acta Part A: Molecular and Biomolecular Spectroscopy, 56, 1681-1691.

Fulton, J. (2011) Remote detection of explosives using Raman spectroscopy. Proceedings of SPIE, 8018 Chemical, Biological, Radiological, Nuclear, and Explosives (CBRNE) Sensing XII, 80181A.

Furić, K., and Volovšek, V. (2010) Water ice at low temperatures and pressures: New Raman results. Journal of Molecular Structure, 976, 174-180.

Gaft, M., and Nagli, L. (2008) UV gated Raman spectroscopy for standoff detection of explosives. Optical Materials, 30, 1739-1746.

Galeener, F.L., and Geissberger, A.E. (1983) Vibrational dynamics in $^{30}$Si-substituted vitreous $SiO_2$. Physical Review B, 27, 6199-6204.

Gasda, P.J., Acosta-Maeda, T.E., Lucey, P.G., Misra, A.K., Sharma, S.K., and Taylor, G.J. (2015) Next generation laser-nased standoff spectroscopy techniques for Mars exploration. Applied Spectroscopy, 69, 173-192.

Giese, R.F. (1966) Crystal Structure of Kernite, $Na_2B_4O_6(OH)_2 \cdot 3H_2O$. Science, 154, 1453-1454.

Gillet, P., Chen, M., Dubrovinsky, L., and El Goresy, A. (2000) Natural $NaAlSi_3O_8$-hollandite in the shocked Sixiangkou meteorite. Science, 287, 1633-1636.

Gonzalez-Vilchez, F., and Griffith, W.P. (1972) Transition-metal tetra-oxo-complexes and their vibrational spectra. Journal of the Chemical Society, Dalton Transactions, 1416-1421.

Google Maps (2015) University of Hawai‘i at Mānoa. Available: https://www.google.com/maps/@21.2991617,-157.817062,17z (accessed June 2016).

Goryainov, S.V., Boldyreva, E.V., and Kolesnik, E.N. (2006) Raman observation of a new (ζ) polymorph of glycine? Chemical Physics Letters, 419, 496-500.

Graf, D., Molitor, F., Ensslin, K., Stampfer, C., Jungen, A., Hierold, C., and Wirtz, L. (2007) Spatially Resolved Raman Spectroscopy of Single- and Few-Layer Graphene. Nano Letters, 7, 238-242.

Griffith, W.P. (1969) Raman spectroscopy of minerals. Nature, 224, 264-266.

Gucsik, A., Koeberl, C., Brandstätter, F., Libowitzky, E., and Reimold, W.U. (2003) Scanning electron microscopy, cathodoluminescence, and Raman spectroscopy of experimentally shock-metamorphosed quartzite. Meteoritics & Planetary Science, 38, 1187-1197.

Gupta, S., and Goyal, S. (2011) Equation of State for $Mg_2SiO_4$ (alpha-forsterite, beta-wadsleyite and gamma-ringwoodite): ab-Initio. American Institute of Physics Conference Series. 1349, 200-201.

Hahn, D.W. (2007) Raman scattering theory. Available: http://plaza.ufl.edu/dwhahn/Raman%20Scattering%20Theory.pdf (accessed July 2016). Department of Mechanical and Aerospace Engineering, University of Florida.

Halvorson, K., and McHone, J.F. (1992) Vredefort coesite confirmed with Raman spectroscopy. Abstracts of the Lunar and Planetary Science Conference. 23, 477.

Hanesch, M. (2009) Raman spectroscopy of iron oxides and (oxy)hydroxides at low laser power and possible applications in environmental magnetic studies. Geophysical Journal International, 177, 941-948.

Hanlon, E., Manoharan, R., Koo, T.W., Shafer, K., Motz, J., Fitzmaurice, M., Kramer, J., Itzkan, I., Dasari, R., and Feld, M. (2000) Prospects for in vivo Raman spectroscopy. Physics in medicine and biology, 45, R1.

Harriss, K.H., and Burchell, M.J. (2016) A study of the observed shift in the peak position of olivine Raman spectra as a result of shock induced by hypervelocity impacts. Meteoritics & Planetary Science, published online, doi: 10.1111/maps.12660.

Harvey, P.D., and Butler, I.S. (1986) Raman spectra of orthorhombic sulfur at 40 K. Journal of Raman Spectroscopy, 17, 329-334.

Hazen, R.M., Downs, R.T., Finger, L.W., and Ko, J. (1993) Crystal chemistry of ferromagnesian silicate spinels; evidence for Mg-Si disorder. American Mineralogist, 78, 1320-1323.

Hemley, R.J., Mao, H.K., and Chao, E.C.T. (1986) Raman spectrum of natural and synthetic stishovite. Physics and Chemistry of Minerals, 13, 285-290.

Herzberg, G. (1945) Infrared and Raman Spectra of Polyatomic Molecules. 632 p. Van Nostrand Reinhold Company, New York.

Heymann, D. (1987) Raman spectra of carbon in the Canyon Diablo iron meteorite. Abstracts of the Lunar and Planetary Science Conference. 18, 419.

Hibben, J.H. (1939) The Raman Effect. Reinhold Publishing Co., New York.

Hirschfeld, T. (1974) Range independence of signal in variable focus remote Raman spectrometry. Applied Optics, 13, 1435-1437.

Hofmeister, A.M., Giesting, P.A., Wopenka, B., Gwanmesia, G.D., and Jolliff, B.L. (2004) Vibrational spectroscopy of pyrope-majorite garnets: Structural implications. American Mineralogist, 89, 132-146.

Hokr, B.H., Bixler, J.N., Noojin, G.D., Thomas, R.J., Rockwell, B.A., Yakovlev, V.V., and Scully, M.O. (2014) Single-shot stand-off chemical identification of powders using random Raman lasing. Proceedings of the National Academy of Sciences of the United States of America, 111, 12320-12324.

Hopkins, A.J., Cooper, J.L., Profeta, L.T., and Ford, A.R. (2016) Portable deep-ultraviolet (DUV) Raman for standoff Detection. Applied Spectroscopy, 70, 861-873.

Huang, E., Chen, C.H., Huang, T., Lin, E.H., and Xu, J.-A. (2000) Raman spectroscopic characteristics of Mg-Fe-Ca pyroxenes. American Mineralogist, 85, 473-479.

Iishi, K. (1978) Lattice dynamics of forsterite. American Mineralogist, 63, 1198-1208.

Isakov, D., Petukhova, D., Vasilev, S., Nuraeva, A., Khazamov, T., Seyedhosseini, E., Zelenovskiy, P., Shur, V.Y., and Kholkin, A.L. (2014) In situ observation of the humidity controlled polymorphic phase transformation in glycine microcrystals. Crystal Growth & Design, 14, 4138-4142.

Izake, E.L., Cletus, B., Olds, W., Sundarajoo, S., Fredericks, P.M., and Jaatinen, E. (2012) Deep Raman spectroscopy for the non-invasive standoff detection of concealed chemical threat agents. Talanta, 94, 342-347.

Jabłoński, A. (1933) Efficiency of anti-Stokes fluorescence in dyes. Nature, 131, 839-840.

Jenkins, A.L., Larsen, R.A., and Williams, T.B. (2005) Characterization of amino acids using Raman spectroscopy. Spectrochimica Acta Part A: Molecular and Biomolecular Spectroscopy, 61, 1585-1594.

Kalidasan, M., Asokan, K., Baskar, K., and Dhanasekaran, R. (2015) Effect of gamma ray irradiation on sodium borate single crystals. Radiation Physics and Chemistry, 117, 70-77.

Kamemoto, L.E., Misra, A.K., Sharma, S.K., Goodman, M.T., Luk, H., Dykes, A.C., and Acosta, T. (2010) Near-Infrared micro-Raman spectroscopy for in vitro detection of cervical cancer. Applied Spectroscopy, 64, 255-261.

Kashyap, S.C., Bhatti, K.P., Chaudhary, S., Pandya, D.K., and Sharma, S.K. (2009) Chemically synthesized ferromagnetic $Zn_{1-x}Co_xO$ nanocrystals: Raman investigations. Synthesis and Reactivity in Inorganic, Metal-Organic, and Nano-Metal Chemistry, 39, 216-220.

Keppler, H., and Smyth, J.R. (2005) Optical and near infrared spectra of ringwoodite to 21.5 GPa: Implications for radiative heat transport in the mantle. American Mineralogist, 90, 1209-1212.

Kerschhofer, L., Dupas, C., Liu, M., Sharp, T.G., Durham, W.B., and Rubie, D.C. (1998) Polymorphic transformations between olivine, wadsleyite and ringwoodite: mechanisms of intracrystalline nucleation and the role of elastic strain. Mineralogical Magazine, 62, 617-638.

Kerschhofer, L., Rubie, D.C., Sharp, T.G., McConnell, J.D.C., and Dupas-Bruzek, C. (2000) Kinetics of intracrystalline olivine–ringwoodite transformation. Physics of the Earth and Planetary Interiors, 121, 59-76.

Kerschhofer, L., Sharp, T.G., and Rubie, D.C. (1996) Intracrystalline Transformation of Olivine to Wadsleyite and Ringwoodite Under Subduction Zone Conditions. Science, 274, 79-81.

Kettle, S.F.A. (1982) Final Report: The Raman Spectra of Phase III Ammonium Nitrate, p. 23.

Khare, B.N., Sagan, C., Ogino, H., Nagy, B., Er, C., Schram, K.H., and Arakawa, E.T. (1986) Amino acids derived from Titan tholins. Icarus, 68, 176-184.

Kiefert, L., and Karampelas, S. (2011) Use of the Raman spectrometer in gemmological laboratories: Review. Spectrochimica Acta Part A: Molecular and Biomolecular Spectroscopy, 80, 119-124.

Klein, V., Popp, J., Tarcea, N., Schmitt, M., Kiefer, W., Hofer, S., Stuffler, T., Hilchenbach, M., Doyle, D., and Dieckmann, M. (2004) Remote Raman spectroscopy as a prospective tool for planetary surfaces. Journal of Raman Spectroscopy, 35, 433-440.

Kleppe, A.K., Jephcoat, A.P., Smyth, J.R., and Frost, D.J. (2002a) On protons, iron and the high-pressure behavior of ringwoodite. Geophysical Research Letters, 29, 17-1-17-4.

Kleppe, K.A., Jephcoat, P.A., and Smyth, R.J. (2002b) Raman spectroscopic study of hydrous $\gamma$-$Mg_2SiO_4$ to 56.5 GPa. Physics and Chemistry of Minerals, 29, 473-476.

Koshizuka, N., Yokoyama, Y., Hiruma, H., and Tsushima, T. (1975) Resonance Raman scattering in $CdIn_2S_4$. Solid State Communications, 16, 1011-1014.

Kramers, H.A., and Heisenberg, W. (1925) Über die Streuung von Strahlung durch Atome. Zeitschrift für Physik, 31, 681-708.

Kubo, T., Kimura, M., Kato, T., Nishi, M., Tominaga, A., Kikegawa, T., and Funakoshi, K.-i. (2010) Plagioclase breakdown as an indicator for shock conditions of meteorites. Nature Geosci, 3, 41-45.

Kubo, T., Ohtani, E., and Funakoshi, K.-i. (2004) Nucleation and growth kinetics of the α-β transformation in $Mg_2SiO_4$ determined by in situ synchrotron powder X-ray diffraction. American Mineralogist, 89, 285-293.

Kuebler, K.E., Jolliff, B.L., Wang, A., and Haskin, L.A. (2006) Extracting olivine (Fo–Fa) compositions from Raman spectral peak positions. Geochimica et Cosmochimica Acta, 70, 6201-6222.

Lam, P.K., Yu, R., Lee, M.W., and Sharma, S.K. (1990) Structural distortions and vibrational modes in $Mg_2SiO_4$. American Mineralogist, 75, 109-119.

Landsberg, G., and Mandelstam, L. (1928) Eine neue Erscheinung bei der Lichtzerstreuung in Krystallen. Naturwissenschaften, 16, 557-558.

Lange, D.E., Keil, K., and LaPaz, L. (1980) Catalog of the Meteorite Collection of the Institute of Meteoritics at the University of New Mexico.

Le Ru, E.C., Schroeter, L.C., and Etchegoin, P.G. (2012) Direct Measurement of Resonance Raman Spectra and Cross Sections by a Polarization Difference Technique. Analytical Chemistry, 84, 5074-5079.

Lin, Q., Niu, G., Wang, Q., Yu, Q., and Duan, Y. (2013) Combined laser-induced breakdown with Raman spectroscopy: historical technology development and recent applications. Applied Spectroscopy Reviews, 48, 487-508.

Lingemann, C., and Stöffler, D. (1998) New evidence for the colouration and formation of ringwoodite in severely shocked chondrites. Lunar and Planetary Science Conference. 29, Abstract# 1308.

Liu, L.-G. (1978) High-pressure phase transformations of albite, jadeite and nepheline. Earth and Planetary Science Letters, 37, 438-444.

Liu, L.-g., Lin, C.C., Yung, Y., Mernagh, T., and Irifune, T. (2009) Raman spectroscopic study of K-lingunite at various pressures and temperatures. Physics and Chemistry of Minerals, 36, 143-149.

Loeffen, P.W., Maskall, G., Bonthron, S., Bloomfield, M., Tombling, C., and Matousek, P. (2011) Spatially offset Raman spectroscopy (SORS) for liquid screening. SPIE. 8189, 81890C.

Lopez-Reyes, G., Rull, F., Venegas, G., Westall, F., Foucher, F., Bost, N., Sanz, A., Catalá-Espí, A., Vegas, A., Hermosilla, I., Sansano, A., and Medina, J. (2013) Analysis of

the scientific capabilities of the ExoMars Raman Laser Spectrometer instrument. European Journal of Mineralogy, 25, 721-733.

-. (2014) Analysis of the scientific capabilities of the ExoMars Raman Laser Spectrometer instrument. European Journal of Mineralogy, 25, 721-733.

Lutz, H.D., Becker, R.A., Eckers, W., Hölscher, B.G., and Berthold, H.J. (1983) Raman and IR spectra of the potassium, rubidium, and cesium perchlorates in the orthorhombic low-temperature modifications (baryte-type) and in the cubic high-temperature phases (sodium chloride-type with orientationally disordered perchlorate ions). Spectrochimica Acta A, 39, 7-14.

Lutz, H.D., Müller, B., and Steiner, H.J. (1991) Lattice vibration spectra. LIX. Single crystal infrared and Raman studies of spinel type oxides. Journal of Solid State Chemistry, 90, 54-60.

Madon, M., and Poirier, J.P. (1983) Transmission electron microscope observation of α, β and γ (Mg, Fe)$_2$SiO$_4$ in shocked meteorites: planar defects and polymorphic transitions. Physics of the Earth and Planetary Interiors, 33, 31-44.

Malavergne, V., Guyot, F., Benzerara, K., and Martinez, I. (2001) Description of new shock-induced phases in the Shergotty, Zagami, Nakhla and Chassigny meteorites. Meteoritics & Planetary Science, 36, 1297-1305.

Mammone, J.F., Sharma, S.K., and Nicol, M. (1980) Raman spectra of methanol and ethanol at pressures up to 100 kbar. The Journal of Physical Chemistry, 84, 3130-3134.

Manghnani, M.H., Vijayakumar, V., and Bass, J.D. (1998) High-Pressure Raman Scattering Study of Majorite-Garnet Solid Solutions in the System $Mg_4Si_4O_{12}$—$Mg_3Al_2Si_3O_{12}$. In M.H. Manghnani, and T. Yagi, Eds. Properties of Earth and Planetary Materials at High Pressure and Temperature, p. 129-137. American Geophysical Union, Washington, D.C.

Manov, G.G., DeLollis, N.J., and Acree, S.F. (1944) Ionization constant of boric acid and the pH of certain borax-chloride buffer solutions from 0 degrees to 60 degrees C. Journal of Research of the National Bureau of Standards, 33, 287-306.

Mao, H., Bell, P., and Boctor, N. (1982) The mineral chemistry of majorite in L6 chondrites. Carnegie Instute of Washington Yearbook, 81, 279-281.

Mary, Y.S., Ushakumari, L., Harikumar, B., Varghese, H.T., and Panicker, C.Y. (2009) FT-IR, FT-raman and SERS spectra of L-proline. Journal of the Iranian Chemical Society, 6, 138-144.

Mathies, R.A., Smith, S.O., and Palings, I. (1987) Determination of retinal chromophore structure in rhodopsins. In T.G. Spiro, Ed. Biological Applications of Raman Spectroscopy: Vol 2 - Resonance Raman Spectra of Polyenes and Aromatics, p. 59-108. John Wiley and Sons, New York.

McClung, F.J., and Weiner, D. (1964) Measurement of Raman Scattering Cross Sections for Use in Calculating Stimulated Raman Scattering Effects. Journal of the Optical Society of America, 54, 641-641.

McCreery, R.L. (2000) Raman Spectroscopy for Chemical Analysis. John Wiley & Sons, Inc.

-. (2002) Photometric Standards for Raman Spectroscopy. In J.M. Chalmers, and P.R. Griffiths, Eds. Handbook of Vibrational Spectroscopy, p. 1-13. John Wiley & Sons, Ltd, Chichester.

McKinnon, W.B., and Zolensky, M.E. (2003) Sulfate content of Europa's ocean and shell: evolutionary considerations and some geological and astrobiological implications. Astrobiology, 3, 879-897.

McMillan, P., Akaogi, M., Ohtani, E., Williams, Q., Nieman, R., and Sato, R. (1989) Cation disorder in garnets along the $Mg_3Al_2Si_3O_{12}$-$Mg_4Si_4O_{12}$ join: an infrared, Raman and NMR study. Physics and Chemistry of Minerals, 16, 428-435.

McMillan, P.F., and Akaogi, M. (1987) Raman spectra of β-$Mg_2SiO_4$ (modified spinel) and gamma-$Mg_2SiO_4$ (spinel). American Mineralogist, 72, 361-364.

Measures, R.M. (1992) Laser-Remote-Sensor Equations. Laser Remote Sensing, Fundamentals and Applications, p. 237-280. Krieger Publishing company, Florida.

Menzies, A.C. (1930) The Raman effect. Nature, 125, 205-207.

Misra, A.K., Sharma, S.K., Acosta, T.E., and Bates, D.E. (2011) Compact remote Raman and LIBS system for detection of minerals, water, ices and atmospheric gases for planetary exploration. Proceedings of SPIE, 8032, 80320Q

Misra, A.K., Sharma, S.K., Acosta, T.E., Porter, J.N., and Bates, D.E. (2012) Single-Pulse Standoff Raman Detection of Chemicals from 120 m Distance During Daytime. Applied Spectroscopy, 66, 1279-1285.

Misra, A.K., Sharma, S.K., Chio, C.H., Lucey, P.G., and Lienert, B. (2005) Pulsed remote Raman system for daytime measurements of mineral spectra. Spectrochimica Acta Part A: Molecular and Biomolecular Spectroscopy, 61, 2281-2287.

Misra, A.K., Sharma, S.K., and Lucey, P.G. (2006) Remote Raman Spectroscopic Detection of Minerals and Organics Under Illuminated Conditions from a Distance of 10 m Using a Single 532 nm Laser Pulse. Applied Spectroscopy, 60, 223-228.

Misra, A.K., Sharma, S.K., Lucey, P.G., Lentz, R.C.F., and Chio, C.H. (2007) Daytime rapid detection of minerals and organics from 50 and 100 m distances using a remote Raman system. Proceedings of SPIE, 6681, Lidar Remote Sensing for Environmental Monitoring VIII, 66810C.

Miyahara, M., El Goresy, A., Ohtani, E., Nagase, T., Nishijima, M., Vashaei, Z., Ferroir, T., Gillet, P., Dubrovinsky, L., and Simionovici, A. (2008) Evidence for fractional crystallization of wadsleyite and ringwoodite from olivine melts in chondrules

entrained in shock-melt veins. Proceedings of the National Academy of Sciences, 105, 8542-8547.

Miyahara, M., Ohtani, E., Yamaguchi, A., Ozawa, S., Sakai, T., and Hirao, N. (2014) Discovery of coesite and stishovite in eucrite. Proceedings of the National Academy of Sciences of the United States of America, 111, 10939-10942.

Moore, D.S., and Scharff, R.J. (2009) Portable Raman explosives detection. Analytical and Bioanalytical Chemistry, 393, 1571-1578.

Moreno, T., Morán López, M.A., Huerta Illera, I., Piqueras, C.M., Sanz Arranz, A., García Serna, J., and Cocero, M.J. (2011) Quantitative Raman determination of hydrogen peroxide using the solvent as internal standard: Online application in the direct synthesis of hydrogen peroxide. Chemical Engineering Journal, 166, 1061-1065.

Mori, H. (1994) Shock-induced phase transformations of the Earth and planetary materials. Journal of the Mineralogical Society of Japan, 23, 171-178.

Moros, J., and Laserna, J.J. (2011) New Raman-laser-induced breakdown spectroscopy identity of explosives using parametric data fusion on an integrated sensing platform. Analytical Chemistry, 83, 6275-6285.

Moros, J., Lorenzo, J.A., and Laserna, J.J. (2011) Standoff detection of explosives: critical comparison for ensuing options on Raman spectroscopy–LIBS sensor fusion. Analytical and Bioanalytical Chemistry, 400, 3353-3365.

Moros, J., Lorenzo, J.A., Novotný, K., and Laserna, J.J. (2013) Fundamentals of stand-off Raman scattering spectroscopy for explosive fingerprinting. Journal of Raman Spectroscopy, 44, 121-130.

Mosenfelder, J.L., Marton, F.C., Ross Ii, C.R., Kerschhofer, L., and Rubie, D.C. (2001) Experimental constraints on the depth of olivine metastability in subducting lithosphere. Physics of the Earth and Planetary Interiors, 127, 165-180.

Movasaghi, Z., Rehman, S., and Rehman, I.U. (2007) Raman spectroscopy of biological tissues. Applied Spectroscopy Reviews, 42, 493-541.

Murli, C., Vasanthi, R., and Sharma, S.M. (2006) Raman spectroscopic investigations of DL-serine and DL-valine under pressure. Chemical Physics, 331, 77-84.

Mustard, J.F., Adler, M., Allwood, A., Bass, D.S., Beaty, D.W., III, J.F.B., Brinckerhoff, W.B., Carr, M., Marais, D.J.D., Drake, B., Edgett, K.S., Eigenbrode, J., Elkins-Tanton, L.T., Grant, J.A., Milkovich, S.M., Ming, D., Moore, C., Murchie, S., Onstott, T.C., Ruff, S.W., Sephton, M.A., Steele, A., and Treiman, A. (2013) Report of the Mars 2020 Science Definition Team, 154 pp., posted July, 2013, by the Mars Exploration Program Analysis Group (MEPAG) at http://mepag.jpl.nasa.gov/reports/MEP/Mars_2020_SDT_Report_Final.pdf.

Nagli, L., Gaft, M., Fleger, Y., and Rosenbluh, M. (2008) Absolute Raman cross-sections of some explosives: Trend to UV. Optical Materials, 30, 1747-1754.

Nagy, S., Bérczi, S., Józsa, S., Gucsik, A., and Veres, M. (2010a) Olivine and pyroxene high-pressure polymorphs in melt veins of the strongly shocked NWA 5011 meteorite sample. Lunar and Planetary Science Conference XLI, Abstract# 1228.

Nagy, S., Gyollai, I., Józsa, S., and Bérczi, S. (2011) Observation of colouration of ringwoodite in the NWA 5011 L5-6 Chondrite. Lunar and Planetary Science Conference XLII, Abstract# 1285.

Nagy, S., Józsa, S., Bérczi, S., Gucsik, A., Koós, M., and Veres, M. (2010b) Shock induced high-pressure phases in the shock veins of NWA 5011 L6 chondrite. The 33rd Symposium on Antarctic Meteorites, National Institute of Polar Research, Tachikawa City, Tokyo, Japan.

Nakamura-Messenger, K., Connolly Jr., H.C., Lauretta, D.S., and OSIRIS-REx Science Team (2014) Strategy for ranking the science value of the surface of asteroid 101955 Bennu for sample site selection for OSIRIX-REx. LPSC XLV, The Woodlands, Texas, Abstract #2023.

Neish, C.D., Somogyi, Á., and Smith, M.A. (2010) Titan's primordial soup: Formation of amino acids via low-temperature hydrolysis of tholins Astrobiology, 10, 337-347.

Nieuwoudt, M.K., Comins, J.D., and Cukrowski, I. (2011) The growth of the passive film on iron in 0.05 M NaOH studied in situ by Raman micro-spectroscopy and electrochemical polarisation. Part I: near-resonance enhancement of the Raman spectra of iron oxide and oxyhydroxide compounds. Journal of Raman Spectroscopy, 42, 1335-1339.

Ohtani, E., Kimura, Y., Kimura, M., Takata, T., Kondo, T., and Kubo, T. (2004) Formation of high-pressure minerals in shocked L6 chondrite Yamato 791384: constraints on shock conditions and parent body size. Earth and Planetary Science Letters, 227, 505-515.

Otto, C., van den Tweel, T.J.J., de Mul, F.F.M., and Greve, J. (1986) Surface-enhanced Raman spectroscopy of DNA bases. Journal of Raman Spectroscopy, 17, 289-298.

Pasteris, J.D., Freeman, J.J., Goffredi, S.K., and Buck, K.R. (2001) Raman spectroscopic and laser scanning confocal microscopic analysis of sulfur in living sulfur-precipitating marine bacteria. Chemical Geology, 180, 3-18.

Pearce, B.K.D., and Pudritz, R.E. (2015) Seeding the pregenetic Earth: Meteoritic abundances of nucleobases and potential reaction pathways. The Astrophysical Journal, 807, 85.

Petry, R., Schmitt, M., and Popp, J. (2003) Raman spectroscopy—a prospective tool in the life sciences. ChemPhysChem, 4, 14-30.

Pettersson, A., Wallin, S., Östmark, H., Ehlerding, A., Johansson, I., Nordberg, M., Ellis, H., and Al-Khalili, A. (2010) Explosives standoff detection using Raman spectroscopy: from bulk towards trace detection. Proceedings of SPIE. 7664, 76641K.

Potgieter-Vermaak, S.S., Potgieter, J.H., Belleil, M., DeWeerdt, F., and Van Grieken, R. (2006) The application of Raman spectrometry to the investigation of cement: Part II: A micro-Raman study of OPC, slag and fly ash. Cement and Concrete Research, 36, 663-670.

Price, G.D., Putnis, A., and Agrell, S.O. (1979) Electron petrography of shock-produced veins in the Tenham chondrite. Contributions to Mineralogy and Petrology, 71, 211-218.

Price, G.D., Putnis, A., Agrell, S.O., and Smith, D.G.W. (1983 ) Wadsleyite, natural β-$(Mg,Fe)_2SiO_4$ from the Peace River meteorite. Canadian Mineralogist, 21, 29–35.

Price, G.D., Putnis, A., and Smith, D.G.W. (1982) A spinel to [beta]-phase transformation mechanism in $(Mg,Fe)_2SiO_4$. Nature, 296, 729-731.

Putnis, A., and Price, G.D. (1979) High-pressure $(Mg,Fe)_2SiO_4$ phases in the Tenham chondritic meteorite. Nature, 280, 217-218.

Pye, C.C., and Rudolph, W.W. (2003) An ab Initio, Infrared, and Raman Investigation of Phosphate Ion Hydration. The Journal of Physical Chemistry A, 107, 8746-8755.

Raman, C.V., and Krishnan, K.S. (1928) A new type of secondary radiation. Nature, 121, 501-502.

Ramdas, A.K. (1953) The Infra-Red Absorption Spectrum of Potassium Chlorate Crystals - Part II. Proceedings of the Indian Academy Of Science, Section A, 36, 55-60.

Ramírez-Cedeño, M.L., Ortiz-Rivera, W., Pacheco-Londoño, L.C., and Hernández-Rivera, S.P. (2010) Remote detection of hazardous liquids concealed in glass and plastic containers. Sensors Journal, IEEE, 10, 693-698.

Rauch, M., Keppler, H., Hafner, W., Poe, B., and Wokaun, A. (1996) A pressure-induced phase transition in $MgSiO_3$-rich garnet revealed by Raman spectroscopy. American Mineralogist, 81, 1289-1292.

Rayleigh, L. (1899) On the transmission of light through an atmosphere containing small particles in suspension, and on the origin of the blue of the sky. Philosophical Magazine Series 5, 47, 375-384.

Raymond, S.N. (2010) Formation of terrestrial planets. In R. Barnes, Ed. Formation and Evolution of Exoplanets. Wiley, Weinheim, Germany.

Ringwood, A.E. (1975) Composition and petrology of the Earth's mantle. McGraw-Hill, London.

Robinson, E.A. (1963) Characteristic vibrational frequencies of oxygen compounds of phosphorus and chlorine: correlation of symmetric and asymmetric stretching frequencies of PO and ClO bonds. Canadian Journal of Chemistry, 41, 173-179.

Ross, S.D. (1962) Forbidden transitions in the infra-red spectra of some tetrahedral anions—I. perchlorates. Spectrochimica Acta, 18, 225-228.

Rousseau, D.L., Miller, R.E., and Leroi, G.E. (1968) Raman Spectrum of Crystalline Sodium Nitrate. The Journal of Chemical Physics, 48, 3409-3413.

Rull, F., Martinez-Frias, J., and Rodríguez-Losada, J.A. (2007) Micro-Raman spectroscopic study of El Gasco pumice, western Spain. Journal of Raman Spectroscopy, 38, 239-244.

Rull, F., and Sobrón, F. (1994) Band profile analysis of the Raman spectra of sulphate ions in aqueous solutions. Journal of Raman Spectroscopy, 25, 693-698.

Rull, F., Vegas, A., Sansano, A., and Sobron, P. (2011) Analysis of arctic ices by remote Raman spectroscopy. Spectrochimica Acta Part A: Molecular and Biomolecular Spectroscopy, 80, 148-155.

Rull Perez, F., Edwards, H., Rivas, A., and Drummond, L. (1999) Fourier transform Raman spectroscopic characterization of pigments in the mediaeval frescoes at Convento de la Peregrina, Sahagun, Léon, Spain. Part 1—preliminary study. Journal of Raman Spectroscopy, 30, 301-305.

Rull Pérez, F., and Martinez-Frias, J. (2006) Raman spectroscopy goes to Mars. Spectroscopy Europe, 18, 18-21.

Rull Perez, F., and Maurice, S. (2016) The ExoMars rover instrument suite. RLS - Raman Spectrometer. Available: http://exploration.esa.int/mars/45103-rover-instruments/?fbodylongid=2130 (accessed June 16th, 2016). European Space Agency.

Sakamoto, K., Mizutani, G., and Ushioda, S. (1993) Absolute Raman-scattering cross section of a surface-adsorbed layer: Amorphous nitrobenzene on Ni(111). Physical Review B, 48, 8993-9005.

Sato, Y., and Nakamura, N. (2010) Shock melt veins of Tenham chondrite as a possible paleomagnetic recorder: Rock magnetism and high-pressure minerals. Geochem. Geophys. Geosyst., 11, Q04Z16.

Sazonova, L., Fel'dman, V., Kozlov, E., Dubrovinskaya, N., and Dubrovinskii, L. (2006) Genesis of ringwoodite during metamorphism induced by impact waves: Experimental data. Geochemistry International, 44, 137-142.

Scaffidi, J.P., Gregas, M.K., Lauly, B., Carter, J.C., Angel, S.M., and Vo-Dinh, T. (2010) Trace Molecular Detection via Surface-Enhanced Raman Scattering and Surface-Enhanced Resonance Raman Scattering at a Distance of 15 Meters. Applied Spectroscopy, 64, 485-492.

Schomacker, K.T., Delaney, J.K., and Champion, P.M. (1986) Measurements of the absolute Raman cross sections of benzene. The Journal of Chemical Physics, 85, 4240-4247.

Schrödinger, E. (1926) Quantisierung als Eigenwertproblem. Annalen der Physik, 386, 109-139.

Schrötter, H.W., and Klöckner, H.W. (1979) Raman Scattering Cross Sections in Gases and Liquids. In A. Weber, Ed. Raman Spectroscopy of Gases and Liquids, p. 123-166. Springer Berlin Heidelberg, Berlin, Heidelberg.

Scott, E.R.D., Sharma, K.S., and Chio, C.H. (2004) Micro-Raman and petrologic study of shock-induced high-pressure minerals in the Taiban meteorite. GEORAMAN 2004: 6th International Conference on Raman spectroscopy Applied to the Earth and Planetary Sciences, Honolulu, Hawai‘i, USA, 61–62.

Sharma, S.K., Angel, S.M., Ghosh, M., Hubble, H.W., and Lucey, P.G. (2002) Remote pulsed laser Raman spectroscopy system for mineral analysis on planetary surfaces to 66 meters. Applied Spectroscopy, 56, 699-705.

Sharma, S.K., Cooney, T.F., Wang, Z., and van der Laan, S. (1997) Raman band assignments of silicate and germanate glasses using high-pressure and high-temperature spectral data. Journal of Raman Spectroscopy, 28, 697-709.

Sharma, S.K., Lucey, P.G., Ghosh, M., Hubble, H.W., and Horton, K.A. (2003) Stand-off Raman spectroscopic detection of minerals on planetary surfaces. Spectrochimica Acta Part A: Molecular and Biomolecular Spectroscopy, 59, 2391-2407.

Sharma, S.K., Misra, A.K., Clegg, S.L., Barefield, J.E., Wiens, R.C., and Acosta, T. (2010) Time-resoved remote Raman study of minerals under supercritical $CO_2$ and high temperatures relevant to Venus exploration Philosophical Transactions of the Royal Society A, 368, 3167-3191.

Sharma, S.K., Misra, A.K., Clegg, S.M., Barefield, J.E., Wiens, R.C., Acosta, T.E., and Bates, D.E. (2011) Remote-Raman spectroscopic study of minerals under supercritical $CO_2$ relevant to Venus exploration. Spectrochimica Acta Part A: Molecular and Biomolecular Spectroscopy, 80, 75-81.

Sharma, S.K., Misra, A.K., Lucey, P.G., Angel, S.M., and McKay, C.P. (2006) Remote pulsed Raman spectroscopy of inorganic and organic materials to a radial distance of 100 meters. Applied Spectroscopy, 60, 871-876.

Sharma, S.K., Misra, A.K., Lucey, P.G., and Lentz, R.C.F. (2009) A combined remote Raman and LIBS instrument for characterizing minerals with 532 nm laser excitation. Spectrochimica Acta Part A: Molecular and Biomolecular Spectroscopy, 73, 468-476.

Sharma, S.K., Misra, A.K., Lucey, P.G., Wiens, R.C., and Clegg, S.M. (2007) Combined remote LIBS and Raman spectroscopy at 8.6 m of sulfur-containing minerals, and

minerals coated with hematite or covered with basaltic dust. Spectrochimica Acta Part A: Molecular and Biomolecular Spectroscopy, 68, 1036-1045.

Sharma, S.K., Simons, B., and Yoder, H.S. (1983) Raman study of anorthite, calcium Tschermak's pyroxene, and gehlenite in crystalline and glassy states. American Mineralogist, 68, 1113-1125.

Sharp, T.G., and De Carli, P.S. (2006) Shock effects in meteorites. p. 653–677. . In D.S. Lauretta, and H.Y. McSween Jr., Eds. Meteorites and the Early Solar System II. University of Arizona Press, Tucson.

Sharp, T.G., Lingemann, C.M., Dupas, C., and Stöffler, D. (1997) Natural Occurrence of $MgSiO_3$-Ilmenite and Evidence for MgSiO3-Perovskite in a Shocked L Chondrite. Science, 277, 352-355.

Sharp, T.G., Trickey, R., Xie, Z., and Decarli, P.S. (2009) Ringwoodite microstructures in L-chondrites RC106 and Acfer 040: implications for transformation mechanisms. Lunar and Planetary Science Conference XL, Abstract# 2541.

Sherman, D.M., and Waite, T.D. (1985) Electronic spectra of $Fe^{3+}$ oxides and oxide hydroxides in the near IR to near UV. American Mineralogist, 70, 1262-1269.

Shim, S., Stuart, C.M., and Mathies, R.A. (2008) Resonance Raman Cross-Sections and Vibronic Analysis of Rhodamine 6G from Broadband Stimulated Raman Spectroscopy. ChemPhysChem, 9, 697-699.

Shimanouchi, T. (1972) Tables of Molecular Vibrational Frequencies Consolidated, Volume I. 160 p. National Bureau of Standards.

Silva, W.R., Keller, E.L., and Frontiera, R.R. (2014) Determination of Resonance Raman Cross-Sections for Use in Biological SERS Sensing with Femtosecond Stimulated Raman Spectroscopy. Analytical Chemistry, 86, 7782-7787.

Sinogeikin, S.V., Bass, J.D., and Katsura, T. (2003) Single-crystal elasticity of ringwoodite to high pressures and high temperatures: implications for 520 km seismic discontinuity. Physics of the Earth and Planetary Interiors, 136, 41-66.

Sjöberg, B., Foley, S., Cardey, B., and Enescu, M. (2014) An experimental and theoretical study of the amino acid side chain Raman bands in proteins. Spectrochimica Acta Part A: Molecular and Biomolecular Spectroscopy, 128, 300-311.

Skinner, J.G., and Nilsen, W.G. (1968) Absolute Raman Scattering Cross-Section Measurement of the 992 $cm^{-1}$ Line of Benzene. Journal of the Optical Society of America, 58, 113-119.

Smekal, A. (1923) Zur Quantentheorie der Dispersion. Naturwissenschaften, 11, 873-875.

Smith, J.V., and Mason, B. (1970) Pyroxene-Garnet Transformation in Coorara Meteorite. Science, 168, 832-833.

Spiro, T.G., Smulevich, G., and Su, C. (1990) Probing protein structure and dynamics with resonance Raman spectroscopy: cytochrome c peroxidase and hemoglobin. Biochemistry, 29, 4497-4508.

Sprowles, J.C., and Plane, R.A. (1975) Raman spectrophotometric study of aqueous chlorate solutions. The Journal of Physical Chemistry, 79, 1711-1716.

Squyres, S.W., Arvidson, R.E., Bell, J.F., Calef, F., Clark, B.C., Cohen, B.A., Crumpler, L.A., de Souza, P.A., Farrand, W.H., Gellert, R., Grant, J., Herkenhoff, K.E., Hurowitz, J.A., Johnson, J.R., Jolliff, B.L., Knoll, A.H., Li, R., McLennan, S.M., Ming, D.W., Mittlefehldt, D.W., Parker, T.J., Paulsen, G., Rice, M.S., Ruff, S.W., Schröder, C., Yen, A.S., and Zacny, K. (2012) Ancient impact and aqueous processes at Endeavour Crater, Mars. Science, 336, 570-576.

Stebbins, J.F., Smyth, J.R., Panero, W.R., and Frost, D.J. (2009) Forsterite, hydrous and anhydrous wadsleyite and ringwoodite ($Mg_2SiO_4$): $^{29}Si$ NMR results for chemical shift anisotropy, spin-lattice relaxation, and mechanism of hydration. American Mineralogist, 94, 905-915.

Steele, A., Fries, M.D., Amundsen, H.E.F., Mysen, B.O., Fogel, M.L., Schweizer, M., and Boctor, N.Z. (2007) Comprehensive imaging and Raman spectroscopy of carbonate globules from Martian meteorite ALH 84001 and a terrestrial analogue from Svalbard. Meteoritics & Planetary Science, 42, 1549-1566.

Steele, A., McCubbin, F.M., Fries, M., Kater, L., Boctor, N.Z., Fogel, M.L., Conrad, P.G., Glamoclija, M., Spencer, M., Morrow, A.L., Hammond, M.R., Zare, R.N., Vicenzi, E.P., Siljeström, S., Bowden, R., Herd, C.D.K., Mysen, B.O., Shirey, S.B., Amundsen, H.E.F., Treiman, A.H., Bullock, E.S., and Jull, A.J.T. (2012) A Reduced Organic Carbon Component in Martian Basalts. Science, 337, 212-215.

Stein, L., and Appelman, E.H. (1983) Raman spectra of potassium perchlorate and potassium perbromate in anhydrous hydrogen fluoride and the acid strengths of perchloric and perbromic acids. Inorganic Chemistry, 22, 3017-3020.

Stöffler, D., Keil, K., and Edward R.D, S. (1991) Shock metamorphism of ordinary chondrites. Geochimica et Cosmochimica Acta, 55, 3845-3867.

Stokes, G.G. (1852) On the change of refrangibility of light. Philosophical Transactions of the Royal Society of London, 142, 463-562.

Stopar, J.D., Lucey, P.G., Sharma, S.K., Misra, A.K., Taylor, G.J., and Hubble, H.W. (2005) Raman efficiencies of natural rocks and minerals: Performance of a remote Raman system for planetary exploration at a distance of 10 meters. Spectrochimica Acta Part A: Molecular and Biomolecular Spectroscopy, 61, 2315-2323.

Strekas, T.C., and Spiro, T.G. (1972) Hemoglobin: resonance Raman spectra. Biochimica et Biophysica Acta (BBA) - Protein Structure, 263, 830-833.

Tang, J., and Albrecht, A.C. (1970) Developments in the theories of vibrational Raman intensities. In H.A. Szymanski, Ed. Raman Spectroscopy, Theory and Practice, Vol. 2. Plenum Press, New York.

Taran, M., Koch-Müller, M., Wirth, R., Abs-Wurmbach, I., Rhede, D., and Greshake, A. (2009) Spectroscopic studies of synthetic and natural ringwoodite, γ-$(Mg,Fe)_2SiO_4$. Physics and Chemistry of Minerals, 36, 217-232.

Tomioka, N., and Fujino, K. (1997) Natural $(Mg,Fe)SiO_3$-Ilmenite and -Perovskite in the Tenham Meteorite. Science, 277, 1084-1086.

Tomioka, N., and Kimura, M. (2003) The breakdown of diopside to Ca-rich majorite and glass in a shocked H chondrite. Earth and Planetary Science Letters, 208, 271-278.

Tomioka, N., Mori, H., and Fujino, K. (2000) Shock-induced transition of $NaAlSi_3O_8$ feldspar into a hollandite structure in a L6 chondrite. Geophys. Res. Lett., 27, 3997-4000.

Toupry, N., Poulet, H., Le Postollec, M., Pick, R.M., and Yvinec, M. (1983) A Raman spectroscopic study of the structural phase transition and reorientational motions of the $ClO_4^-$ ions in $KClO_4$. Journal of Raman Spectroscopy, 14, 166-177.

Triebold, S., Luvizotto, G.L., Tolosana-Delgado, R., Zack, T., and von Eynatten, H. (2011) Discrimination of $TiO_2$ polymorphs in sedimentary and metamorphic rocks. Contributions to Mineralogy and Petrology, 161, 581-596.

Trulson, M.O., and Mathies, R.A. (1986) Raman cross section measurements in the visible and ultraviolet using an integrating cavity: Application to benzene, cyclohexane, and cacodylate. The Journal of Chemical Physics, 84, 2068-2074.

van Schrojenstein Lantman, E.M., Deckert-Gaudig, T., Mank, A.J.G., Deckert, V., and Weckhuysen, B.M. (2012) Catalytic processes monitored at the nanoscale with tip-enhanced Raman spectroscopy. Nature Nanotechnology, 7, 583-586.

Wang, A., Freeman, J.J., Jolliff, B.L., and Chou, I.M. (2006) Sulfates on Mars: A systematic Raman spectroscopic study of hydration states of magnesium sulfates. Geochimica et Cosmochimica Acta, 70, 6118-6135.

Wang, A., Jolliff, B.L., and Haskin, L.A. (1995) Raman spectroscopy as a method for mineral identification on lunar robotic exploration missions. Journal of Geophysical Research: Planets, 100, 21189-21199.

Wang, A., Jolliff Brad, L., Haskin Larry, A., Kuebler Karla, E., and Viskupic Karen, M. (2001) Characterization and comparison of structural and compositional features of planetary quadrilateral pyroxenes by Raman spectroscopy. American Mineralogist, 86, p. 790.

Wang, A., Kuebler, K., Jolliff, B., and Haskin, L.A. (2004) Mineralogy of a Martian meteorite as determined by Raman spectroscopy. Journal of Raman Spectroscopy, 35, 504-514.

Wetherill, G.W. (1980) Formation of the terrestrial planets. Annual Review of Astronomy and Astrophysics, 18, 77–113.

White, S.N. (2009) Laser Raman spectroscopy as a technique for identification of seafloor hydrothermal and cold seep minerals. Chemical Geology, 259, 240-252.

Wiens, R., and Maurice, S. (2016) SuperCam. Mars Future Rover Plans, NASA 2020 Launch. Available: http://mars.nasa.gov/mars2020/mission/science/for-scientists/instruments/supercam/ (accessed June 16th, 2016). Jet Propulsion Laboratory, California Institute of Technology.

Wiens, R.C., Maurice, S., McCabe, K., Cais, P., Anderson, R.B., Beyssac, O., Bonal, L., Clegg, S.M., Deflores, L., Dromart, G., Fischer, W.W., Forni, O., Gasnault, O., Grotzinger, J.P., Johnson, J.R., Martinez-Frias, J., Mangold, N., McLennan, S., Montmessin, F., Rull, F., Sharma, S.K., Sautter, V., Lewin, E., Cloutis, E., Poulet, F., Bernard, S., McConnochie, T., Lanza, N., Newsom, H., Ollila, A., Leveille, R., Le Mouelic, S., Lasue, J., Melikechi, N., Meslin, P.-Y., Misra, A., Grasset, O., Angel, S.M., Fouchet, T., Beck, P., Bridges, N., Bousquet, B., Fabre, C., Pinet, P., Benzerara, K., and Montagnac, G. (2016) The SuperCam Remote Sensing Instrument Suite for Mars 2020 47th Lunar and Planetary Science Conference, The Woodlands, Texas, Abstract# 1322.

Wiens, R.C., Sharma, S.K., Thompson, J., Misra, A., and Lucey, P.G. (2005) Joint analyses by laser-induced breakdown spectroscopy (LIBS) and Raman spectroscopy at stand-off distances. Spectrochimica Acta Part A: Molecular and Biomolecular Spectroscopy, 61, 2324-2334.

Wu, M., Ray, M., Fung, K.H., Ruckman, M.W., Harder, D., and Sedlacek, A.J. (2000) Stand-off detection of chemicals by UV Raman spectroscopy. Applied Spectroscopy, 54, 800-806.

Xie, Z., and Sharp, T.G. (2007) Host rock solid-state transformation in a shock-induced melt vein of Tenham L6 chondrite. Earth and Planetary Science Letters, 254, 433-445.

Xie, Z., Sharp, T.G., and DeCarli, P.S. (2006) High-pressure phases in a shock-induced melt vein of the Tenham L6 chondrite: Constraints on shock pressure and duration. Geochimica et Cosmochimica Acta, 70, 504-515.

Yang, H., Konzett, J., Frost Daniel, J., and Downs Robert, T. (2009) X-ray diffraction and Raman spectroscopic study of clinopyroxenes with six-coordinated Si in the $Na(Mg_{0.5}Si_{0.5})Si_2O_6$-$NaAlSi_2O_6$ system. American Mineralogist, 94, p. 942.

Yin, J.-H., Li, Z.-W., Tian, Y.-J., Sun, Z.-W., and Song, X.-L. (2005) A study on Raman scattering cross sectionof carbon tetrachloride at low concentrations. Applied Physics B, 80, 573-576.

Yu, Y., Lin, K., Zhou, X., Wang, H., Liu, S., and Ma, X. (2007) New C−H Stretching Vibrational Spectral Features in the Raman Spectra of Gaseous and Liquid Ethanol. The Journal of Physical Chemistry C, 111, 8971-8978.

Yu, Y., Wang, Y., Hu, N., Lin, K., Zhou, X., and Liu, S. (2014) Overlapping spectral features and new assignment of 2-propanol in the C–H stretching region. Journal of Raman Spectroscopy, 45, 259-265.

Yu, Y.G., and Wentzcovitch, R.M. (2006) Density functional study of vibrational and thermodynamic properties of ringwoodite. Journal of Geophysical Research: Solid Earth, 111, n/a-n/a.

Zachhuber, B., Gasser, C., Chrysostom, E.t.H., and Lendl, B. (2011a) Stand-off spatial offset Raman spectroscopy for the detection of concealed content in distant objects. Analytical Chemistry, 83, 9438-9442.

Zachhuber, B., Ramer, G., Hobro, A., Chrysostom, E.H., and Lendl, B. (2011b) Stand-off Raman spectroscopy: a powerful technique for qualitative and quantitative analysis of inorganic and organic compounds including explosives. Analytical and Bioanalytical Chemistry, 400, 2439-2447.

Zhang, A., Hsu, W., Wang, R., and Ding, M. (2006) Pyroxene polymorphs in melt veins of the heavily shocked Sixiangkou L6 chondrite. European Journal of Mineralogy, 18, 719-726.

Zhu, G., Zhu, X., Fan, Q., and Wan, X. (2011) Raman spectra of amino acids and their aqueous solutions. Spectrochimica Acta Part A: Molecular and Biomolecular Spectroscopy, 78, 1187-1195.